INFORMATION TO USERS

This manuscript has been reproduced from the microfilm master. UMI films the text directly from the original or copy submitted. Thus, some thesis and dissertation copies are in typewriter face, while others may be from any type of computer printer.

The quality of this reproduction is dependent upon the quality of the copy submitted. Broken or indistinct print, colored or poor quality illustrations and photographs, print bleedthrough, substandard margins, and improper alignment can adversely affect reproduction.

In the unlikely event that the author did not send UMI a complete manuscript and there are missing pages, these will be noted. Also, if unauthorized copyright material had to be removed, a note will indicate the deletion.

Oversize materials (e.g., maps, drawings, charts) are reproduced by sectioning the original, beginning at the upper left-hand corner and continuing from left to right in equal sections with small overlaps. Each original is also photographed in one exposure and is included in reduced form at the back of the book.

Photographs included in the original manuscript have been reproduced xerographically in this copy. Higher quality 6" x 9" black and white photographic prints are available for any photographs or illustrations appearing in this copy for an additional charge. Contact UMI directly to order.

U·M·I

University Microfilms International
A Bell & Howell Information Company
300 North Zeeb Road, Ann Arbor, MI 48106-1346 USA
313/761-4700 800/521-0600

Order Number 9224818

Positron diffusion in solid and liquid metals

Gramsch, Ernesto Vicente, Ph.D.

City University of New York, 1992

U·M·I
300 N. Zeeb Rd.
Ann Arbor, MI 48106

H

Positron diffusion in solid and liquid metals

by

Ernesto Gramsch

A dissertation submitted to the Graduate Faculty in Physics
in partial fulfillment of the requirements for the degree of
Doctor of Philosophy, The City University of New York.

1992

This manuscript has been read and accepted for the Graduate Faculty in Physics in satisfaction of the dissertation requirements for the degreee of Doctor of Philosophy.

28 Feb 1992

Date

Martin A. Kramer

Dr. Martin A. Kramer
Chair of Examining Committee

5 March 1992

Date

Joseph B. Krieger

Dr. Joseph B. Krieger
Executive Officer

Dr. Herman Z. Cummins

Dr. Kelvin. G. Lynn

Dr. Myriam P. Sarachik

Supervisory Committee

The City University of New York

Abstract

Positron diffusion in solid and liquid metals

by

E. Gramsch

Adviser: Kelvin G. Lynn

A systematic study of diffusion of positrons in several liquid and solid metals was performed with a vertical positron beam. The S parameter and positronium fraction was measured as a function of temperature in the solid and liquid phases for Ga, Bi, Na, Sn, In and Pb. An appreciable change is observed in metals where positrons trapping is not observed in the solid just below the melting point (Ga, Bi, Na, Sn). In metals where positrons are trapped below the melting point (In and Pb), a very small or no change is observed upon melting. The results suggest that all positrons are trapped in the liquid.

The diffusion length of positrons in the liquid was also measured. In Ga, Bi and Sn, a large drop is observed upon melting. In Pb and In only small or no change change is observed. In all liquid metals, as the temperature of the liquid is increased the diffusion length increases. Diffusion appears to be related to trapping in temporary density fluctuations, thus the positron hops from one trap to another. The size of the traps is strongly dependent on temperature, so that when it is increased, the hopping motion increases.

The re-emitted energy spectra of positrons from the liquid and solid surfaces was measured. No appreciable change was seen with increasing temperature. or when the sample is melted.

Acknowledgement

I would like to express my appreciation to the many people that cooperated to the happy ending of this project. Specially I am grateful to Kelvin Lynn for his guidance and great support in scientific and financial matters. I appreciate the advise and support from Len Roellig, who introduced me to positron physics and invited me to work at the Laboratory. I want to thank H. Cummins, M. Sarachik, and M. Kramer for agreeing to be in my thesis committee. The beam would have been hard to complete without the design from Jane Throwe and John Dioguardi, a lot of help from Gabriel Muñoz, Ikuzo Kanazawa, Harry Hacker, and Mike Carrol. Comments and very useful discussions with Bent Nielsen, Steve Usmar, Ravinder Khatry, S. Tang, M. Weber, X. Wu and Ken Ritley, are greatly appreciated.

I cannot forget my wife Angela, that endured this long project and supported me at all times. This project would have been impossible without her constant encouragement.

Table of Contents

Chapter II. Diffusion model

Chapter III. Liquid metals

Chapter IV. Experimental section

Chapter V. Results

List of figures

Chapter I. Introduction

Our knowledge of the liquid state of matter has made slow progress in the last decades compared to our knowledge of the crystalline structure of solids and the dynamics of gases. Part of the reason is the few techniques available to study liquids, as well as intrinsic difficulties in formulating models for them.[1-5] Because many crystals are grown or refined from the molten state, the study of its structure and properties is important. Liquid metals can be considered as an ensemble of ions and electrons with good electrical and thermal conductivity. The density of electron states in liquids is generally free-electron-like.[1] In contrast to a solid metal, the components of a liquid metal must move under an irregular configuration of ions. This is the basic difficulty in formulating a model for a liquid: the theory must include the potentials between all pairs of ions. Simplifications that can be included in the model due to a periodic arrangement of atoms (as in a crystalline solid), or due to a completely disordered structure (as in a gas) are not satisfactory for modelling a liquid. Because of the irregular arrangement of the ions, there can be regions of low ion density in a liquid. similar to vacancies or voids in a solid. Because positrons have a strong sensitivity to vacancies and other defects[6] in solids, techniques that use positrons as a probe, like angular correlation or lifetime, have been extensively used to measure vacancy formation energies in solid metals in the past decade.[7-12] In this work, we will use the strong sensitivity of positrons to defects to study the regions of low ion density and the dynamics of such defects in a liquid.

Most of our knowledge of the liquid structure comes from x-ray and neutron diffraction experiments[1-5]. These experiments allow to determine the structure factors from liquid metals, which can be compared with calculations based on pair potentials between ions. A disadvantage of these techniques is their short range order: only the structure of the nearest atoms can be determined. Positrons, in contrast are sensitive to defects that are located many lattice-spaces away[8]. Therefore the positron annihilation technique can be used to complement x-ray and neutron diffraction results.

The study of condensed matter with positrons has a long history since their discovery in 1932 by Anderson[7]. The first applications to solid-state physics were in bulk studies of electronic structure. Lifetime techniques and measurements of the angular correlation of annihilation gamma rays were extensively used. The interaction of positrons with matter has given information about its fundamental properties, as for example the electron momentum distribution, or defect concentration.[8] The positron probe does not depend on long-range order, as do diffraction techniques, but probes local structure. Therefore, positrons have the potential to be useful for studying liquids and solid-liquid interfaces.

The study of defects in metals using positrons started in 1967, when MacKenzie *et al.*[9] demonstrated that thermally generated vacancies in several metals can trap or localize positrons.[6] Since then, the research done with positrons in solid-state physics has increased considerably, several techniques were developed or improved. Lifetime techniques[9] show that the residence time of the positron in a solid increases when it is trapped at vacancies or defects. Angular correlation techniques[10,11] show that positrons have a narrower spectrum when they are trapped at defects than when they are in the bulk of a crystalline solid.

The sensitivity of positrons to changes caused by melting was demonstrated by early studies of liquids with angular correlation[12–15] and lifetime[16–17] techniques. For several metals the lifetime was seen to increase 10 – 40 % on melting, as shown in figure 1.1 for mercury (Hg), gallium (Ga), and sodium (Na). In angular correlation studies[18], the proportion of conduction-electron annihilation relative to core annihilation was considerably higher in the liquid than in the solid. Figure 1.2 shows the results for Hg.

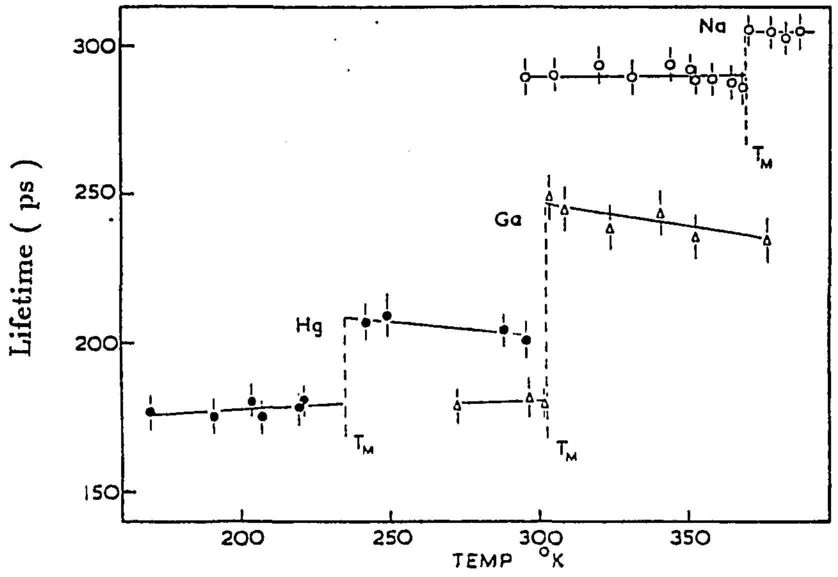

Figure 1.1: Positron lifetimes for solid and liquid metals, The increase in lifetime upon melting (T_M) is attributed to positron trapping. From reference 20.

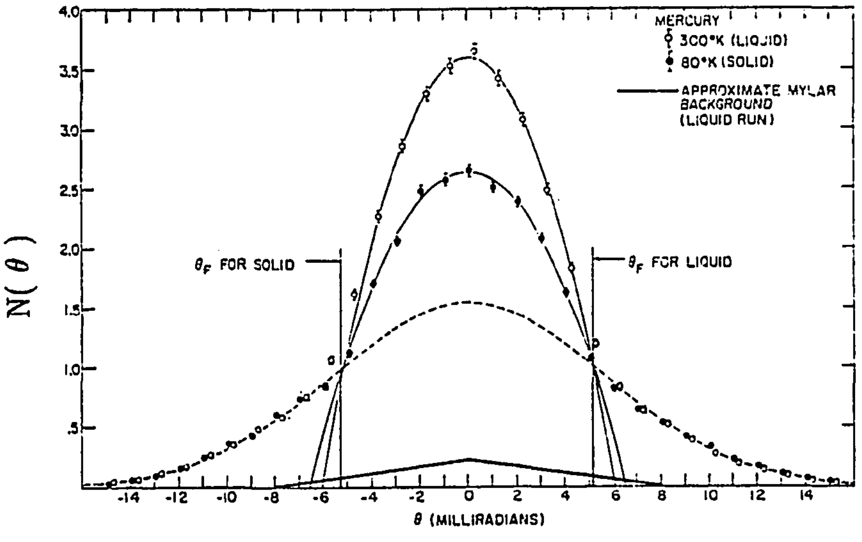

Figure 1.2: Angular correlation results from solid and liquid mercury (Hg). An increase in the proportion of conduction electron annihilations is observed in liquid Hg. From reference 15.

The effects were attributed to disorder in the conduction electrons, but the nature of the change was not clear until MacKenzie *et al*[9] showed that vacancies could trap positrons. The changes observed upon melting were qualitatively similar to those arising from positron-trapping at thermal vacancies in solids. In addition, a large change was observed in metals where vacancy trapping does not occur in the solid phase[16] (for example Ga, tin (Sn)), which suggests that the disorder creates regions of low-ion density, similar to vacancies in solids, that can trap the positrons. Metals that show large changes in angular correlation and lifetime in the solid phase upon heating, demonstrate a small change or no change on melting (for example lead (Pb), or indium (In)). This finding suggests that positrons trapped in the solid remain trapped upon melting. Doppler broadening results[19], very clearly show the effect of thermal vacancy trapping in several metals, as shown in figure 1.3. Upon melting there is a sudden increase in the peak counts, and no further increase in spite of the increasing temperature. In all metals studied the increase can be associated with trapping of positrons.[19] Doppler broadening measurements in In and Pb are shown in figure 1.3.

The techniques discussed above all obtain positrons from a radioactive source. Depending on the source, the energy distribution can be very wide ($0 - 0.545$ MeV for ^{22}Na), with a large end-point energy, and the positrons can penetrate deep into the sample. Therefore, the techniques are sensitive only to bulk effects. To date, no studies of positron annihilation at the surface of clean liquid metals have been reported.

In contrast to lifetime or angular correlation techniques, positron beams have a narrow energy distribution, which allows us to implant them into the sample at a depth that is known and, most important, that can be controlled.

The angular distribution and the size of the beam also is very small.[6] At low incident energies ($E < 100$ eV), positrons do not penetrate deeply into the sample so that the surface of the sample can be studied.

Positron beams have been shown to be useful probes for defect profiling in crystalline solids[8]. With the discovery of efficient positron moderators[8,21,22] slow positron beams were developed, representing a major step in the research in the positron field[8]. New techniques were developed, such as positronium emission spectroscopy[23], positron Auger spectroscopy[24], and beams that provide a depth-sensitive probe for interface studies. It became possible to measure the diffusion length of thermal positrons in matter using positron beams.[21,25]

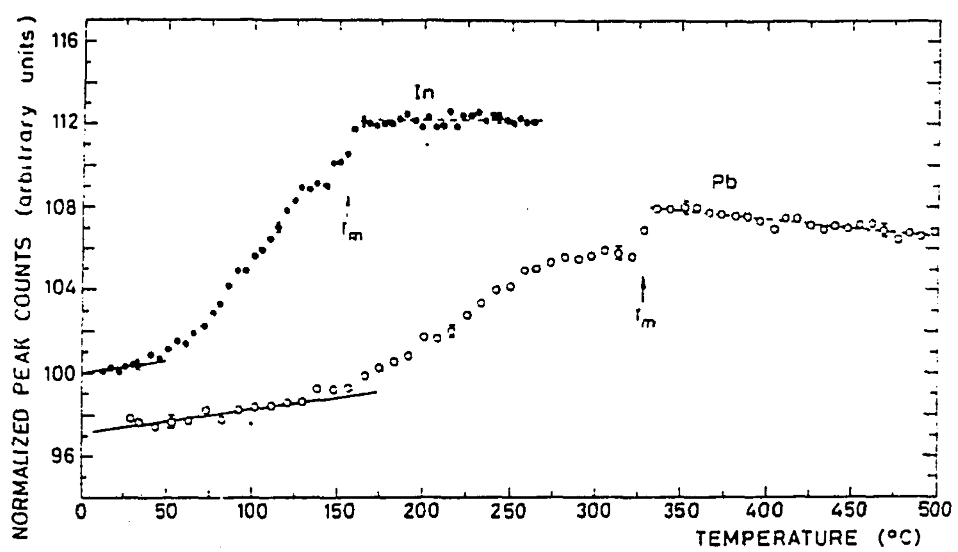

Figure 1.3: Doppler broadening measurements in two solid and liquid metals. The increase at the melting point can be associated with trapping in regions of low ion density. From reference 19.

It is well known[8,27–37] that diffusion of thermalized positrons in solids is determined by their interaction with phonons, impurities, or trapping (in vacancies, voids, or other type of defects). In a defect-free metal, the diffusion coefficient D_+ for positrons has a temperature dependence[27] of $D_+ \sim T^{-1/2}$. In some metals, at temperatures close to the melting point, positrons become trapped at thermally generated vacancies, and the diffusion coefficient rapidly decreases.

Upon melting, the metal looses its crystalline structure, and a disordered array of atoms is generated. There is an increase in the number, as well as a change in the nature of the traps (considered as regions of low ion-density), and positron localization increases. Because trapping will probably increase, and positrons move in a disordered array, we expect that the diffusion coefficient then will drop to a value lower than in the solid phase.

If positron diffusion in liquid metals is determined by the same mechanisms as in the solid phase (phonon scattering and trapping), we would expect that the diffusion coefficient continues to decrease with increasing temperature.

In contrast, in the liquids studied, the diffusion coefficient increases with temperature. This surprising result suggests that a different mechanism is involved in the interaction of positrons with liquids.

To better understand the diffusion mechanism in liquids, we have made a systematic study of the diffusion characteristics of positrons in several liquid and solid metals. A vertical positron beam was designed and constructed to study low melting temperature metals under ultra high-vacuum. It is also of considerable interest to study surface defects (or regions of low ion density), positron and positronium states in the surface, and the relation between the diffusion coefficient and density fluctuations in liquids.

Chapter 2 discuses the different interactions of positrons with solid and liquid metals and the energy and time scales at which they occur. We assume the motion of the thermalized positron to be a random walk, and describe its motion with the diffusion equation. In this chapter, we define the S and F parameters which are the quantities measured experimentally. The S parameter is fitted to the solution of the diffusion equation to extract the diffusion length. Finally a description of the program used for the fits is given.

Chapter 3 describes the modern theory of liquid metals in terms of correlation functions. It also gives a description of the neutron scattering and x-ray diffraction methods used to derive the pair correlation functions.

In chapter 4 we give a description of the positron beam and the special features necessary for the study of liquid metals, and samples with high vapor pressure. We also discuss the different types of moderators used for positron beams and give a comparison of their efficiencies.

Chapter 5 presents the experimental results. The metals studied are separated in two groups according to the state of the positron in the solid phase at $T < T_m$. The first group is formed by Ga, Bi, Na, and Sn. In these metals, positrons do not get trapped in thermally generated vacancies in the solid phase, but trapping is observed in the liquid phase. Consequently, there are large changes in the S and F parameters and in the diffusion coefficient. The second group is formed by Pb and In, in which positron trapping at thermally generated vacancies is observed at $T < T_m$.

Section 5.1 has the S and F parameters versus energy. These measurements are used to determine the state of the positron in the solid or liquid phases (free or trapped). The sensitivity of positrons to the melting transition and positronium formation in liquid surfaces is discussed. The S parameter and Positronium fraction (F parameter) is measured as a function of temperature for several incident energies. The results are compared to previous studies of positron lifetimes and Doppler broadening in liquids. A surface state is shown to exist in the liquid, and positronium formation is observed in several liquid surfaces.

In section 5.2 , we present the diffusion length results in solid and liquid metals. The increase in the diffusion length with temperature is discussed in terms of hopping between traps and is related to density fluctuations in the host or thermal desorption of positrons from traps. However, to obtain more quantitative information of the fluctuations in liquid metals, we need a theoretical model relating the diffusion length to density fluctuations.

In section 5.3 , we show measurements of nonthermal positron emission from the surface of liquid and solid metals. A small fraction (5 - 15 %) is re-emitted from Bi, Sn, and In. This fraction is unchanged upon melting.

The conclusions and suggestions for future studies are presented in chapter 6.

Chapter II. Diffusion model

2.1 Interaction of fast positrons with matter

The interactions of an energetic positron with matter can be described according to the energy that the positron has at a given time. The scattering mechanisms between positrons and the solid are strongly energy dependent.[28–31] Inelastic ion core scattering is dominant at high energies (E > 1 keV), while the creation of electron-hole pairs, plasmon excitation, and phonon scattering are dominant at lower energies (E < 1 keV). Since the energies that can be attained with the Liquid Metals Beam range down from 25 keV, the processes relevant to our work are those that occur below 25 keV.

As illustrated in figure 2.1, an energetic beam of positrons incident on a sample undergoes processes on several different time scales and energies. The longest time is spent by the positron in thermal motion in the solid (with energy $E = 3/2\ k_B T$). Positron lifetimes are of the order of 10^{-10} sec for most metals; this is much longer than prethermalization period[31] which lasts $\approx 10^{-12}$sec. It is during the slowing process that the spatial distribution of the positrons in the sample is determined (usually a Makhovian profile).

At shorter times, $0 < t < 10^{-15}$sec, a positron can be scattered or diffracted, leaving the sample after losing only a fraction of its energy. If annihilation takes place far from the detector, the gamma rays will not be detected, and the positrons will not contribute to the diffusion equation. For samples with high Z (*eg.* Pb, Bi), the backscattered fraction can be high and many of those positrons will be trapped by the magnetic field and later return to the sample. The energy of these positrons is likely to be lower than the incident energy. Thus, there is a situation where the incident beam is not monoenergetic, but has a low energy tail.

This effect, which tends to modify the spatial profile of the incident positrons, will be discussed in section 5.2.

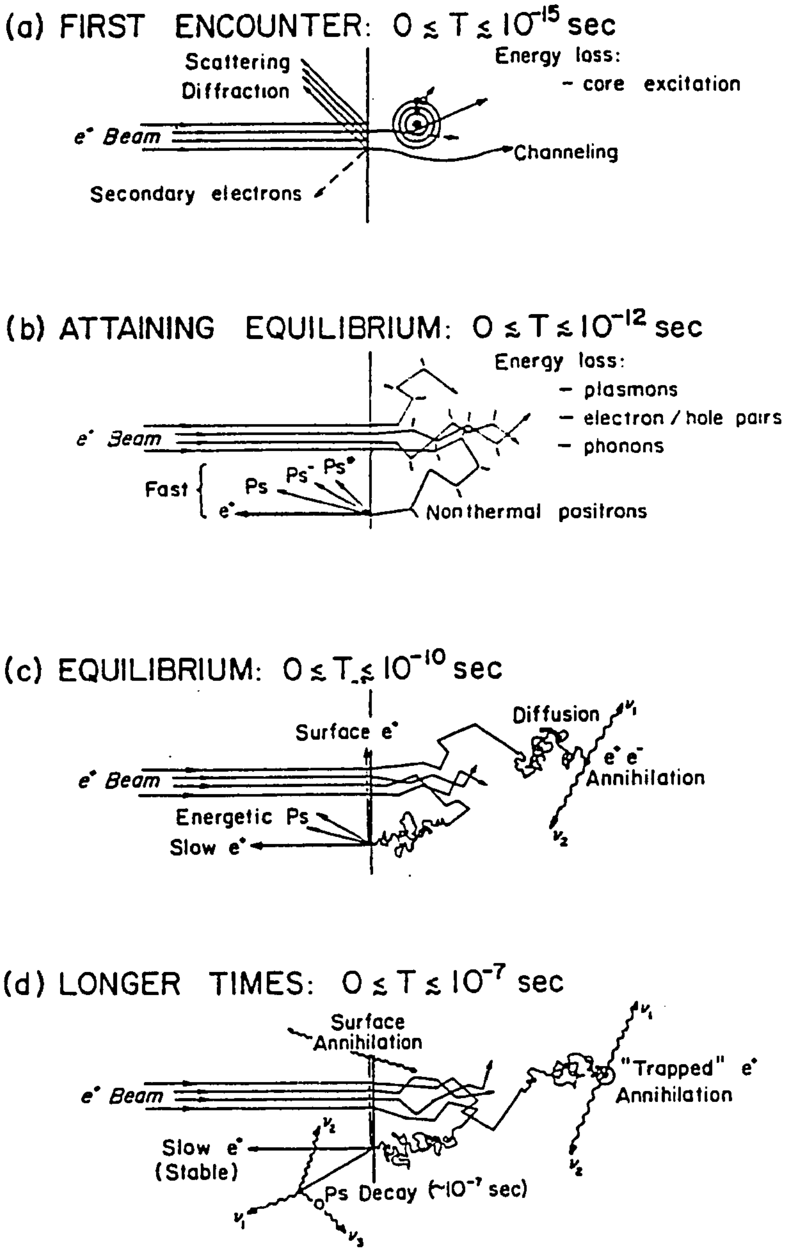

Figure 2.1: Typical interactions of positrons near the surface of a solid, organized according to the time scales at which they occur. The process of energy loss is different for each stage. From reference 8.

If the sample is a crystalline solid, the positrons will be channeled along the planes of a crystal, and strong scattering and absorption is observed for specific orientations. This effect has been discussed by others[32,33] and will not be discussed here because it is not relevant for a liquid or polycrystalline solid.

At high incident energies, from 50 keV down to ≈ 1 keV, the positron scatters mainly with core electrons, and the rate of energy loss is very fast. In this initial stage, the time required for the positron to reach 1 keV is less than $\sim 1 \times 10^{-15}$ sec. The angular deflection in each scattering event is small, and the differential scattering cross-section is peaked in the forward direction[34] (figure 2.1a).

At energies from about 1 keV down to the Fermi energy, the dominant process of energy loss is inelastic scattering by conduction electrons. Oliva[28] showed that plasmon excitation is dominant over electron-hole pair excitation. Direct evidence of plasmon excitation was found by Dale *et. al.*[35] This second stage of energy loss lasts $\sim 1 \times 10^{-12}$ sec. In insulators and semiconductors, because of the energy gap between conduction and valence band, the creation of electron-hole pairs no longer occurs when the energy of the positron is less than the gap energy. This results in the wide energy distribution of positrons re-emitted from ionic solids.[36] The slower rate of energy loss allows some positrons to reach the surface and be reemitted with energies higher than the thermalization energy, E_{th}. This process is illustrated in figure 2.1b (nonthermal positrons). For these reasons, the thermalization times and mean free path of positrons in insulators and semiconductors are longer than those in metals. For example, it was observed[37] that the average energy loss per collision in solid Ne is only ~ 6 meV.

At even lower energies, from the Fermi energy E_F to thermal energies E $= \frac{3}{2}k_B T$, inelastic phonon scattering becomes dominant. The crossover from electron-to phonon-dominated scattering was found to be ≈ 5 eV, as shown by the onset of temperature dependence in figure 2.2.

Perkins and Carbotte[30] calculated the rate of energy loss including phonon and electron scattering. These were extended by Nieminen and Oliva[31] to include different thermalization temperatures; their results are shown in figure 2.3.

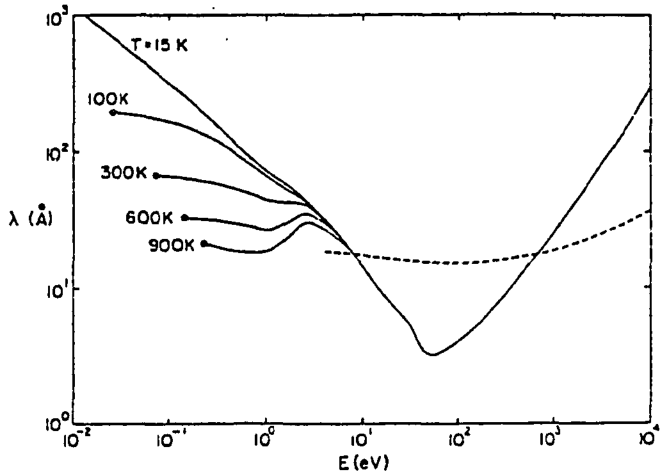

Figure 2.2: Mean free path of nonthermal positrons in Al plotted as function of energy. The model[31] includes the combined effect of electron and phonon scattering. The onset of temperature dependence is at E ≈ 5 eV. From reference 31.

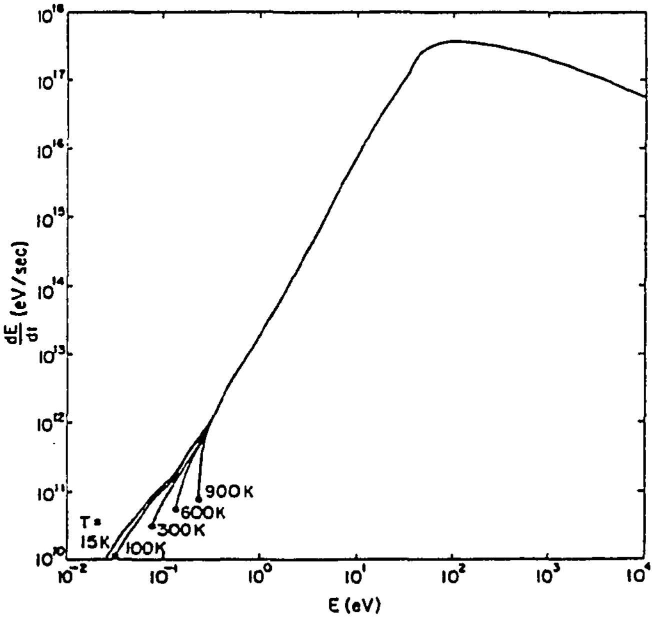

Figure 2.3: Rate of energy loss for positrons in Al. The calculation includes the scattering of positrons with conduction electrons and phonons for several temperatures. From reference 31.

In each scattering event, the positron undergoes angular deflections that are very pronounced close to thermal energies,[31] and its mean free path decreases. The mean free path of nonthermal positrons versus energy is shown in figure 2.3. At low energies, the mean free path is larger (~ 100 Å) than at higher energies. As a consequence of this, there is an overall broadening of the spatial profile of the positrons in the incident direction.

2.2 Nonthermal positrons

Before complete thermalization, a small fraction of positrons can return to the surface or become trapped at defects in the bulk of the sample. In the analysis of lifetime measurements,[38,39] nonthermal trapping of positrons was proposed to explain a drop with temperature in λ_f, the annihilation rate of untrapped positrons. Nonthermal positron trapping in vacancies was observed only recently with a positron beam[40,41] and was shown to affect the analysis that is used to obtain the diffusion length of positrons. These experiments also showed that trapping is a very efficient process that can occur in times shorter than 10^{-13} sec. A recent theoretical model[42] shows resonances in the trapping rate at energies of about 1 - 2 eV, that can only enhance nonthermal trapping. The analysis of lifetime data, as well as calculations of diffusion length are affected by the the fraction of nonthermal positrons.

Gramsch and Lynn[43] included the effect of nonthermal trapping in the analysis of lifetime data in Al. They modified the standard, two-state trapping model in the energy range between 5 eV and the thermalization energy E_{th}. Their model includes the effect of resonance trapping in vacancies and divacancies. A positron-energy-loss function[30] and energy-dependent trapping rates[42] were used to calculate the mean lifetime and intensity of the untrapped and trapped positrons. To compare these theoretical calculations with experimental data, a nonlinear fitting routine was used to obtain a best fit to the experimental lifetime results of Jackman *et al*[39] in Al. Gramsch and Lynn[43] showed that the lifetime calculated with this model is longer than that resulting from the simple trapping model.[43] This effect is more evident at temperatures close to the melting point, where large numbers of vacancies are in thermal equilibrium in the sample. The fitted results along with the experimental data are shown in figure 2.4.

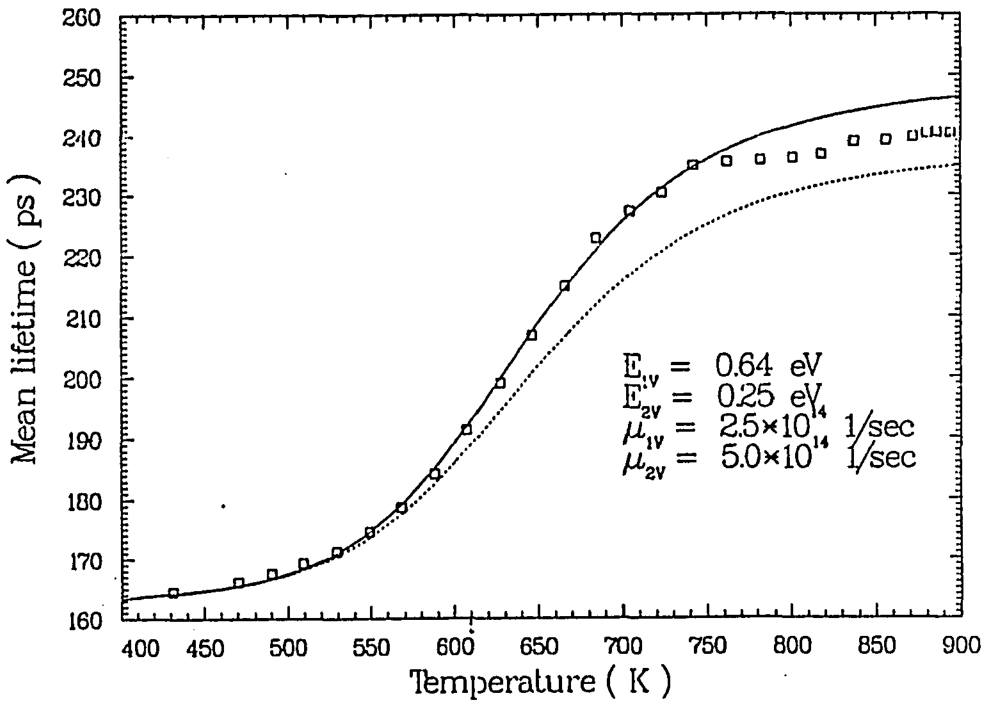

Figure 2.4: Mean lifetime of positrons in Al. The squares are the experimental data. The solid line is the fit using the the model proposed in reference 43. The dashed line corresponds to the standard two-states trapping model.

The solid line shows the fitted results. The fitted parameters are written in the plot. E_{1V} is the formation energy of vacancies, E_{2V} is the formation energy of divacancies in the metal, μ_{1V} and μ_{2V} are the specific trapping rates of positrons in vacancies and divacancies respectively. The dashed line is the lifetime as obtained using the standard two-states trapping model with the same parameters as the solid line. The model does not fit in the high-temperature region, where the lifetime remains relatively constant. This effect is probably due to saturation trapping, *i.e.*, all positrons are trapped, and an increase in the number of vacancies does not lead to a change in the lifetime.

There is a variety of channels open to nonthermal positrons that return to the surface. They may be re-emitted from the sample with $E > E_{th}$, even if the positron work-function is positive, or they may form nonthermal positronium and leave the sample. The positronium activation energy is smaller than the positron work function; thus, this effect is probably more significant because it is energetically favorable. Nonthermal positron and positronium emission have not yet been included in the diffusion model. However, there are techniques to estimate the magnitude of the error incurred by their omission.[44] The effect of nonthermal re-emission of positrons in the analysis of the diffusion length will be discussed in section 5.2.

2.3 Diffusion of thermal positrons

When monoenergetic positrons from a beam have reached thermal energies, $E_{th} = \frac{3}{2}k_B T$, the spatial distribution within the sample in the incident direction (z) can described by a Makhovian distribution[45]

$$P(z) = \frac{mz^{m-1}}{z_0^m} \exp\left(-(z/z_0)^m\right), \tag{2.1}$$

where $z_0 = \bar{z}/\Gamma(1/m+1)$. The distribution is isotropic in a plane parallel to the surface. The mean implantation depth, $\bar{z}$ is assumed to be a power law,

$$\bar{z} = AE^n, \tag{2.2}$$

where E is the incident energy of the beam, and A is a constant to be discussed below. The relation (2.2) between incident energy and mean implantation depth gives us a depth-sensitive probe, which is essential for defect-profiling or multi-layer studies. The value of n depends on the energy, and it varies from 1.16 at 3

MeV to 1.68 at 10 keV.[40,46] From Monte Carlo simulations,[34] and from studies of multilayer structures,[47,48] it was found that n ≈ 1.6 for positrons, but there are indications that this value depends on the material.[49–53]

The shaping parameter, m, is found to be close to 2 from fits to Monte Carlo simulations[34], and from studies of multilayer structures.[47] Monte Carlo simulations by McKeown *et al*[52] are shown in figure 2.5. However, in magnetically guided positron beams, a fraction of the incident positrons are backscattered out of the the sample.

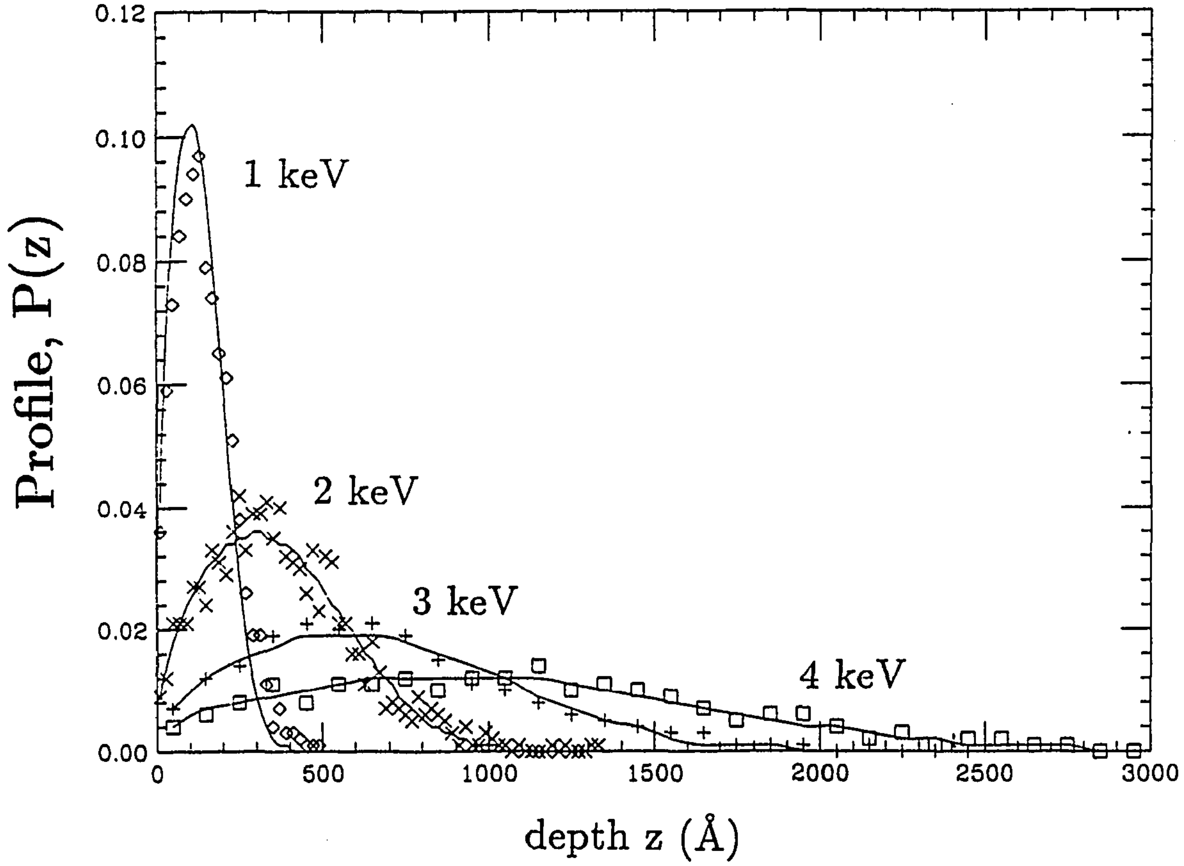

Figure 2.5: Stopping profile for 1, 2, 3, and 4 keV incident positrons on Al, as obtained from Monte Carlo simulations[52]. The solid lines are fits to the Makhovian profile.

This effect is more evident in metals with high Z (Pb, Bi). The backscattered positrons are trapped by the magnetic field of the beam and may return to the sample, thus modifying the profile by increasing the number of positrons in the low energy region.[50] There is little experimental evidence of the modification to the implantation profile[8] due to backscattered positrons. This effect will be discussed in section 5.3.

The value of A is also controversial. Experimentally, it was found that A$\approx$ $4.0/\rho$ [μgr/cm^2], where ρ is the density of the sample.[54] Multilayer studies[47] give A $= 4.5(4)/\rho$ [μgr/cm^2], and Monte Carlo simulations[34] give A $= 4.6/\rho$ [μgr/cm^2]. The value used in this work is A $= 4.0/\rho$ [μgr/cm^2], following reference 8.

Monte Carlo simulations by McKeown *et al*[52] show that A and n depend on the density and the atomic number Z of the host material. A increases significantly with the atomic number, (figure 2.6), and n decreases with Z. But the combined variations of n and A do not significantly alter the mean implantation depth, $\langle z\rangle$, from the standard implantation depth, eq. (2.2).

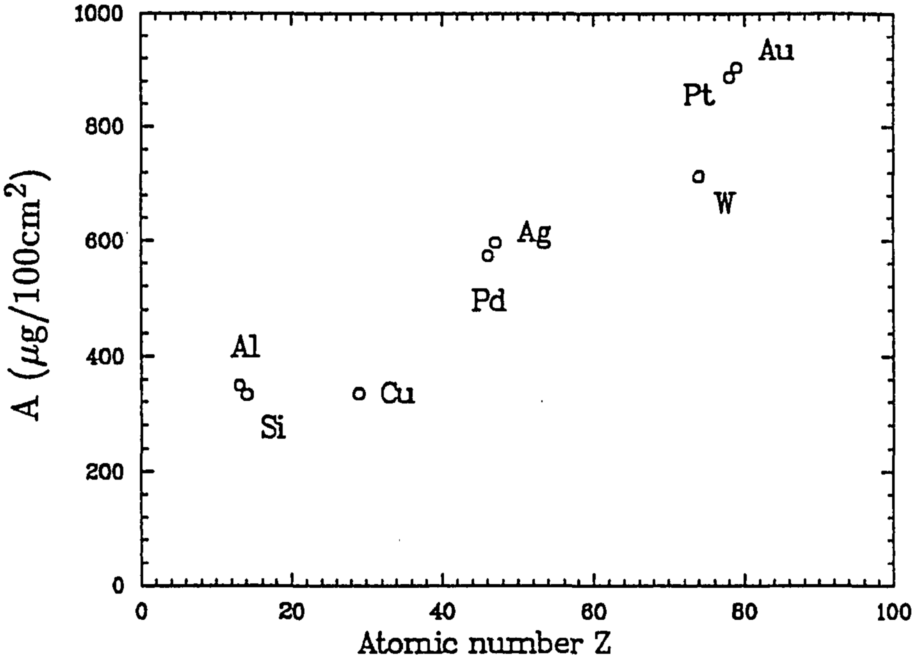

Figure 2.6: Dependence of the A parameter on the atomic number, Z. These results were obtained by fitting the mean implantation depth obtained from Monte Carlo simulations to the equation $\langle z\rangle = (A'/\rho)E^n$.

We note that the Monte Carlo simulations from Valkealahty and Nieminen[34] and McKeown *et al*[52] at low energies only include scattering with valence and core electrons. As a consequence, the end point energy of the positrons is ≈ 25 eV. However, the lower energy interactions with phonons can further modify the implantation profile.

Recent simulations by Ritley and Lynn[53] have shown that the profile can be significantly broadened at low incident energies. A comparison of the profile with thermal end-point energy (T = 23 °C , E = 0.06 eV), and 20 eV end-point energy is shown in figure 2.7(a). The incident energy of the positrons is 1 keV on an Al substrate. The curves have been normalized to the same area. For high incident energies, the difference between thermal energies and 20 eV is less pronounced. Figure 2.7(b) shows the profiles with thermal end-point energy and 20 eV, but for an incident energy of 3 keV. The calculations were done on Al at T = 23 °C . The effect of phonon scattering is less at this temperature because the profile is broad to begin with.

When positrons have thermal energies, the scattering with phonons is isotropic. Under these conditions, the motion of the positron can be characterized as a random walk, with a gaussian velocity distribution. However, the random walk model requires that the implantation depth be much larger than the mean free path. Typical implantation depths[31] are about 10^3 Å, and the mean free path[31] is about 100 Å. For low-energy positrons, which have an implantation depth of ≈ 100Å, the diffusion model may not be valid. The assumption of the model is that the mean free path is smaller than the de Broglie wavelength of positrons. In bulk crystalline materials, the diffusion length is of the order of 200 - 600 Å. Therefore, at low incident energies the model can not be used. However, in liquid metals, all positrons get trapped in regions of low ion density and the de Broglie wavelength is of the order of the atomic dimensions. In this situation, the use of the diffusion model is justified because the de Broglie wavelength is much shorter than the mean free path.

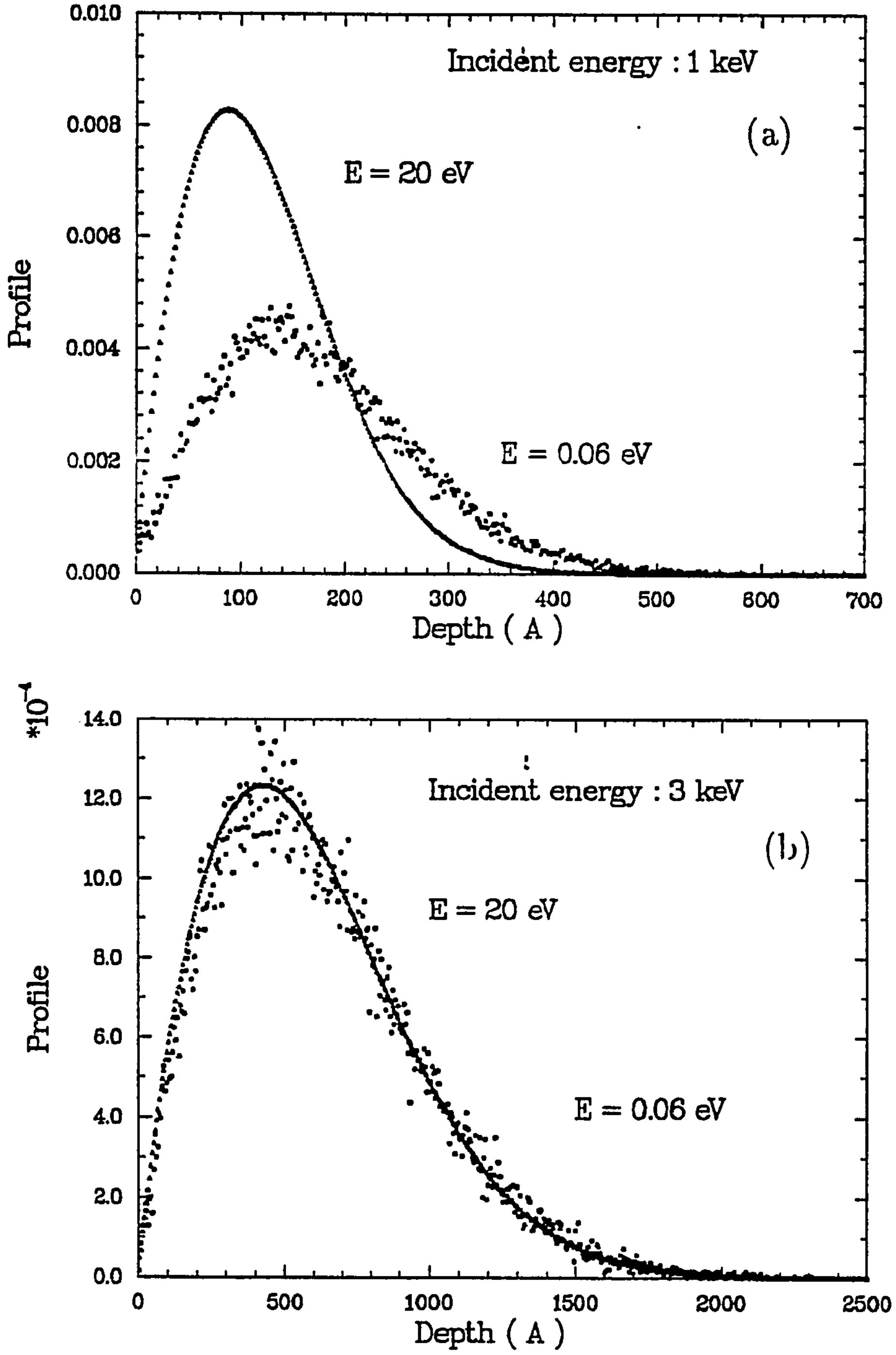

Figure 2.7: Broadening of the implantation profile for positrons with low incident energy. a) Stopping profile for 1 keV incident positrons on Al at $T = 27$ °C . The end-point energy is 20 keV and thermal energy ($5/2\ k_BT$). b) Stopping profile for 3 keV incident positrons on Al at $T = 27$ °C . The end-point energies are the same as in a). From reference 53.

Mathematically, this model of positron motion can be represented by the diffusion equation in one dimension. The derivation of this formula for positrons was given by Mills[21] and Lynn and Welch[55]:

$$\frac{\partial N_p(z,t)}{\partial t} = D_+ \frac{\partial^2 N_p(z,t)}{\partial z^2} - \lambda_{eff} N_p(z,t), \tag{2.3}$$

where z is the distance from the surface, N_p is the positron density, D_+ is the positron diffusion coefficient, $\lambda_{eff} = \lambda_b + \lambda_t$ is the effective annihilation rate of the positron, λ_b is the bulk annihilation rate, and λ_t is the trapping rate. The formula does not included thermal detrapping of the positron, which, in most solids, is generally assumed to be small. The relevance of detrapping in liquids will be discussed in section 5.2.

Nonthermal vacancy trapping has not been included in the diffusion model because otherwise the equations become very complicated and too time-consuming for computer simulations. There is no clear solution to this problem yet, nor is it clear how important the effect is.

The eigensolution to eq. (2.3) for $z > 0$ is given by:

$$n_k = (A\sin(kz) + B\cos(kz))\exp(-\delta t). \tag{2.4}$$

Replacing (2.4) in eq. (2.3), we obtain the relation $\delta = -D_+k^2 + \lambda_{eff}$. The constants A and B can be obtained with the radiative boundary condition[56], that takes into account reflections at the surface:

$$N_p(0,t) = \beta \frac{\partial N_p(z,t)}{\partial z}\bigg|_{z=0}. \tag{2.5}$$

The result is $B = \beta k A$. For $\beta \rightarrow 0$ the surface is perfectly absorbing; this is the case for a metal with a potential well at the surface. For $\beta \rightarrow \infty$, all positrons are reflected by the surface and return to the bulk where they annihilate. Sodium is an example of this later effect (section 5.1). The normalization condition gives $A = 1/\sqrt{1+\beta^2k^2}$. Therefore,

$$n_k(z,t) = \frac{\sin(kz) + \beta k \cos(kz)}{\sqrt{1+\beta^2k^2}} \exp(-\delta t). \qquad (2.6)$$

The general solution is a linear combination of n_k for all possible k:

$$N_p(z,t) = \int_0^\infty C(k) n_k(z,t) dk, \qquad (2.7)$$

where C(k) is obtained from the initial conditions (implantation profile). The standard method[57] to solve for C(k) is to use a δ function, $N_p(z,0) = \delta(z-a)$ in eq. (2.7),

$$N_a(z,t) = \int_0^\infty \left(\frac{2}{\pi} \frac{\sin(ka) + k\beta \cos(a)}{\sqrt{1+\beta^2k^2}} \right) n_k(z,t) dk. \qquad (2.8)$$

From eq. (2.8) we can calculate the number of positrons returning to the surface.

$$F_s(a) = \int_0^\infty |J(0,t)| dt, \qquad (2.9)$$

where,

$$J(0,t) = -D_+ \frac{\partial N_a(z,t)}{\partial z}\bigg|_{z=0} \qquad (2.10)$$

is the flux of positrons through the surface. Substitution of (2.8) and (2.10) into (2.9), and carrying out the integration in k and t, we obtain:

$$F_s(a) = \frac{\exp(-a/\sqrt{D_+\tau_{eff}})}{1+\beta/\sqrt{D_+\tau_{eff}}} \qquad (2.11)$$

For a more general Makhovian implantation profile P(z), the solution is a weighted integral of the delta function result (2.11):

$$\langle F_s \rangle = \int_0^\infty P(a) T(a) da. \qquad (2.12)$$

A closed form for $\langle F_s \rangle$ can be found when m = 1 in the implantation profile (2.2). In this case we have $z_o = AE^n/\Gamma(2) = AE^n$. Substituting (2.1) in eq. (2.12):

$$\langle F_s \rangle = \int_0^\infty \frac{1}{z_o} \frac{\exp(-a\left(\frac{1}{z_o}+\frac{1}{L_+}\right)}{1+\beta/L_+} da \tag{2.13}$$

Where $L_+ = \sqrt{D_+ \tau_{eff}}$ is the diffusion length. The result is:

$$\langle F_s \rangle = \frac{1}{\left(1+\left(\frac{AE}{L_+}\right)^n\right)(1+\beta/L_+)} \tag{2.14}$$

Another analytic solution is found for m = 2, which better fits the Monte Carlo simulations shown in figure 2.4. In this case, $z_o = AE^n/\Gamma(3/2) = = 2AE^n/\sqrt{\pi}$, substituting (2.1) in (2.12)

$$\langle F_s \rangle = \int_0^\infty \frac{2a}{z_0} \frac{\exp -\left((\frac{a}{z_o})^2+\frac{a}{L_+}\right)}{1+\beta/L_+} da. \tag{2.15}$$

The result is:

$$\langle F_s \rangle = \left[1-\frac{AE^n}{L_+}\exp\left(\frac{AE^n}{\sqrt{\pi}L_+}\right)^2 \operatorname{erfc}\left(\frac{AE^n}{\sqrt{\pi}L_+}\right)\right]\left(\frac{1}{1+\beta/L_+}\right), \tag{2.16}$$

where erfc(x) is the complimentary error function. For other values of m, the integration has to be carried out numerically.

The connection between theory and experiment is given by $\langle F_s \rangle$, the number of positrons that return to the surface after being implanted with an energy, E. This value can be directly compared with the experimental results.

There are two methods to determine this fraction experimentally: the measurement of annihilation radiation from positronium (Ps); or the Doppler broadening of the annihilation radiation from positrons trapped at the surface. Both techniques will be discussed in section 2.5

2.4 Interactions at the surface

The potential to which the the positron is subjected at the surface consists of contributions from the interaction with ions, as well as bulk and surface electrons. The bulk part (μ_+), which comes from the interaction of the positron with ions and conduction electrons, is defined as the difference between the crystal zero level for T = 0 °K and the bottom of the lowest positron band. Contributions to μ_+ are the repulsion from the ion cores (zero point potential E_o), and the correlation energy E_{corr}, which is the attraction to the electrons,[58] $\mu_+ = E_{corr} + E_o$. The surface contribution to the potential is the tailing of the electrons into the vacuum, which produces a dipole D, that is directed out of the solid. These contributions are shown in figure 2.8 for a typical metal. The positron work function is defined as the *minimum* energy required to extract a positron from a metal, and is given by:

$$\phi_+ = -D - \mu_+. \tag{2.17}$$

D is positive, and, in some metals, it is sufficiently large that the positron work function is negative, allowing slow positrons reaching the surface to be re-emitted into the vacuum. This situation exists for W ($\phi_+ \approx -3$ eV) , Ni, and Cu. The re-emission effect allows these metals to be used as positron moderators. For electrons, a similar relation holds,

$$\phi_- = D - \mu_-, \tag{2.18}$$

where μ_- is the chemical potential of the conduction electrons.

The Positronium (Ps) formation potential is the energy required to extract a positron and an electron from the metal, minus the binding energy of the Ps atom in vacuum:

$$\phi_{Ps} = \phi_+ + \phi_- - 6.8\ eV. \tag{2.19}$$

For most metals, ϕ_+ is positive, but because of the large binding energy of Ps, ϕ_{Ps} is negative or slightly positive, and Ps formation is the only way that the positron can leave the metal. In a metal with $\phi_+ < 0$ all positrons reaching the surface are expected to form Ps, and the conversion probability to Ps is unity. But, at the surface they are accelerated by the potential well and have some probability of inelastic collisions with the surface electrons. Thus, they might be trapped at the surface, and the probability of forming Ps is less than unity.[31]

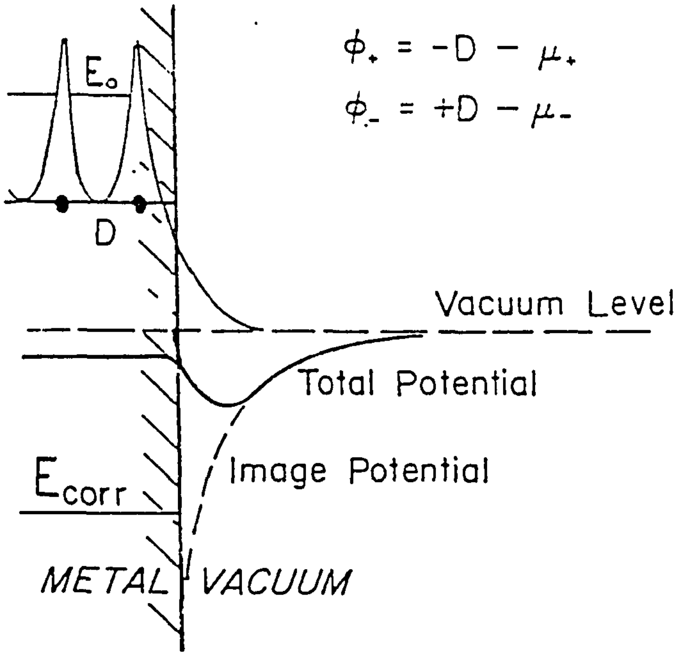

Figure 2.8: The surface potential for thermalized positrons. The positron work function ϕ_+ is determined by the dipole contribution D, the attraction to the electrons E_{corr}, and the repulsion from the ion cores E_0.

During the diffusion motion, some positrons will approach the surface before annihilation. Several interactions processes can occur.

i) Binding to the surface state. For metals, a typical potential well is depicted in fig. 2.8. Thermal positrons approaching the surface will be trapped with a binding energy of 2 - 3 eV. They also may get trapped at defects in the surface, and the binding energy is higher.

ii) Re-emission as a free positron. If the positron does not have time to thermalize in the bulk, and its energy is higher than the positron work function ϕ_+, it can be re-emitted as nonthermal positron (E > k_BT). Thermal positrons can be re-emitted with an energy E = ϕ_+ only if the positron work function is negative, as in W, Ni, or Cu.

iii) Re-emission as nonthermal positrons. If the positrons did not have time to thermalize before reaching the surface, and they have an energy higher than the positron work function, they can be reemitted as nonthermals. This effect is usually seen in a beam of low incident energy (E_{inc} < 4. keV). The signal from these positrons can affect the analysis of the results, and will be discussed in the section 5.2

iv) Positronium emission. If the sum of the electron and positron work functions is less than the binding energy of Ps (6.8 eV), positrons can pick up a surface electron and be re-emitted as Ps or as excited states of Ps (Ps^*, Ps^-). Nonthermal positrons also can pick up an electron and be re-emitted with higher energies.

v) Thermal positronium emission. If the positron is bound to a surface state, or to a defect at the surface, it can be excited and re-emitted if the temperature is high enough. Most metals emit thermal Ps above 0 °C.

vi) Internal reflection at the surface. The alkali metals have low electron density, perhaps reducing the degree to which the electrons penetrate out into the vacuum. This, in turn, tends to create a potential well outside the surface that is too narrow to have bound states.[59] Therefore, a positron reaching the surface will be reflected back to the bulk. In the diffusion model, the reflection is quantified with the parameter β, which is 1 for total reflection, and 0 for a totally absorbent surface.

2.5 Observables

Most research with the liquid metals beam consists of measurement of the nearly antiparallel gamma rays resulting from the annihilation of positrons with core or valence electrons, or in positronium states.

Because of the momentum of the electron at the site of annihilation, the annihilation radiation exhibits a Doppler shift around the mean energy value (511 keV) of the emerging gamma rays. In a metal, typical valence-electron energies are of the order of the Fermi energy (3-5 eV), while core-electron energies are much higher. On the other hand, the energy of a thermalized positron is only a few meV ($\sim$ 0.04 eV). Therefore, the momentum of the positron is smaller than the electron momentum and can be neglected. The gamma rays resulting from the annihilation will have a spread in energy and angle proportional to the momentum of the electron, as illustrated in fig 2.9.

The Doppler broadening and angle distribution of the gamma rays can be easily calculated. The velocity of valence electrons in a solid is $\sim 10^8$ cm/s, which is 2 orders of magnitude smaller than the speed of light. The applicable nonrelativistic equations of motion are:

$$\begin{aligned} 2mc^2 + \frac{1}{2}mv^2 &= E_1 + E_2 \\ mv\sin\theta &= \frac{E_1}{c}\sin\phi, \quad \text{and} \\ mv\cos\theta &= E_2 - \frac{E_1}{c}\cos\phi, \end{aligned} \tag{2.20}$$

where v is the speed of the center of mass of the electron and positron before annihilation, and c is the speed of light. E_1 and E_2 are the energies of the outgoing gamma rays. The angles are depicted in fig. 2.9. From the second and third equation in (2.20):

$$m^2v^2 + E_2^2 - 2m\frac{v}{c}E_2\cos\theta = \frac{E_1^2}{c^2}, \tag{2.21}$$

Substituting the first equation of (2.20) in (2.21) and neglecting the terms of $O(v/c)^2$ and $O(v/c)^4$:

$$-\frac{1}{2}\frac{v}{c}E_2\cos\theta = mc^2 - E_2 \quad \text{and} \tag{2.22}$$

$$E_2 = mc^2\left(1 + \frac{v}{2c}\cos\theta\right). \tag{2.23}$$

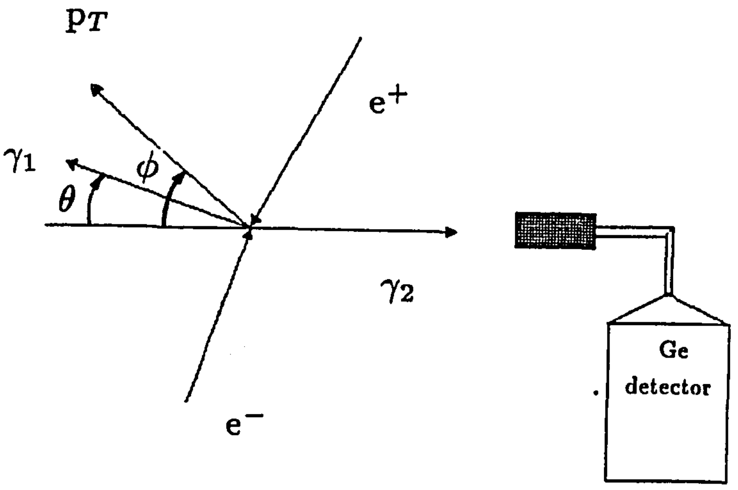

Figure 2.9: Annihilation of the electron and positron and Doppler broadening of the gamma rays arising from the annihilation. P_T is the center of mass momentum of the e^+-e^- pair. γ_1 and γ_2 are the outgoing gamma rays.

If the positron is diffusing freely, there is a large overlap of its wave function that of the the core electron. Therefore, the probability of annihilation with a core electron is higher than annihilation with a valence electron. On the other hand when a positron falls into a vacancy, defect, or at the surface, it loses energy to a valence electron and its wave function is localized in the vacancy . Thus it has higher probability of annihilating with a conduction electron which has lower momentum than the core electron.

Two techniques are used to study the Doppler shift of the annihilating gamma rays. Using a large array of detectors at long distances, the angular distribution of gamma rays can be measured, giving direct information on the momentum distribution of the electrons (integrated in one direction). This is the two-dimensional angular correlation[10–15] technique (2d ACAR).

The second technique, which is used in this study, consists of measuring the broadening of the annihilation peak arising from the gamma rays. The spectrum obtained is a convolution of the energy resolution of the detection system and the doppler broadening of the annihilating gamma rays (figure 2.10).

When positrons annihilate with core electrons, the Doppler broadening is large because of the relatively large momentum of the electrons, and the shape of the peak is broad. The peak is narrow when the positron annihilates with a low momentum electron, as also seen in eq. (2.23)

These two effects are characterized by the lineshape parameter, S, as introduced by MacKenzie *et. al.*[60] S is defined as the area of a central segment of the 511 keV peak divided by the total area (fig. 2.10). These areas are defined at the beginning of the experiment, and are kept fixed throughout. The background underlying the peak is removed by simple linear subtraction. Thus, the S parameter is a measure of the width of the annihilation peak.

A major advantage of this definition of the lineshape parameter is its superposition property. If there are various annihilation modes (in defects, bulk, surface or as Ps), each with a probability f_i, having a lineshape S_i, then the observed S is:

$$S = \frac{\sum S_i f_i}{\sum f_i}. \tag{2.24}$$

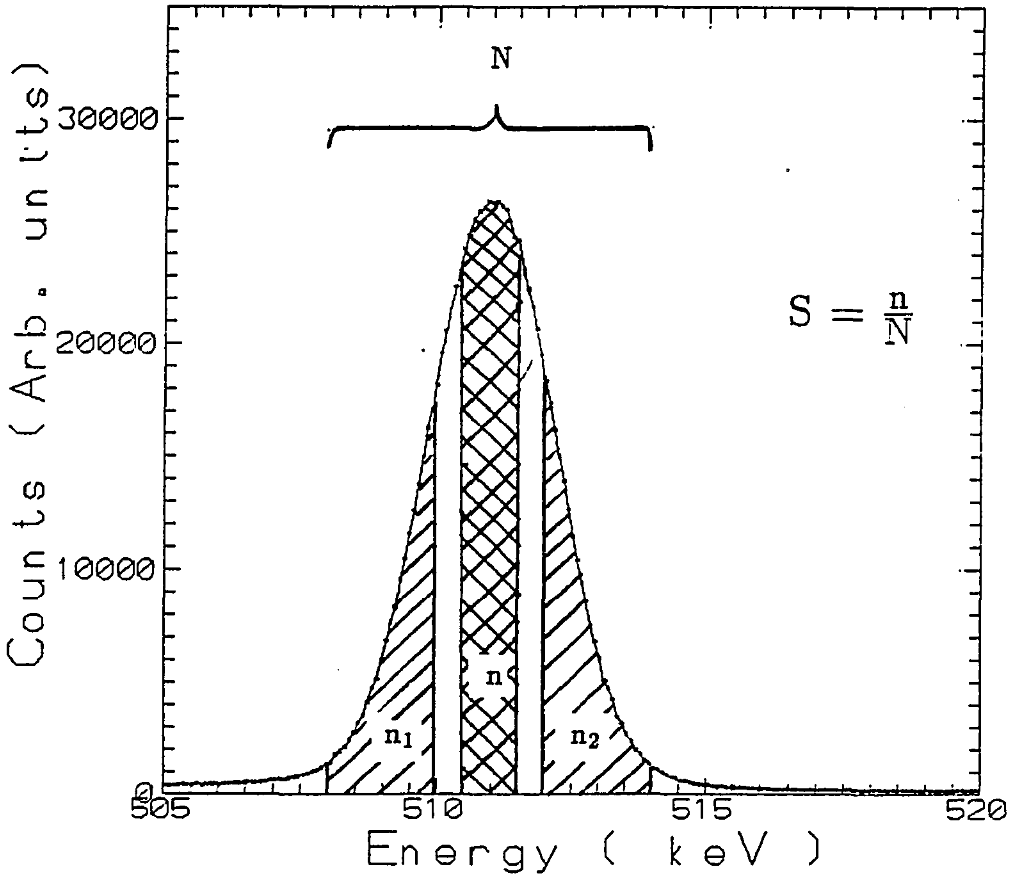

Figure 2.10: Illustration of the areas used for the definition of the S (lineshape) and W (wings) parameter. S = n/N, and W = $(n_1 + n_2)/$ N.

Another property of the *S* parameter is that it can be described by the binomial distribution[61]. The *S* parameter is the ratio of the counts, *n*, in the center of the peak to the total counts *N*, $S = n/N = p$. Thus there are only two classes of events: an event which falls within the central area of the peak or one which falls outside. The probabilities are p and (1 - p). In this situation, the binomial distribution can be used to describe the spectrum,

$$P(n) = \binom{n}{N} p^n (1-n)^{N-n}, \quad n = 0, 1, \cdots, N. \tag{2.25}$$

From statistics theory, the variance is:

$$V(n) = Np(1-p), \tag{2.26}$$

and the standard deviation is:

$$\sigma(n/N) = \left(\frac{n(N-n)}{N^3}\right)^{1/2}. \tag{2.27}$$

For a typical value S = 0.5, the statistical error is $\sigma(0.5) = 0.5/\sqrt{N}$. This value is smaller than $\sigma(0.5) = 0.86/\sqrt{N}$, which results from the addition of errors from independent quantities n and N. This is an advantage of the definition of S that has received little attention in the literature.

The channels to define the S parameter have to be chosen to obtain the maximum sensitivity to defects or surface annihilation. If a wide central region is defined, the statistical error is small, but channels that are sensitive to core annihilation[61] may be included. If the cental region is too narrow, the sensitivity to valence electron annihilation is high, but the statistical error may be too big. A good definition of S which balances these considerations was found[61] to be between 0.4 and 0.6.

The superposition property of the S parameter, eq. (2.24) is essential to study the diffusion length of positrons, because the probability, F_s, of positrons reaching the surface can be obtained by solving the diffusion equation. Its solution is given in eq. (2.14) or (2.16). The probability of positrons annihilating in the bulk is just 1 - F_s. Thus, in an experiment to determine S(E), the measured result will be:

$$S = \frac{S_s F_s + S_{bulk}(1-F_s)}{\Omega}, \tag{2.28}$$

where Ω is a normalization factor defined below, S_s is the S parameter from positrons annihilating at the surface, and S_{bulk} is associated with positrons annihilating in the bulk. The second term, in general has contributions from positrons annihilating in the defect-free bulk, and trapped at defects (vacancies, divacancies, or voids). If f_f and f_t are the free and trapped fraction, the bulk S is given by $S_{bulk} = S_t f_t + S_f f_f$.

The surface term has several contributions. Positrons can annihilate while trapped at the surface state, after forming Ps, or after being emitted as free positrons. Two types of Ps can be formed, each with a different decay scheme. Twenty five percent are Para-Ps, the singlet spin state, that has a short lifetime (~ 125 ps) and decays via two gamma rays. Thus, its signal falls into the 511 keV annihilation peak. Seventy five percent of the Ps are Ortho-Ps, the triplet spin state that has a long lifetime (142 ns), and decays via 3 gamma rays. Thus, the signal has a distribution in energy below 511 keV. Ortho-Ps lives long enough to travel far from the surface, and a small fraction is not detected. Only Para-Ps contributes to the S parameter. Therefore, an expression for S at the surface is given by,

$$S_s = \frac{1}{4} f_o S_{Ps} + (1 - f_o) S_{ss}, \tag{2.29}$$

where f_o is the fraction of positrons arriving at the surface that form Ps. S_{Ps} is the S parameter associated with the fraction $\frac{1}{4} f_o$ of positrons that annihilate after forming Para-Ps (the fraction $(\frac{3}{4} f_o)$ that forms Ortho-Ps does not contribute to S because it is detected in the energy region below 511 keV). S_{ss} is associated with the fraction (1 - f_o) annihilating from the surface state. Because of the low center-of-mass momentum of the Ps atom, the S parameter from Ps is higher than the S parameter arising from valence electron annihilation (S_{ss}).

In all metals that we studied, the fraction of positrons that is reemitted from the sample is small. Thus, the S parameter arising from nonthermal positrons that escape from the sample and eventually return to it can be neglected. The measured nonthermal fraction is discussed in section 5.3.

The calibration factor, Ω, is obtained from the different annihilation modes that contribute to S:

$$\Omega = (1 - F_s) + F_s(1 - \frac{3}{4}f_o). \tag{2.30}$$

The positronium fraction, *i.e.* the fraction of positrons that form positronium for a given incident energy is $F(E) = F_s(E)\, f_o$. Because of the factor Ω in the definition of S, F is a nonlinear function of S.

Another parameter that can be defined from the annihilation peak, is W (wings), which is defined as the counts at the extremes of the peak $(n_1 + n_2)$ divided by the total counts under the peak (N) (Fig. 2.10). Since W is defined from the gamma rays that have large deviation from 511 keV, it will be more sensitive to core-electron annihilation. The statistical and superposition properties of W are the same as S.

A useful combination of the S and W parameters is the R parameter,[62,63] which is insensitive to changes in the fraction of positrons annihilating in each state. R can be calculated from the S and W parameters in the bulk only. If $(1 - S_t)$ and S_t correspond to the S parameter from a free and trapped state respectively, then:

$$S = S_f(1 - f_t) + S_t f_t \tag{2.31}$$

f_t is the probability of annihilation in a trapped state. For W we find a similar relation. Both relations can rewritten as:

$$\begin{aligned} S - S_f &= (S_t - S_f)f_t, \quad \text{and} \\ W - W_f &= (W_t - W_f)f_t. \end{aligned} \tag{2.32}$$

To eliminate the dependence on f_t, the R parameter is defined as the ratio between these quantities.

$$R = \left| \frac{S - S_f}{W - W_f} \right| . \tag{2.33}$$

Thus, R is independent of the concentration of traps, and characterizes the type of traps involved. This analysis is valid when there is only one type of trap involved, or, at least, one type of trap is dominant. However, the R parameter requires a precise knowledge of S_f and W_f in the bulk of the sample. In the liquid metals beam, these values are difficult to obtain for high density metals, because positrons cannot be implanted at energies where they all annihilate in the bulk.

The fraction of positrons that form positronium after returning to the surface[21] also can be determined with the liquid metals beam. Both Para-Ps and Ortho-Ps can be formed outside the surface. The radiation is collected by a Ge detector, and two regions of interest are selected in the energy spectrum: the total T, that has all the counts in the spectrum below the 511 keV peak, and the peak P, that includes only a region under the photopeak. We assume that a fraction, F, of the positrons which annihilate in the sample form Ps. F is the positronium fraction and depends on the incident energy of the positron. If the total number of counts in the spectrum is T_F, and the number of counts in the peak is P_F, we then have:

$$\begin{aligned} T_F &= T_1 F + (1-F)T_o \quad \text{and} \\ P_F &= P_1 F + (1-F)P_o, \end{aligned} \tag{2.34}$$

where we have defined T_1 as the total counts when $F = 1$, and T_o the total number of counts when $F = 0$. P_1 represents the counts under the 511 peak when $F = 1$, and P_o is the peak counts when $F = 0$.

We now define $R_F = (T_F - P_F)/T_F$, $R_o = (T_o - P_o)/T_o$, and $R_1 = (T_1 - P_1)/T_1$, which are independent of the beam intensity. Solving eq. (2.34) for F we find:

$$F = \left(1 + \frac{P_1}{P_o}\frac{(R_F - R_o)}{(R_1 - R_F)}\right)^{-1}. \tag{2.35}$$

To obtain F experimentally, it is necessary to calculate the parameters R_1,

R_o, and P_1/P_o. P_1 and P_o are determined from the counts in the peak when R_1 and R_o are measured. R_o is calculated from the total energy spectrum at high incident energies (when no positrons can return to the surface). R_1 is more difficult to determine, because it has to be extrapolated to zero incident energy, under very clean surface conditions, at high temperature, when all positrons are thermally desorbed as Ps. Even under these conditions, it is difficult to determine R_1 with confidence[44].

2.6 Fitting Procedure

The analysis of the data depends critically on the fitting procedure and the method used to solve the equations numerically for different implantation profiles and overlayers[64].

The fitting routine used in this work, developed by Van Veen *et al*,[65] is a very fast numerical scheme developed to solve the diffusion equation (2.3). This scheme allows fitting a number of parameters related to the implantation profile: m , n and A parameters, mean depth, trapping rates, and electric fields, in layered materials. The positron diffusion parameters are also fitted: S_{bulk}, S_s and diffusion length L_+. The last parameter is defined in term of the lifetime and the diffusion coefficient,

$$L_+ = \sqrt{D_+\tau}. \tag{2.36}$$

The problem is reduced to a single-speed diffusion equation by considering only thermalized positrons, with a source term given by the Makhov profile[31]. The positron density is averaged over time. The equation to be solved is:

$$D_+\frac{d^2N_p(z)}{dz^2} - \frac{d}{dz}(v_dN_p) + I(z) - \lambda_{eff}N_p(z) = 0 \tag{2.37}$$

where $N_p(z)$ is the time averaged positron density, $v_d(z) = \mu E(z)$ the drift velocity, μ the positron mobility, E the electric field strength, I(z) the positron stopping rate, and λ_{eff} the effective annihilation rate of the positron in the bulk.

The boundary condition at $z \to \infty$ is taken at a depth z_f beyond which there are no defects and no positrons are stopped[65]. At the surface, an apparent diffusion length is defined such that:

$$\left(\frac{dN_p}{dz}\right)_{z=0} = \frac{N_p(0)}{L_a}. \tag{2.38}$$

This equation is the same as the boundary condition (2.5), with $\beta = L_a$.

To solve the problem, the sample is divided into intervals $\triangle\bar{z}$ relative to the mean depth $\bar{z}$. Equation (2.37) is solved for each interval. The concentration of defects, the positron implantation profile (eq. 2.1), and the electric field are assumed to vary slowly over the interval, and they can be taken as constant within the interval. This method allows the solution of the equation with a general m and n in the Makhovian profile (eq. 2.1), while the analytical solution to the problem exists only for m = 1 and m = 2. The general solution to eq. (2.37) within an interval is given by:

$$N_p(z) = A\exp(\gamma z) + B\exp(-\gamma z) + p/\alpha \tag{2.39}$$

where A, B and α are constants that are determined from the continuity relations and the boundary conditions at z = 0 and at z = ∞,

$$N_i(z_i) = N_{i+1}(z_i), \qquad N_i'(z_i) = N_{i+1}'(z_i) \tag{2.40}$$

where N' denotes the derivative with respect to z. The solutions obtained from the set of equations (2.40) can be used to calculate the fraction F_s of positrons returning to the surface for a given incident energy, E.

The fitting procedure used to deduce the parameters of the model (L_+, S_s, S_b, m, n, etc.) is varied for the experimental situation. Five models cover most of the problems that are investigated by positron beams.

Model #1: This is a general model that allows any value for all parameters, L_+, S_s, S_b, L_a, S_s, f_o, L_{epi}, S_{epi}, $f_{o,epi}$. The three last values correspond to an approximate treatment of nonthermal positrons following reference 63. Any parameter can be fitted independently.

Model #2: Here, the S parameter (S_b and S_t) is not solved for each interval and is related to the diffusion length and to the concentration of defects. This relation allows to obtain information on the depth profile of the defects.

Model #3: In this case, the diffusion length is coupled to the S parameter in the same way as in model #2. The defect concentration and the electric field are assumed to have a Gaussian depth distribution. The standard deviation of the gaussian, the mean values, and the normalization factors are the fitting parameters. The distribution of defects or electric fields in the sample can be obtained.

Model #4: In this model, the defect concentration is assumed to be distributed in blocks across the sample. The density of the sample is uniform. A layered structure is defined, with different values of the diffusion length and/or the electric field. Continuity conditions are imposed on the diffusion length across the boundary of the layers. The S parameters are coupled to the diffusion length as in model #2.

Model #5: This model is similar to model #1; all parameters can be fitted independently. However a layered structure composed of materials of different density can be treated. An S parameter and diffusion length for each layer is assigned, both values being independent of each other. The S parameter is the weighted sum of S in each layer and the surface, normalized by the the factor defined in eq. (2.30)

Chapter III. Liquid Metals

3.1 Thermodynamics

Liquid metals can be considered as an ensemble of ions and electrons in a disordered configuration. In contrast to solids, there is no medium or long range order and the position of its elements can not be described by a simple function. Short range order is evidenced by the strong peak of the structure factor, or the pair distribution function, as seen in figure 3.1b.

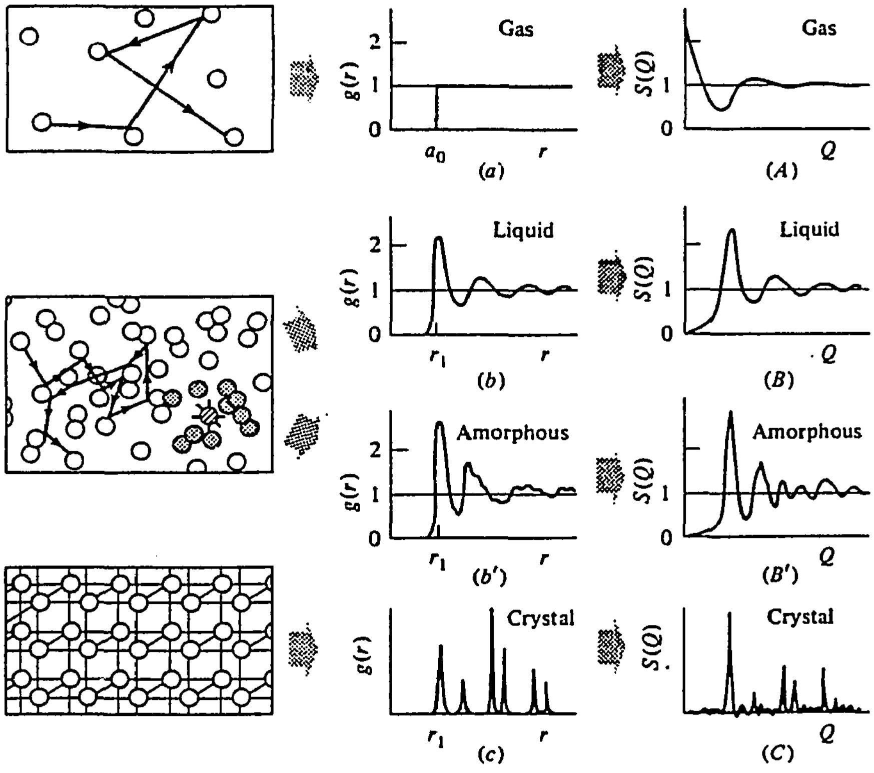

Figure 3.1: Schematic view of the atomic configurations in a gas, liquid, amorphous solid, and crystalline solid. The pair distribution function g(R) and the atomic structure factor S(Q) are shown. From reference 2.

Conversely, in a liquid, the elements are not completely independent as in gases$^{1-5}$. There is a weak positional correlation that indicates interactions between pairs of particles, and the mean free path is shorter than in gases.

The differences between the three states can be seen in figure 3.1. The pair correlation function g(R) as well as the structure factor S(Q) are shown for a gas, liquid, amorphous material, and a crystalline solid.

The ions are assumed to be classical particles with effective potentials between them. A correct description of a liquid metal should consider it as a binary mixture of positive ions and conduction electrons, and proceed by a two component formalism. The ion-ion correlation needs to be calculated in the presence of a free electron gas, which has to be treated quantum mechanically. However, as a first approximation[69,70], it is reasonable to convert the problem into one in which the ions move in an effective force field produced by the electron gas (Born-Oppenheimer approximation). Such method is possible because the electron-ion coupling is weak, and can be regarded as a perturbation to the electron gas. Thus, in a first order approximation, the electron gas density will be taken as constant. In the discussion that follows, we will be concerned mainly with the ion-ion interaction.

The thermodynamic properties of liquids can be studied by specifying two independent quantities, which are generally temperature and pressure. In this way, the connection between the experimentally measured parameters from x-ray and neutron diffraction experiments and the thermodynamic variables can be easily seen.

The partition function of a system of particles, in the *grand canonical ensemble* can be calculated as:

$$\Xi = \sum_N Q_N \exp(N\mu/k_B T), \tag{3.1}$$

where the number of particles N, in the ensemble is not restricted, Q_N is the partition function in the *canonical ensemble*, and is defined as:

$$Q_N = \sum_i \nu_i \exp(-E_i/k_bT) \tag{3.2}$$

where the sum is taken over all possible states of a system with N particles, E_i is the energy of each state, and ν_i is the degeneracy of the state.

The thermodynamical variables are connected to the grand canonical ensemble[67] by the relation:

$$pV = k_BT\ln(\Xi) \tag{3.3}$$

In a similar way, the partition function is connected to the Helmholtz free energy by the relation

$$F = -k_BT\ln Q_N, \tag{3.4}$$

and the total energy can be calculated as[67,68]:

$$E = F - T(\frac{\partial F}{\partial T})_V. \tag{3.5}$$

Let us consider a liquid metal, with a large number N, of elements. The total energy of the system is given by $E_N = \sum_i \frac{1}{2}mv_i^2 + U_N$. The potential energy of the system U_N is a function of the coordinates of the particles, $R_1, ..., R_N$, then the partition function in the canonical ensemble is given by[67]:

$$\begin{aligned} Q_N = \frac{1}{N!}\int \exp(-\sum_j(\frac{1}{2}mv_j^2)/k_BT)dv_1...dv_N \times \\ \int \exp(-U(\mathbf{R}_1, ..., \mathbf{R}_\mathrm{N})/k_BT)d^3R_1...d^3R_N \end{aligned} \tag{3.6}$$

Performing the integral in the velocities, the above expression reduces to:

$$Q_N = \zeta^{3N}Z_N/N! \tag{3.7}$$

where ζ is the partition function for a single molecule, $\zeta = (mk_bT/2\pi\hbar^2)^{1/2}$, $\hbar$ is the Plank's constant divided by 2π, and Z_N is the configurational partition function:

$$Z_N = \int ... \int \exp(-U(\mathbf{R}_1, ..., \mathbf{R}_\mathrm{N})/k_BT)d^3R_1...d^3R_N \tag{3.8}$$

From eq (3.1) and (3.8), the corresponding grand partition function is obtained.

$$\Xi = \sum_N \zeta^{3N} Z_N \exp(N\mu/k_B T)/N!. \tag{3.9}$$

In the *grand canonical ensemble*, the number of particles is not fixed, but fluctuates about a mean value given by[68,69]:

$$\langle (N - \langle N \rangle)^2 \rangle = \langle N^2 \rangle - \langle N \rangle^2 = k_B T (\frac{\partial \langle N \rangle}{\partial \mu})_{T,V}, \tag{3.10}$$

which can also be shown[3] to be:

$$\langle N^2 \rangle - \langle N \rangle^2 = \frac{N^2}{V} \chi_T, \tag{3.11}$$

where χ_T is the isothermal compressibility.

In general, in a disordered system such as a liquid metal, the potential energy can be separated in two parts:

a) The structure-dependent part, which can be expressed as a sum of potentials between pairs of atoms of the form $u = u(R_{ij})$, where $R_{ij} = |\mathbf{R}_i - \mathbf{R}_j|$, is the distance between atoms.

b) The part that depends on the volume of the system, which is independent of the coordinates of the ions, $U_V = N u_V$.

The total energy of a liquid metal can be expressed as:

$$U = N u_V + \sum_{i \neq j} u(R_{ij}) \tag{3.12}$$

Eq (3.8), (3.9) and (3.12) show that the grand partition function is mathematically very complicated because of the potential between pairs of ions. In general, there are no satisfactory simplifications to describe the properties of liquids. In a solid, the periodic structure of the atoms allows the potential to be described in terms of coordinates of the form $\mathbf{R} = \mathbf{a}_1 n_1 + \mathbf{a}_2 n_2 + \mathbf{a}_3 n_3$. In a gas, the configuration is perfectly random, the particles are far apart, and the potential is U $\approx$ 0.

3.2 Correlation functions

In the theory of liquids, a formalism of correlation functions is adopted to avoid the direct evaluation of the configurational partition function, which has a complicated dependence on the coordinates of the particles. In this approach[5], the probability of grouping the particles in two, three or more sets is introduced, and probability functions (or correlation functions) are used to obtain the same information as from direct calculation of the partition function (3.9).

The probability of finding one particle in a volume element d^3R of a constant density liquid is nd^3R, where n is the number density, $n = N/V = 1/v$ of a liquid with N particles in a volume V. Then, n is regarded as the one-body distribution function, $n^{(1)}$, and v is the volume per particle. The next case is the probability of finding two particles in the volume elements d^3R_1 and d^3R_2 separated by a distance $R = \mid \mathbf{R}_2 - \mathbf{R}_1 \mid$. This value is given by $n^{(2)}(R)d^3R_1d^3R_2$, the two-body distribution function or pair distribution function. From probability theory, there are $N!/(N-n)!$ ways to chose n particles out of N. Thus, we have the normalization condition:

$$\begin{aligned} \int n^{(1)} d^3R_1 &= N, \\ \int n^{(2)} d^3R_1 d^3R_2 &= N(N-1). \end{aligned} \tag{3.13}$$

Similar definitions can be made for higher order distribution functions.

For diluted systems, where the positional correlation between the particles is very weak, the distribution functions $n^{(s)}$ become n^s. Thus, it is convenient to define dimensionless quantities called correlation functions, $g_0^{(s)} = n^{(s)}/n^s$. These functions are unity for diluted systems. The connection between theory and experiment is accomplished by the pair correlation function, $g^{(2)}$, which can be determined by x-ray or neutron scattering.

Using the definition of the canonical ensemble, the pair distribution function can be calculated as:

$$n^{(2)} = \frac{N!}{(N-2)!} \frac{\int .... \int \exp(-U/k_BT) d^3R_3....d^3R_N}{Z_N}, \tag{3.14}$$

this equation also can be written as:

$$n^{(2)} = n^2 \exp(-u'(R_{12}/k_BT)), \tag{3.15}$$

where $R_{12} = |R_2 - R_1|$, and $u'(R_{12})$ is the mean potential energy of a pair of particles including the interaction of the other particles in the system. The advantage of writing the pair-distribution function in this form is that for a dilute system, where the $n \rightarrow 0$, it reduces to:

$$n^{(2)} = n^2 \exp(-u(R_{12}/k_BT)), \tag{3.16}$$

because the interaction between the two particles is not affected by the rest of the system, u being the pair potential. However, at liquid densities u is very different than u'. Using formulas (3.4), (3.5), and (3.7), the total energy of the system can be shown to be:

$$E = \frac{3}{2}Nk_BT + \frac{1}{Z_N}\int .... \int U \exp(-U/k_BT) d^3R_1....d^3R_N. \tag{3.17}$$

Combining these last two equations, an expression for the pair correlation function and the energy of the system can be found:

$$E = \frac{3}{2}Nk_BT + Nu_g + n(N/2)\int g_0^{(2)}(R)u(R)d^3R. \tag{3.18}$$

The equation of state, can be obtained differentiating the Helmholtz free energy:

$$\begin{aligned} p &= -\left(\frac{\partial F}{\partial V}\right)_T \\ &= nk_BT - \frac{\partial u_g}{\partial v} - \frac{n^2}{6}\int g_0^{(2)} R \frac{\partial u(R)}{\partial R} d^3R, \end{aligned} \tag{3.19}$$

The normalization condition for the pair correlation function in the grand canonical ensemble can be shown to be$^{1-3}$:

$$\int\int n^{(2)}(R) d^3R_1 d^3R_2 = \langle N^2 \rangle - \langle N \rangle^2, \tag{3.20}$$

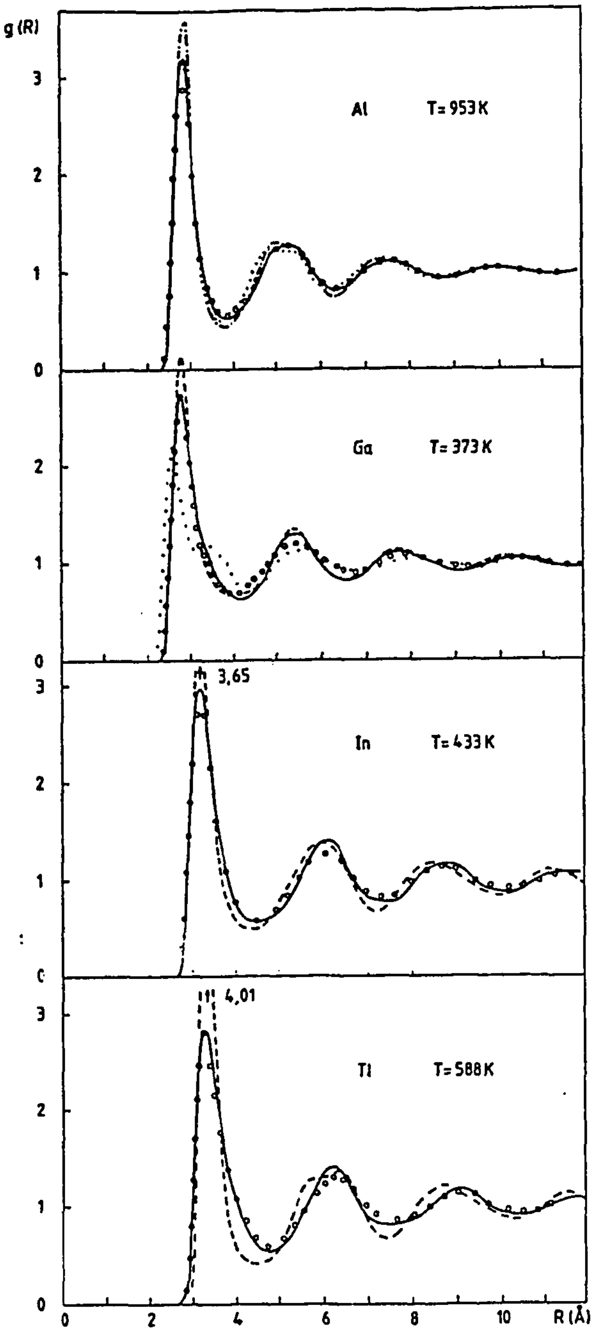

Figure 3.2: Pair correlation function $g_0^{(2)}$ for several liquid, trivalent metals. Calculated with the local empty-core model potential (dotted line), solid and dashed line, optimized nonlocal pseudopotential calculated with relativistic and nonrelativistic core orbitals, from reference 111. The circles are experimental data, Ga is from Ref. 137, Al, In and Tl are from Ref. 2.

Combining (3.20) with equation (3.11), a relation between the isothermal compressibility and the pair correlation function can be obtained

$$1 + n\int (g^{(0)}(R) - 1)d^3R = nk_BT\chi_T, \tag{3.21}$$

this equation can also be written as:

$$1 + n\int h(R)d^3R = k_B\left(\frac{\partial n}{\partial p}\right)_T, \tag{3.22}$$

Where the compressibility (at constant temperature) has been written as $\chi_T = \frac{1}{n}(\frac{\partial n}{\partial p})_T$.

The function $h(R)$ is the total correlation function, $h(R) = g_0^{(2)}(R) - 1$. Equation (3.21) or (3.22) are known as the compressibility equation, which relates the thermodynamic variables to the pair correlation function $g_0^{(2)}$. Figure 3.2 shows the pair correlation function g^2 for severals liquid metals.

3.3 The force equation and the superposition approximation

We now need to relate the pair potentials to the pair distribution function using an integro-differential equation. The mean force that acts on a particle at a position R_1, when there is a second particle at a distance $R_{12} = |R_2 - R_1|$ can be written as $-\nabla_1 u'(R_{12})$, where u' is the mean potential due to the second particle at R_2, and the combined effect of all other particles. This term can be expressed as the force due to the second particle $-\nabla_1 u(R_{12})$, where u is the potential between the two particles. In calculating the force from a third particle, one must calculate the probability of finding a particle at R_3 when particles 1 and 2 are at R_1 and R_2. This probability is given by the three-body distribution function $n^{(3)}$, which measures the probability of finding simultaneously three particles at R_1, R_2, and R_3. Since we already have particles in positions R_1 and R_2, we have to divide by the two-body distribution function $n^{(2)}$; then the force can be written as:

$$\nabla_1 u'(R_{12}) = \nabla_1 u(R_{12}) + \int \frac{n^{(3)}}{n^{(2)}}\nabla_1 u(R_{13})dR_3, \tag{3.23}$$

where $R_{13} = |R_3 - R_1|$. Using relation (3.15), we can write equation (3.22) as

$$k_B T \nabla_1 n^{(2)}(R_{12}) = -n^{(2)} \nabla_1 u(R_{12}) - \int n^{(3)} \nabla_1 u(R_{13}) d^3 R_3. \tag{3.24}$$

This equations links the structure functions $n^{(s)}$, and the pair potential. However, this is only a formal solution to the problem; to solve this equation, one needs $n^{(3)}$. This term can be solved by another integro-differential equation involving $n^{(4)}$, and successive higher order equations are required[2].

3.4 The superposition approximation and the Ornstein-Zernike equation

An approximation to the above solution can be made with the superposition appro- ximation[71], which gives an explicit relation between the second- and third-order distribution functions:

$$n^{(3)}(R_1, R_2, R_3) = n^{(2)}(R_{12}) n^{(2)}(R_{13}) n^{(2)}(R_{23}). \tag{3.25}$$

In this approximation, it is assumed that in a group of three particles, each pair is independent of the third particle. This assumption is true if the density is low, and the particles are far from each other, but this approximation has been shown to be inadequate for liquid densities[72]. This approximation allows us to write (3.24) as an integro-differential equation with only $n^{(2)}$ (or $g_0^{(2)}$) as the unknown variable.[73–75]

Another approach to the solution of equation (3.24) was introduced by Ornstein and Zernike[76]. They view the total correlation function (3.21) as composed of two terms: a direct term $c(R_{12})$, which is a function of the position of two particles, and an indirect term, that describes the correlation of the pair considered with a third particle:

$$h(R_{12}) = c(R_{12}) + n \int c(R_{13}) h(R_{23}) d^3 R_3, \tag{3.26}$$

this equation is only a definition of the direct correlation function $c(R)$, and it is known as the Ornstein-Zernike relation[76] (OZ). Taking the Fourier transform of of equation (3.26) leads to:

$$\tilde{h}(k) = \tilde{c}(k) + n\tilde{c}(k)\tilde{h}(k), \tag{3.27}$$

where the convolution theorem has been used. $\tilde{h}(k)$ and $\tilde{c}(k)$ are the Fourier transforms of $h(R)$ and $c(R)$. Using eq. (3.22), taking k = 0 in (3.27), and re-arranging the terms, (3.27) can be written as:

$$\frac{1}{k_B T}\left(\frac{\partial p}{\partial n}\right) = 1 - n\int c(R) d^3R, \tag{3.28}$$

which is equivalent to the compressibility equation (3.22) showing that a knowledge of $c(R)$ is enough to determine the compressibility of the system. The physical meaning of $c(R)$ for dilute gases is simple. If we introduce (3.16) in the definition of $c(R)$, (3.27), we obtain:

$$c(R) \approx c'(R) \equiv \exp(-u(R)/k_B T) - 1. \tag{3.29}$$

The OZ direct correlation function puts too much emphasis on the region of small k, *i.e.* small angle scattering[3]. Therefore, one must expect the data from small-angle scattering to be of considerable importance when attempting to deduce the pair correlation function from equation (3.28).

3.5 The Perkus-Yevick approximation

A useful approximation to the direct correlation function $c(R)$ is the Perkus-Yevick (PY) approximation[77]:

$$\begin{aligned} c_{PY}(R) &= g_0^{(2)}(R)(1 - \exp[u(R/k_B T)]) \\ &= f(R)y(R), \end{aligned} \tag{3.30}$$

where we have written:

$$\begin{aligned} f(R) &= \exp(-u(R)/k_B T) - 1 \\ y(R) &= g_0^{(2)}(R)\exp(u(R)/k_B T). \end{aligned} \tag{3.31}$$

Using this approximation, the Orntein-Zernike relation (3.25) becomes:

$$h(R_{12} = f(R_{12})y(R_{12}) + n\int h(R_{23})f(R_{13})y(R_{13})d^3R_3, \tag{3.32}$$

3.6 The hard sphere model

The simplest approximation to the potential between pairs of particles is the hard sphere model[1–4], that allows the PY equation (3.31) to be solved analytically. The potential is:

$$\begin{aligned} u(R) &= \infty \qquad \text{for } R < \sigma \\ &= 0 \qquad \text{for } R > \sigma \end{aligned} \tag{3.33}$$

The potential is shown in figure 3.3, where σ is the diameter of the sphere. This model gives the first useful approximation to the short-range interaction between particles that determines the geometrical packing at liquid densities. This model is also very useful for discussing the thermodynamical properties of many simple liquid metals. Its solution was derived by Thiele[78] and Wertheim[79].

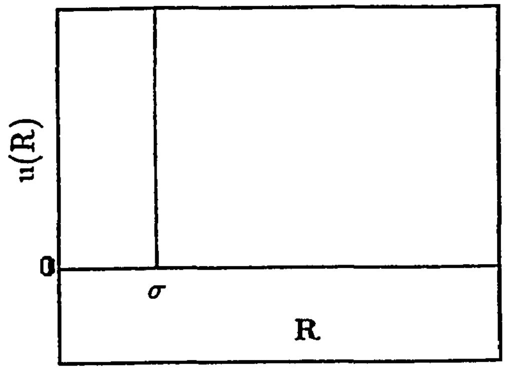

Figure 3.3: The hard sphere potential for liquid metals. σ is the diameter of the sphere.

Using the hard sphere potential, the direct correlation function in the PY approximation can be calculated. The solution is a polynomial in R:

$$\begin{aligned} c_{hs} &= a + b\frac{R}{\sigma} + c\left(\frac{R}{\sigma}\right)^3 \qquad R < \sigma \\ &= 0 \qquad R > \sigma, \end{aligned} \tag{3.34}$$

the coefficients are:

$$a = -(1+2\eta)^2/(1-\eta)^4,$$
$$b = 6\eta(1+\eta/2)^2/(1-\eta)^4, \tag{3.35}$$
$$c = -\eta(1+2\eta)^2/2(1-\eta)^4.$$

These quantities are expressed in terms of the packing fraction η, which denotes the fraction of the total volume occupied by hard spheres:

$$\eta = \frac{1}{6}\pi\sigma^3 n, \tag{3.36}$$

The thermodynamical variables can now be calculated by replacing the direct correlation function (3.37) in the pressure equation (3.19),

$$p_{hs} = nk_BT + \frac{3}{2}\pi n^2 k_B T\sigma^3 g_0^{(2)}(\sigma), \tag{3.37}$$

where we have assumed the term u_g to be constant. The pair-correlation function $g_0^{(2)}$ can be easily evaluated from equation (3.34), and the pressure equation becomes:

$$\frac{p_{hs}}{nk_BT} = \frac{1+2\eta+3\eta^2}{(1-\eta)^2}. \tag{3.38}$$

Because of its mathematical simplicity, the hard sphere model has been well studied. As an example, molecular dynamics simulations[80] determined that the freezing point occurs at a packing fraction of 0.45-0.46. Computer simulations[80,81] of the equation of state are shown to be very close to the results derived with the Perkus-Yevick approximation and the hard sphere potential (equation (3.38)) In general, the compressibility, and thermal pressure coefficients calculated using the hard-sphere model agree well with the alkali metals, but not with other metals[2]. However, the hard sphere model does not approximate well the gas-liquid transition, which requires an attractive part in the potential no included in the hard sphere model.

3.7 The static structure factor

The connection between theory and experiment can be made by the static structure factor, as deduced from x-ray or neutron diffraction experiments. The structure factors derived from these measurements are in qualitative agreement with those calculated with the PY solution for hard-sphere liquids.

Let a liquid metal composed of N ions be illuminated with a monochromatic x-ray beam of wavelength λ. The amplitude of coherent scattering is represented in terms of the atomic scattering factor arising from the electrons associated with each atom. The phase factor of the wave scattered by the ion at $\mathbf{R}_i$ is $\exp[i(\mathbf{k}' - \mathbf{k}) \cdot \mathbf{R}_i]$, where **k** and **k'** are the incident and the scattered wave vectors. The total intensity of the scattered radiation is due to the combined effect of the atoms in a liquid:

$$I(q) = I_0 \left\langle \sum_{i,j} \exp[i\mathbf{q} \cdot (\mathbf{R}_j - \mathbf{R}_i)] \right\rangle, \tag{3.39}$$

where $\mathbf{q} = \mathbf{k} - \mathbf{k}'$, and I_0 is the intensity of scattering from a single atom. If elastic scattering is assumed, with an angle of scattering of 2θ, and, the magnitude of **q** is given by[2]:

$$q = |\mathbf{q}| = \frac{4\pi \sin\theta}{\lambda}. \tag{3.40}$$

The average of equation (3.39) means that $\exp(i\mathbf{q} \cdot \mathbf{R})$ is averaged over all configurations of atomic pairs. Thus, we can use the definition of the pair correlation function (3.14) to calculate the average:

$$N^{-1} \left\langle \sum_{i,j} \exp[i\mathbf{q} \cdot (\mathbf{R}_j - \mathbf{R}_i)] \right\rangle = 1 + n \int g_0^{(2)}(R) \exp(i\mathbf{q} \cdot \mathbf{R}) d^3R, \tag{3.41}$$

The 1 comes from the terms with i = j in the summation. At low densities, when $g_0^{(2)} = 1$, the integral in (3.41) is nearly zero everywhere, except when $q \approx 0$. We can write this equation as:

$$I(q) = N I_0 S(q), \tag{3.42}$$

where we have defined the static structure factor as:

$$S(q) = 1 + n \int (g_0^{(2)}(R) - 1) \exp(i\mathbf{q} \cdot \mathbf{R}) d^3R. \tag{3.43}$$

The inverse of this relation can be obtained with the help of the Fourier theorem:

$$g_0^{(2)}(q) = 1 + \frac{v}{2\pi^2} \int (S(q) - 1) \frac{q \sin q}{R} dq. \tag{3.44}$$

This is the fundamental formula that connects the experimentally measured structure factor S(q) with the pair correlation function $g_0^{(2)}$.

With the help of the δ function, the number density can be written as:

$$n(\mathbf{R}) = \sum_j \delta(\mathbf{R} - \mathbf{R}_j), \tag{3.44}$$

which can be written in terms of the Fourier components $\exp(-i\mathbf{q} \cdot \mathbf{R})$ as:

$$n(\mathbf{R}) = \frac{1}{V} \sum_q n([\mathbf{q}) \exp(-i\mathbf{q} \cdot \mathbf{R}), \tag{3.45}$$

where $n(\mathbf{q})$ is the Fourier transform of $n(\mathbf{R})$:

$$n(\mathbf{q}) = \int n(\mathbf{R}) \exp(i\mathbf{q} \cdot \mathbf{R}) d^3R = \sum_j \exp(i\mathbf{q} \cdot \mathbf{R}_j), \tag{3.46}$$

the last term has been obtained with the use of equation (3.44) Using equation (3.46) in (3.39), and using this result in equation (3.42), we can write the structure factor $S(q)$ in terms of density fluctuations:

$$S(q) = \frac{1}{N} \langle | n(\mathbf{q}) |^2 \rangle, \tag{3.47}$$

At the long wavelength limit, *i.e.* when $q \to 0$, an important relation for the equation of state can be obtained. Taking the limit when $q \to 0$ in equation (3.43) we obtain:

$$S(0) = 1 + n \int (g_0^{(2)}(R) - 1) d^3R, \tag{3.48}$$

Using now the compressibility equation (3.21), we can write:

$$S(0) = nk_BT\chi_T. \tag{3.49}$$

The structure factor $S(q)$ can be obtained by x-ray diffraction, electron or neutron scattering. Some of the advantages and disadvantages of these methods have been discussed by Waseda[2], Vineyard[82], and Enderby[83]. A summary will be given here.

The fundamental difference between neutrons and electrons is that neutrons are scattered by nuclei whose size is smaller than the wavelength of thermal neutrons. Thus, neutron scattering can only determine the ionic configuration in the liquid. X rays are scattered by core electrons, and the ion-ion and ion-electron correlation determine the scattering intensities[84].

The absorption of x-rays in the sample is very large, and increases with high Z elements. Also, the penetration depth in a liquid material is very small. Thus, surface contamination has to be avoided. The samples have to be sealed in low Z material, or studied in vacuum. For neutrons, the absorption is very small, and a large sealed sample should be used.

Multiple scattering events can be important for neutrons, but not for x rays. At small scattering angles, secondary scattering from neutrons is the dominant effect. X-ray scattering is superior at small angles.

The intensity of scattering is larger for x rays than for neutrons. Thus large samples have to be used for neutron scattering.

The scattering process for neutrons is described only in terms of a scattering parameter independent of the scattering angle, which simplifies the analysis. For x rays, the atomic scattering factor and the intensity depend on the scattering angle.

The scattering parameter for neutrons is sensitive to different isotopes, which is a fundamental factor in the study of alloys.

The static structure factor S(q) has been measured for a large number of liquid metals over a wide wavelength range, with x-ray and neutron scattering.

For example, Narten[85] measured liquid Ga, using very careful x-ray and neutron scattering (figure 3.4a). Greenfield made careful X-ray measurements for Na,[86] (figure 3.4b). The general features are similar for all metals, there is a sharp peak followed by several smaller peaks. The physical interpretation is more transparent if we look at the pair correlation function which can be obtained by the Fourier transform of the static structure factor, given by eq. (3.44). This derivation is shown in figure 3.5 for liquid In[90]. At small r, $g_0^{(2)}$ is zero, because the separation between the particles has to be greater than the size of the atoms. The sharp peak at larger R is associated with the distance to the nearest neighbour; the following peaks are associated with the next nearest neighbours. At larger R values, $g_0^{(2)}$ tends towards one, that is, the particles are uncorrelated.

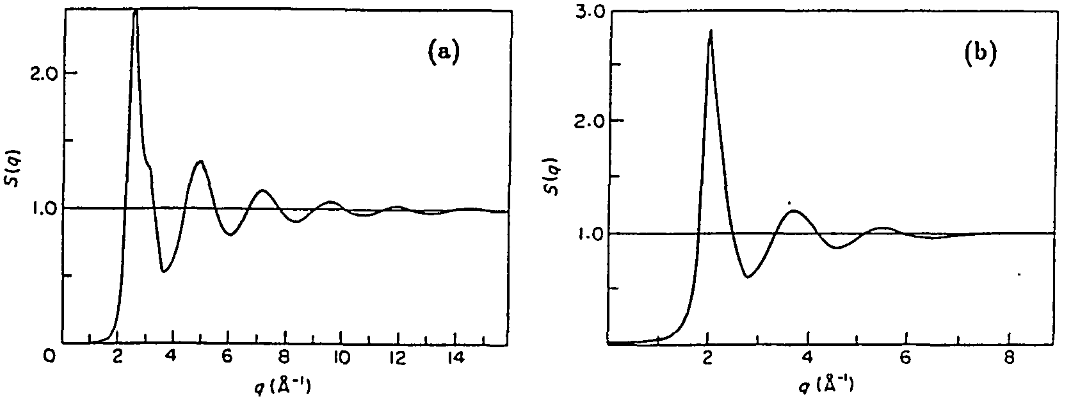

Figure 3.4: a) Static structure factor S(q) of liquid Ga at 20 °C , measured with x-ray and neutron scattering.[85] b) Structure factor of liquid Na at 100 °C using x-ray measurements.[86]

The integral between 0 and r of the pair correlation function gives the number of atoms in a sphere of radius, r:

$$N_r = n \int_0^r g_0^{(2)}(R) 4\pi R^2 dR, \tag{3.50}$$

N_r is called the radial distribution function (RDF). The coordination number, which is defined as the number of nearest neighbours about an atom, can be calculated by integrating the radial distribution function from zero to the position of the first minimum.

For certain metals the results are close to the coordination number in the solid phase,[87] but, in general the number in the liquid phase is smaller than in the solid phase. In close-packed metals the coordination number is 12; for liquid metals it varies[88] from 9 to 11. The difference is related to the random packing of spheres. According to calculations of aggregates of hard spheres[89,57], the random, close-packing fraction is 0.64, compared with 0.74 for crystal close packing. This explains the increase in the volume upon melting that occurs in most metals.

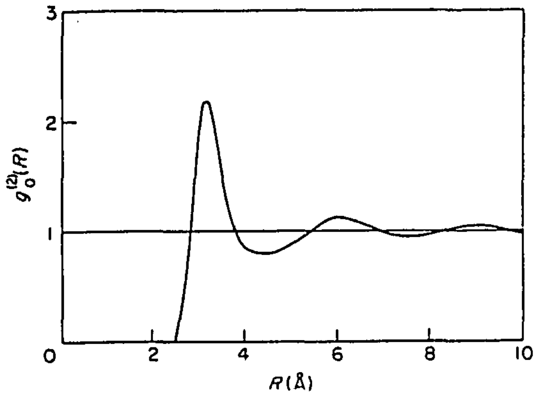

Figure 3.5: The pair correlation function $g_0^{(2)}$ calculated from the measured structure factor S(q) in In[90].

Chapter IV. Experimental section

4.1 Description of the beam:

The Liquid Metals Beam is a magnetically guided positron beam designed to study the interaction of positrons with low vapor-pressure liquids at ultra high vacuum. Positrons are obtained from a radioactive source and are moderated to a few eV. Subsequently, they are guided to the sample and implanted at the desired energy. The resolution of the beam is 1 eV at 200 eV. The transport system, consisting of 9 coils that magnetically guide the positrons to the target, is mounted vertically to allow study of liquid samples. The four main chambers are schematically shown in figure 4.1.

1.- The upper chamber has a 70 mCi radioactive source that produces the positrons. A ^{22}Na source decays into ^{22}Ne, releasing a positron and a gamma ray of 1270 keV of energy. These gamma rays are shielded from the detector by a heavy metal shield placed inside the chamber, and lead sheet outside the vacuum chamber.

The emitted positrons have a broad energy distribution, with mean energy of $\approx$ 150 keV, and maximum energy of $\approx$ 450 keV. These positrons are moderated by a tungsten film of $\sim$ 5000 Å coupled to an inverted tungsten cone. The advantages of this configuration will be discussed in section 4.3. The conversion efficiency from fast to slow positrons with this geometry is approximately 10^{-4}. The negative work function of W allows the positrons reaching the surface to be re-emitted into the vacuum. These positrons have a narrow angle and a narrow energy distribution.[91] A diagram of the source chamber, source, moderator, and accelerator tubes is shown in figure 4.2.

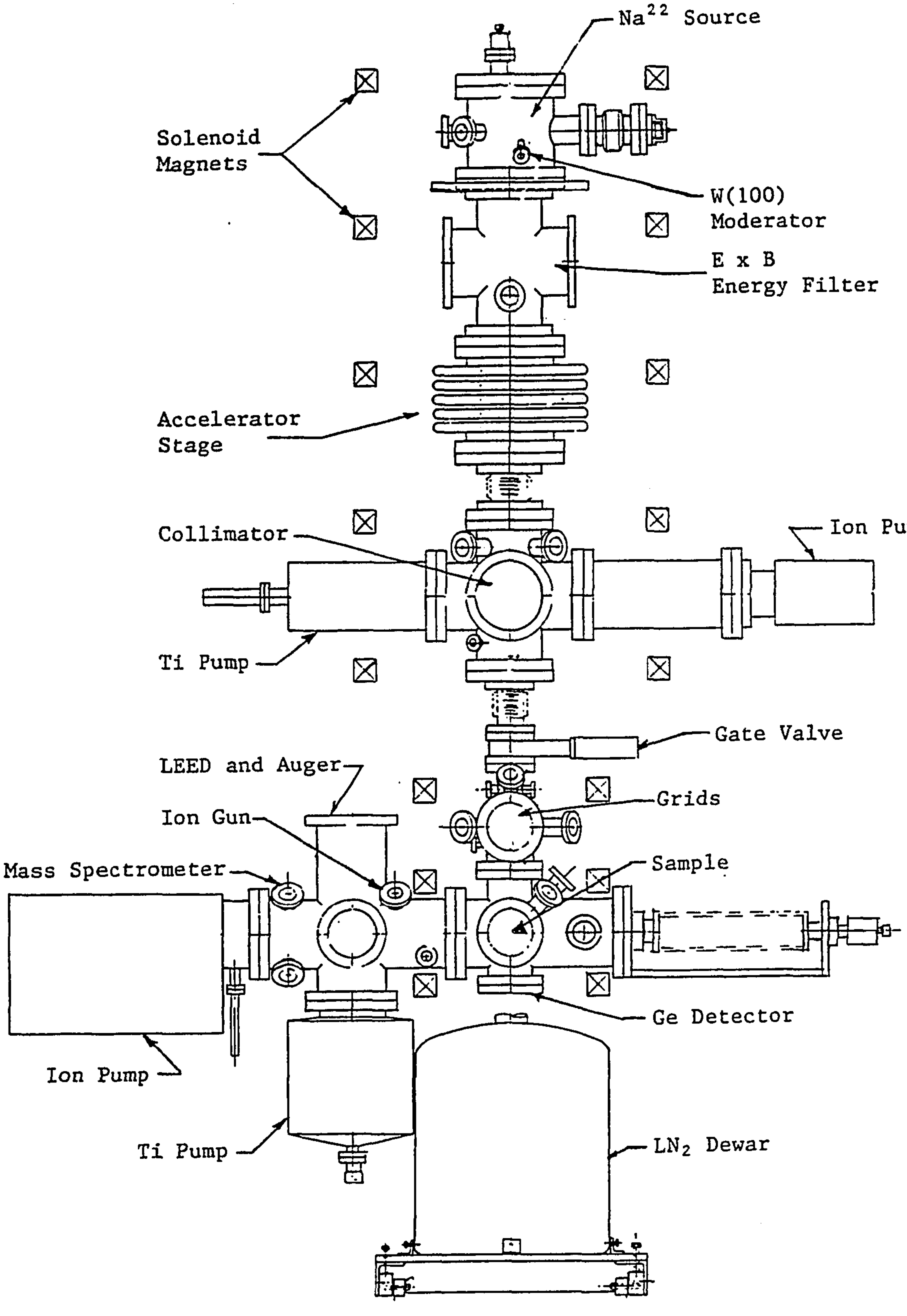

Figure 4.1: Schematic view of the Liquid Metals Beam. The source and moderator are placed at the top. The sample is placed in the bottom chamber. Positrons are guided into the sample by an axial magnetic field.

The source and moderator are mounted on a linear feedthrough of 1 and 2 inches respectively, so that their relative positions can be easily adjusted. The maximum positron yield is obtained with the moderator in contact with the source and at the same potential. The moderator can be moved away from the source, to a position where it can be annealed with an electron gun. Because there are no pumps close to the electron gun, annealing has to be done slowly, to allow the gases released by heating to be pumped down. The annealing temperature in the beam should be ~ 800 °C.

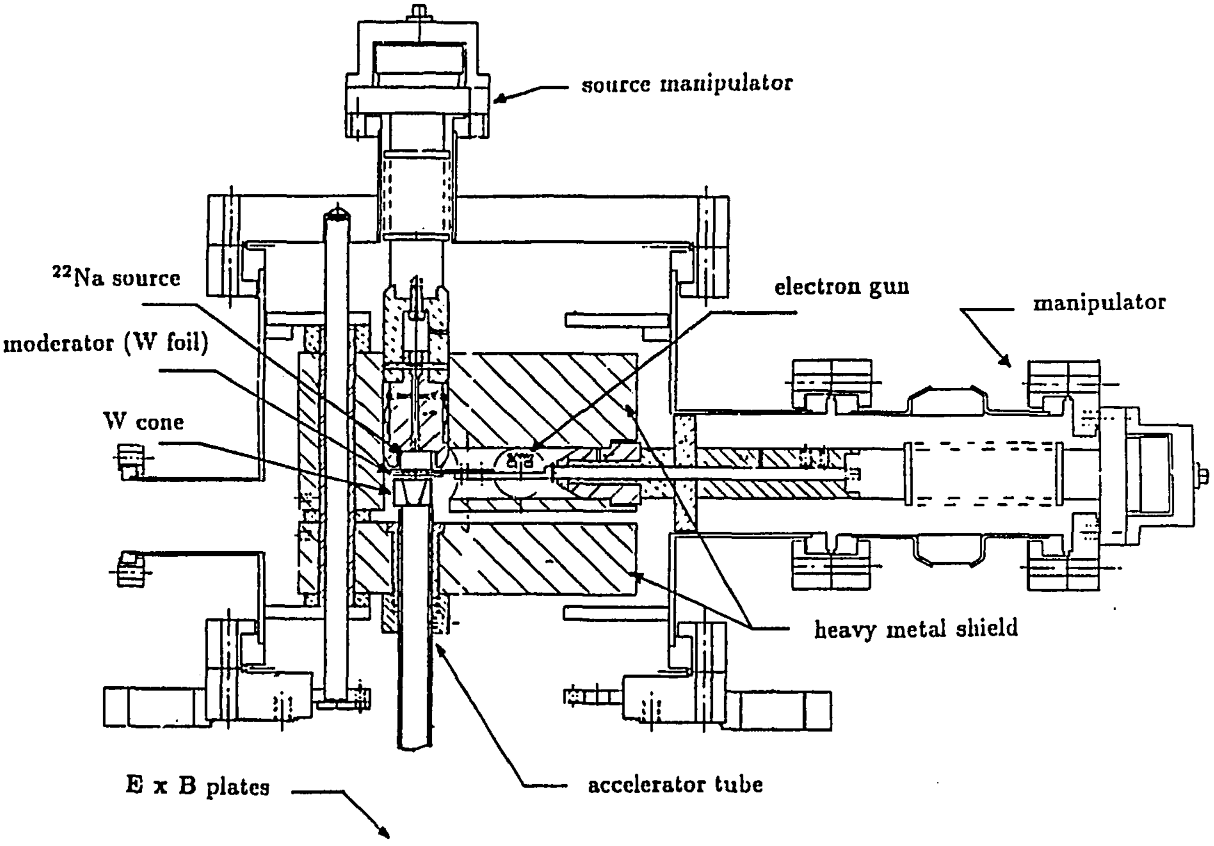

Figure 4.2: Diagram of the source chamber, the source, moderator geometry and accelerator tube. The E × B plates are placed below the accelerator tube.

Below the moderator and source there is a chamber that contains the **E**× **B** plates. On each side of the plates there is tube that creates an homogeneous acceleration field. To prevent the fast positrons and gamma rays from reaching the detector, the source and moderator are displaced 1 inch from the axis of the beam. The **E**× **B** plates act as a velocity filter that deflects the positrons towards the axis of the beam. Two collimator disks made of heavy metal are located on each side of the **E**×**B** plates, so that there is no direct path from the source to the sample.

In standard, flat, **E**×**B** filters, the positrons acquire a drift velocity given by $\mathrm{v} = \mathbf{E}\times\ \mathbf{B}/\mathrm{B}^2$, and their deflection depends on the time spent inside the plates. The velocity is given by $\mathrm{v} = \sqrt{2E/m}$. In the Liquid Metals Beam, the energy of the reemitted positrons is $\approx$ 3 eV. Thus, the positrons are deflected horizontally 25 mm. Fast positrons ($\mathrm{E} > 50$ keV) coming directly from the source are deflected only a few mm and annihilate in the lower collimator plate.

When the diameter of the beam is comparable to the separation between plates, the shape of the beam is distorted.[92] There is a substantial potential gradient across the beam profile inside the **E**×**B** plates that broadens in the longitudinal positron momentum. This produces a spread in the transit times which results in a distortion in the beam profile, as seen in figure 4.3.

The curved **E**×**B** plates were designed to prevent this distortion. A computer simulation[92] shows the distortion by flat plates and the result using curved plates (Fig. 4.3a and Fig 4.3b respectively).

The source and **E**×**B** chamber can be floated up to 25 kV with a high voltage power supply. The moderator, source, and chamber are all electrically isolated from each other and from ground. Up to 7000 V can be applied to the moderator and source, and have the chamber grounded without short circuits. The normal running configuration has the source, moderator and chamber electrically connected.

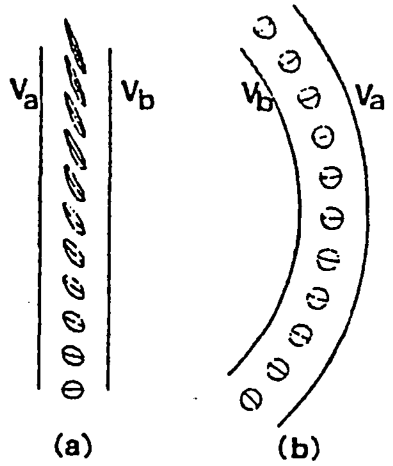

Figure 4.3: Cross sectional view of the flat and curved **E**×**B** plates. a) Beam distortion due to flat plates. b) No distortion ocurrs in curved plates. (from ref. 92).

Three low-voltage power supplies are connected to the chamber and isolated from ground. They are used to bias the **E**×**B** plates and two extraction tubes. Below the source and **E**×**B** chambers there is an accelerator stage that electrically isolates the top chambers from ground. This stage also provides an evenly spaced electric field gradient that helps prevent distortion in the beam.

2.- The center chamber is designed so that a collimator tube can be inserted to protect the moderator and source. Some of the metals studied (Na, Bi, Pb) have high vapor pressure, and, at high temperatures, part of the sample evaporates and may be deposited on the moderator or source, thus decreasing the beam rate. Even worse, deposited metals can corrode the window of the source and create a contamination hazard. The collimator has several 6-inch tubes of different diameters. A rotary mechanism allows tubes with diameters ranging from 5 to 11 mm to be interchanged without breaking the vacuum. If necessary, the tubes can be cooled with liquid nitrogen to increase the sticking coefficients of the gases passing through them.

A 60-liter ion pump and a titanium pump are located on either side of the collimator.

The two top chambers are separated from the bottom chamber by a gate valve. This valve is kept closed to maintain the source and moderator under vacuum while the sample is being changed. It is also desirable to close it during argon sputtering.

3.- The lower chamber (target chamber) contains the sample, a turbo pump, and the Ge detector. Measurements are made in this chamber.

The sample is mounted in a manipulator that allows 36 inches of forward travel. It can also be moved laterally and horizontally, as well as rotated to allow precise alignment of the sample and beam. The temperature is measured with two type-K thermocouples, the first normally mounted in the boat that holds the sample, and the other on top of the heater. The heater is a non-inductively wound W wire isolated from the sample holder by ceramic beads placed below the sample. The maximum sample temperature that can be reached with the heater is $\sim$ 600 °C. Temperature fluctuations depend on the temperature of the sample. For $T > 150$ °C, fluctuations from the set point are less than 1 degree. At lower temperatures, the fluctuations are 2 - 5 °C. There are four electrical connections to the sample; two are attached to the heater, and two can be used to bias the sample. For cooling, there is a liquid nitrogen line that fills a small dewar close to the sample, which cools a copper braid connecting the dewar to the sample. The lowest temperature that can be reached is $\approx -100°$C:

Outside the chamber, on one side of the sample, there is a high purity intrinsic Ge detector. It is used for Doppler broadening and positronium fraction measurements. It operates at liquid nitrogen temperatures in order to lower the leakage current and, hence, the noise of the system. The high purity Ge has been made into a diode capable of withstanding high reverse bias voltages (typically 3500 V). Electron-hole pairs produced by the absorption of a gamma ray are driven to opposite sides of the detector by an electric field. The current pulse is integrated by a charge-sensitive preamplifier that produces an output voltage pulse of height proportional to the incident energy of the gamma ray. The resolution obtained with this type of detector is 1.4 keV FWHM at the 477 keV peak of ^{7}Be. The collection efficiency is $\sim$ 35 %.

Below the sample there is a photodiode coupled to a CsI(Tl) scintillator that is used to monitor the stability of the beam. If, at any time, the beam misses the sample, positrons will annihilate in the bottom of the chamber, close to this detector, increasing the count rate. The detector is used to tune the magnets for different incident energies.

On the opposite side to the detector, there is a 60-liter turbomolecular pump that handles the gas load when the sample is liquid. This pump keeps the vapor from the sample from reaching the low energy electron diffraction (LEED) and Auger system.

4.- The analysis chamber is located on the side of the sample chamber, in line with the manipulator, so that the sample can be moved from the target to the analysis chamber. A shutter separates both chambers, preventing the vapors from the sample from reaching the LEED-Auger apparatus. This chamber contains an electrostatic retarding field Auger analyzer and LEED system. Liquid samples present geometric constraints; the sample surface must be horizontal. Therefore, the surface analysis system must be useable without rotating the sample. This configuration is achieved by mounting the LEED-Auger system in a vertical position.

In this chamber there is also a 200 liter ion pump, quadrupole mass spectrometer, and an ion gun. A leak valve is connected to this chamber to introduce argon gas for sputtering. An ion gauge is also located in this chamber, and the pressure at which the data is taken is typically 1×10^{-9} Torr. The mass spectrometer can be used to look at vapors released from the hot sample. This is an alternative method to detect impurities in the surface of the sample, and it also serves as a very sensitive leak detector.

The normal cleaning procedure consists of sputtering the sample with Ar, (20 μA at 2000-3000 V), at a pressure of $\approx 5 \times 10^{-4}$ Torr. The sputtering time and energy of the ion beam depends on the type of sample, and the impurities present. In most cases, the surface is oxidized.

Next, the sample is annealed for several hours to get rid of any Ar atoms adsorbed on the surface. The annealing temperature also depends on the sample. If the surface looks clean after annealing, an Auger study should be done. The size of the electron beam is less than one mm^2, and it is desirable to study on several places on the sample where contamination is suspected. The electron beam current is typically 20 μA at 3000 V. If the sample still has impurities, the cleaning procedure must be repeated.

Beam transport is achieved with a magnetic field of $\sim$ 100 gauss produced by 9 solenoid magnets. A gradient in the field is established to create a focusing effect that reduces the cross sectional area of the beam at the sample. The field is weaker in the top chamber (close to the moderator) and stronger at the sample.

The current in the solenoids positioned above the sample is controlled by the computer. When the incident energy of the beam is changed, the area of the spot and its position changes slightly. To correct this effect, the magnetic field produced by two magnets above the sample is adjusted for each implantation energy. The effective diameter of the beam at the the sample is $\sim$ 3 mm. The beam moves sideways less than 2 mm when the energy varies from 100 eV to 25 keV.

4.2 Data acquisition system

The data acquisition system for S, W, and F parameter measurements consists of an intrinsic Ge detector, a silicon photodiode coupled to a scintillator, and external electronic circuits (figure 4.4).

The photodiode detector is positioned at the bottom of the beam, below the sample, to monitor the count rate at the bottom of the beam. An increase in the count rate indicates that the beam is bypassig the sample. The Ge detector is used for the high resolution measurements of the 511 keV gamma rays and is positioned ≈ 5 cm from the side of the sample.

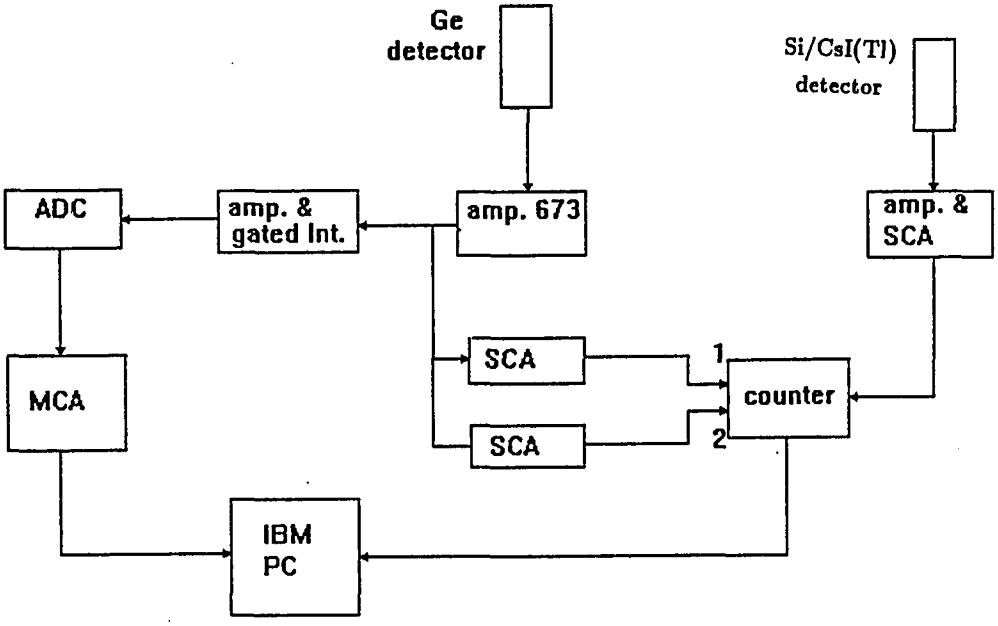

Figure 4.4: Block diagram of the electronic data acquisition system of the Liquid Metals Beam.

The output from the Ge detector is fed into a shaping amplifier, (Ortec 673). One output of the amplifier is fed into a biased amplifier and gated integrator (Ortec 444), which amplifies the region of the spectrum around 511 keV. The spectrum starts at 500 keV and ends at 590 keV. The outputs from the 444 amplifier are fed into an analog-to-digital converter (ADC) Canberra 8077, and finally, into the multichannel analyzer (MCA); the S and W parameters are taken from the MCA.

The second output from the shaping amplifier is fed into a single-channel analyzer (SCA) with a window around 511 keV. The third output is fed into another SCA with a window that starts at $\approx$ 100 keV and ends at $\approx$ 520 keV. The outputs from both SCA go to a counter (Ortec 974). These data are used to calculate the positronium fraction. Annihilation radiation from Ortho-Ps falls into the SCA with the wide window, and annihilation radiation from Para-Ps falls into the SCA with the narrow window. The F parameter can then be determined by the procedure described in section 2.5.

4.3 Development of positron moderators

Moderator efficiency is an essential factor in developing low-energy positron beams. A high flux of positrons allows the study of surface and bulk properties of the sample in a reasonable time span. The geometry, as well as the technique used to prepare the moderators are important factors in the efficiency obtained.[93]

The efficiency of a moderator is defined[93] as the ratio of slow positrons emitted by the moderator and the number of positrons emitted by the source (calculated from its activity). Characterizing moderators in this way is somewhat imprecise, and does not separate the properties of the moderator from those of the source, but the definition was adopted because the self-absorption of the source and the number of positrons backscattered by the substrate into the moderator are not well known.

We will discuss some geometries currently used in positron beams, and the preparation technique of forward re-emission geometry, *i.e.* when positrons are re-emitted from the surface opposite to the source, using a thin foil or cone.

Different geometries are shown in Fig. 4.5

a) The most common configuration is the back-reflection geometry[94] (figure 4.5a). A piece of single crystal, W, is placed in front af a ^{58}Co source plated on a W needle. The positrons are implanted into the W crystal. After thermalization they diffuse back to the surface, where they are reemitted with the energy of the positron work function ($\sim$ 3 eV). The efficiency obtained with this geometry is $\sim 2 \times 10^{-3}$. One disadvantage of this method is the short lifetime of the ^{58}Co source, $T_{1/2}$ = 70.8 days; it has to be replaced often. In addition, only 15 % of the decays results in positrons. Another disadvantage is that a significant fraction ($\sim$ 20%) of the emitted positrons are captured by the source on their drift path out of the moderator. Therefore it is desirable to use the smallest source possible. ^{22}Na can not be used with this geometry because it can not be made in small sizes. ^{22}Na has a high β decay fraction (90 % of the decays are positrons), and long lifetime, $T_{1/2}$ = 2.6 years.

b) Venetian Blinds[95,96]: This moderator (Fig. 4.5b) is made of several polycrystalline parallel W films equally spaced, with the surfaces at an angle to the incoming positrons. This geometry provides a large area for moderation, and large ^{22}Na sources or a LINAC can be used to produce the positrons. In the later case a Ta plate of thickness ranging from 0.3 - 2.5 cm is used to create electron-positron pairs from the incoming electrons. This type of moderator is difficult to make because it has to be made with polycrystalline W foil, which has lower efficiency than single crystal W foils. The efficiency obtained with this geometry[95] is $\sim 9 \times 10^{-6}$.

c) Solid rare-gas moderator: This moderator is used with a ^{22}Na source (other sources could be used, e.g. ^{64}Cu) in thermal contact with a cone or a cylinder but electrically isolated[22,97] from them. The system is cooled to $\sim$ 7 °K, and a thin layer of Ne is deposited on top of the source and cone. Positrons implanted in the Ne layer will quickly lose energy by ionizing radiation and the creation of e-hole pairs. The band gap of insulators limits the minimum energy that a positron can reach, below which phonon excitation is the only available mechanism to lose energy. Positrons with less energy have high mobility and are likely to escape from the solid. The cone or cylinder increases the area available for moderation. This configuration is shown in figure 4.5c

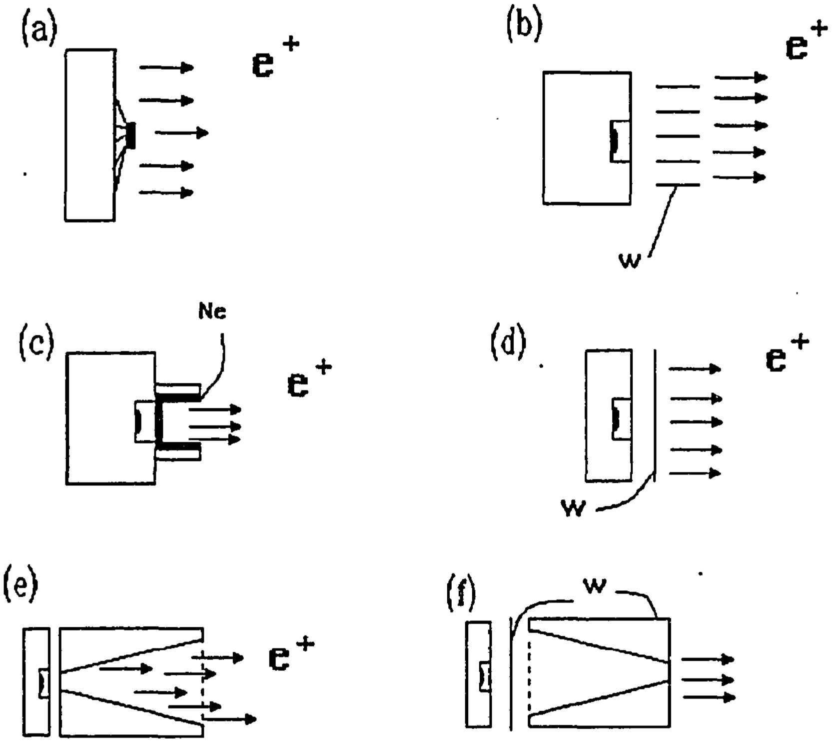

Figure 4.5: Some of the different geometries actually in use in positron beams. a) Back-reflection geometry, b) Venetian blinds, c) Solid neon moderator, d) Thin foil, e) Cone, and f) Thin film and inverted cone.

The disadvantage of this set-up is that it requires that the the moderator/source assembly be cooled and operated under ultra high vacuum. The efficiencies obtained are very high[97]: $\sim 7 \times 10^{-3}$

d) Thin film: This geometry is the simplest of all used (figure 4.5d). It requires a thin film of 0.1 to 1.0 μm thickness that can be made of several crystalline or polycrystalline materials[93,98]. The source is placed on one side of the film and the slow positrons re-emerge on the opposite side. A thin film can be easily used for remoderation because a favorable configuration of electromagnetic fields is easily obtained.

Gramsch *et. al.*[93] compared several different thin films. The films were prepared by annealing to temperatures close to their melting points several times, at a pressure of 5 x 10^{-8} Torr. The measurements were taken with a calibrated ^{22}Na source of 0.9 mCi. For W films, the annealing procedure consisted of heating to $\sim$ 2000 °C for 2-3 min, then cooling to 1600 °C for 15 min, and repeating this step 3 times. The film was annealed in a separate chamber at a pressure of 5×10^{-7} Torr, then was transported in air to the beam were the tests where done. For Ni films, the annealing was done ***in situ*** at $\sim$ 1400 °C several times.

The highest efficiency was obtained[93] with a Ni(100) single crystal of 0.3 μm. A disadvantage is that Ni does not stay clean for long in a vacuum of 5 $\times 10^{-8}$ Torr, and the efficiency decays after a few days. High efficiencies also were obtained with a W(100) single crystal, whose efficiency remains stable in high vacuum (10^{-7} Torr). This crystal can also be exposed to air without losing efficiency. The efficiency of polycrystalline films is 50 % less than single crystal W or Ni, but these films are more rugged and are commercially available. Single crystal W or Ni are not readily available and their production requires specialized equipment.

The slow positron yield from a MgO crystal has been measured by Mayer *et. al.*[99] The crystal was prepared as follows. A 1 x 1 x 0.3 mm^3 MgO plate was etched to a thickness of $\sim$ 50 μm. To make electrical contact between the film and the source, and reduce charging problems, a copper film of $\sim$ 2 μm was evaporated on the source side of the moderator. The positron yield was measured after heating the moderator with an electron gun. The efficiency obtained for this crystal was 2 x 10^{-5} The efficiency of different thin-film moderators is summarized in table 4.1.

Improvements in the efficiency and in the energy resolution of the re-emitted positrons from a thin film can be obtained using an inverted W cone in front of the film (figure 4.5f), as discussed by Wu *et al.*[100] With a film, a large fraction of the positrons (~ 77 %) are transmitted without losing much energy. This method improves the efficiency by forcing the transmitted positrons back to the to the film, so they can be moderated. Improvements from 50 % to 150 % have been obtained for cones with different shapes.

e) Cone moderator: In this configuration (figure 4.5e), a truncated cone is spark-cutted from a W or Ni single crystal rod.[101] Subsequently, it is annealed by a similar procedure as that used for the films in iv).

The cone is placed in front of the source (the smaller opening facing the source) on an x-y-z manipulator. Its position is adjusted until the best efficiency is obtained. A grid placed in front of the cone with a high extraction potential is needed. The magnetic field in the area of the cone has to be lower than the rest of the beam, because the cyclotron radii of positrons leaving the cone decrease with distance from the point of origin. Consequently, the fraction of positron trajectories which intersects the cone surface adjacent to the point of reemission is reduced.

This configuration has high yields of positrons, with an efficiency in the range of 1.2 to 1.5 x 10^{-3}. Because a high extraction potential and nonhomogeneous magnetic field is needed, the energy resolution of the beam is not as good as with a single foil.

Table 4.1: Comparison of different moderators and the efficiency obtained for the source/ moderator system. The efficiencies are taken from the papers quoted in the references.

Moderator	efficiency	reference
W backscattering	2×10^{-3}	94
Venetian Blinds	9×10^{-6}	95,99
Solid rare gas		
cone	7×10^{-3}	97
cylinder	5×10^{-3}	22
W(100) thin film	5.9×10^{-4}	93
W polycrystalline	2.6×10^{-4}	93
Ni(100) thin film	6.6×10^{-4}	93
Ni polycrystalline	2.5×10^{-4}	93
Cu polycrystalline	8.5×10^{-6}	93
Ta polycrystalline	3.5×10^{-5}	93
Mo polycrystalline	7.5×10^{-5}	93
Nb polycrystalline	3.1×10^{-5}	93
MgO(100) thin film	2×10^{-5}	99
W(100) with an inverted cone	1.0×10^{-3}	100
W cone	1.5×10^{-3}	101

Chapter V. Results

5.1 Temperature dependence of S and F

We have studied several liquid metals in an attempt to identify the different variables that contribute to the diffusion motion. As with solids, it is expected that positrons will diffuse freely or be trapped at defects or at the surface of a liquid. In each case, the interpretation of the results will differ.

The metals studied can be classified according to the the state of the positron in the solid phase. The first group is metals in which thermal vacancy trapping has not been observed in the solid phase, either by lifetime[16,102,16] or by angular correlation[12,14,103–105]; these metals are Ga, Bi, Na, and Sn. The second group is metals where experiments have shown positron trapping at thermally generated vacancies: namely Pb and In. Some properties of the metals studied which are relevant to the experiments are presented in table 5.1.

Table 5.1: Lattice structure and other physical characteristics of the metals under investigation. orc = orthorhombic, rhl = rhombohedral, bcc = body-centered cubic, fct = tetragonal, fcc = face-centered cubic. V is the volume of the ion core in the lattice, Z is the number of valence electrons. Trapping refers to trapping in thermally generated vacancies in the solid phase.

Metal	Lattice	Z	T_m °C	Trapping in vacancies
Ga	orc	3	29.8	no
Bi	rhl	5	273.3	no
Na	bcc	1	95.7	no
Sn	fct	4	232.0	no
Pb	fcc	4	327.5	yes
In	fct	3	156.6	yes

Because of their charge, positrons are repelled by the atomic nuclei in the lattice. The potential energy of a positron in a metal is minimal at the interstitial space of the lattice, and increases as the positron approaches the ion cores. Thus, the probability of finding a positron in the interstitial space or at vacancies is higher than the probability of finding it near the ion cores. The details of the potential energy depend on the characteristics of the lattice[106], as well on the relative size of the nuclei.[107] Table 5.2 shows, the bulk lifetime at room temperature and the lifetime just below the melting point. In metals where vacancy trapping is not observed, the lifetime remains constant with temperature. The binding energy of positrons to vacancies is also shown.

Table 5.2: Experimentally measured bulk lifetime of positrons in solid and liquid metals. E_v is the binding energy of a positron to a vacancy in the metal, from reference 117

Metal	τ_b (ps) T=22 °C	τ_b (ps) $T < T_m$	τ_b (ps) $T > T_m$	Ref.	E_v (eV)
Ga	190(5)	190(5)	260(6)	16	2.65
Bi	258(3)	258(3)		105	
Na	263(5)	263(5)	278(5)	16	0.02
Sn	202(5)	202(5)		102	2.64
Pb	201(5)	275(5)		108	3.44
In	220(4)	280(5)	260(4)	109	2.55

If positrons are not localized, the motion can be interpreted in terms of scattering from ions or electrons. If they are trapped, the interpretation has to be made in terms of hopping or tunneling between traps, similar to the self-diffusion process of ions in liquids[1-3]. In metals where vacancy trapping was observed in the solid phase, we can expect trapped positrons also in the liquid phase.

In metals where trapping was not observed in the solid phase, trapping can or canot occur in the liquid phase. In some solid metals, the traps are too shallow to have bound states because the ion cores are too far apart compared to the mean distance between atoms.[107]. In other metals the ions relax arround the trap reducing the binding energy of positrons. In the liquid phase, it is likely that there are traps with varying sizes. Therefore, trapping is likely to happen. For untrapped positrons, the diffusion motion could be related to ion scattering, as in the solid phase. A more detailed discussion with be given in the conclusions.

5.1.1 Measurements of S and F as function of temperature for Ga, Bi, Na, and Sn

Gallium

Gallium has been studied using bulk positron lifetime[16] and angular correlation techniques[104]. Previous experiments[110] on liquid and solid Ga using a positron beam did not show a significant difference between the solid and liquid phase. Gallium is an interesting metal to study because it has a low melting point, 29.8 °C, ant it contracts 3.1 % on melting, its vapor pressure at 500 °C is only 2 x 10^{-9} Torr. These characteristics allow studies over a large temperature range in the liquid phase at ultra high vacuum.

The Ga sample was obtained from ROC/RIC, Ca, 99.999 % purity. Before placing in vacuum, Ga was etched in 50 % nitric acid, 50 % distilled water, until a shiny surface was obtained. The etching procedure is described in reference 144. It was cooled under vacuum to -10 °C, sputtered with argon at a pressure of 4 x 10^{-4} Torr for 1 hour and then annealed at 500 °C for 12 hours. No trace of contaminants was detected with retarding field Auger electron spectroscopy, (figure 5.1).

The temperature was controlled and measured with a type K thermocouple.

Fluctuations were less than 1°C, and the error in the calibration was less than ~ 3°C. During measurements, the pressure in the beam was better than 5 x 10^{-9} Torr.

The S parameter was measured as function of the temperature at three incident energies, as displayed in fig 5.2. The three curves correspond to positrons implanted close to the surface $\bar{z} < 20$ Å (E = 25 eV), in the bulk $\bar{z} \approx 8200$ Å (E = 20 keV), and at an intermediate point where there are contributions from the surface and the bulk, $\bar{z} \approx 130$ Å (E = 1.5 keV).

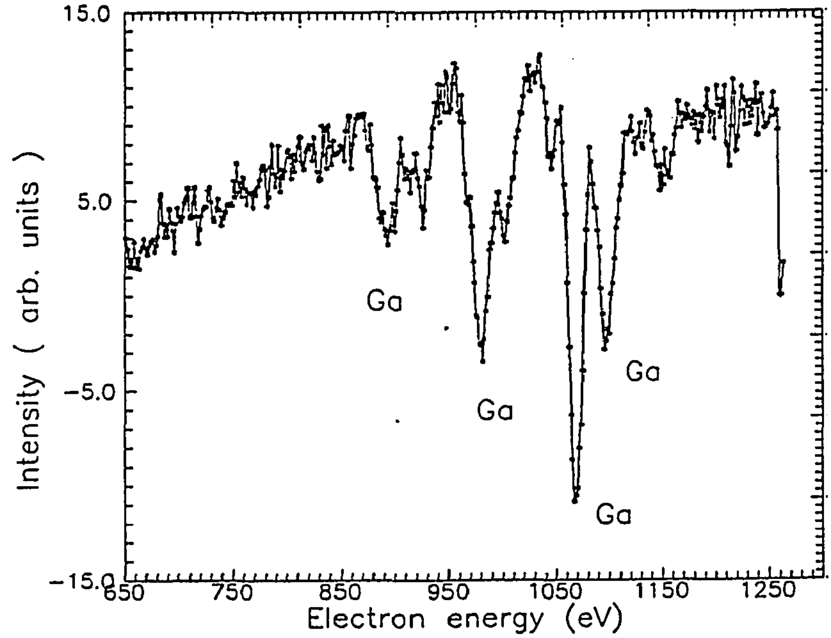

Figure 5.1: Auger spectrum of Ga, taken before the experiments.

The mean implantation depth was calculated using Eq. (2.2). Different features were seen for the surface and bulk. The S parameter at the surface (E = 25 eV) does not show a significant change at the melting temperature suggesting that the branching ratio of positrons forming Ps, or annihilating at the surface, is not altered on melting, *i.e.* is independent of the crystalline structure. The small rise observed at the melting point could be associated with changes in the geometry of the sample, or melting of a section of the sample caused by variations in temperature across the sample. It is interesting to note that the density of electron states increases significantly[111] near the Fermi energy when Ga melts suggesting that there are more energetic electrons available to pick up the positron and form positronium; an increase in positronium formation should be seen on melting, however this did not occur.

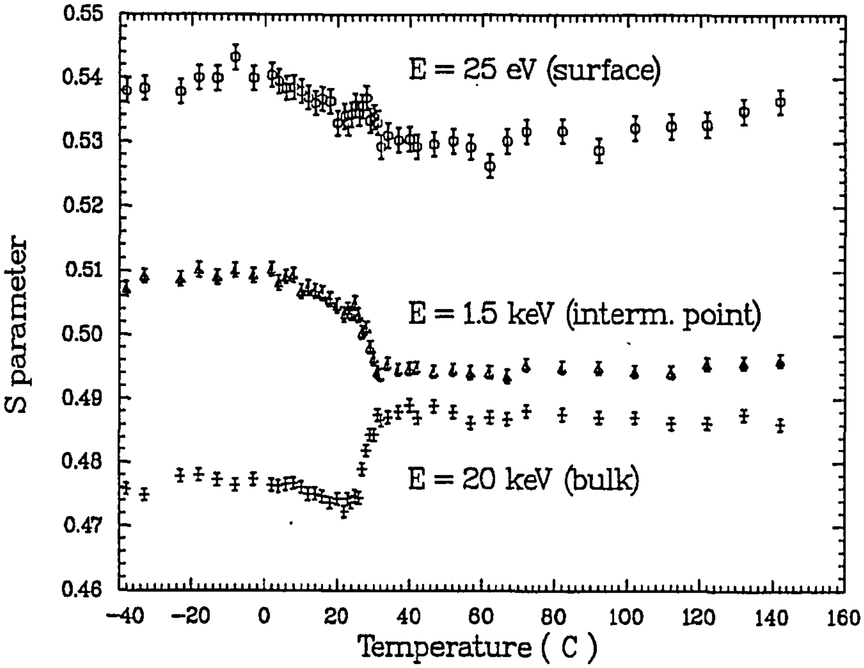

Figure 5.2: S parameter in Ga for three incident energies as function of temperature. E = 25 eV corresponds to positrons implanted close to the surface ($\bar{z} < 50$ Å), E = 20 keV are positrons implanted in the bulk ($\bar{z} \approx 8000$ Å), and E = 1.5 keV positrons implanted at $\bar{z} \approx 130$ Å, this curve has contributions from positrons annihilating in the bulk and surface.

As the temperature increases beyond the melting point, the surface value of S in Ga increases mainly from thermally activated formation and desorption of Ps from the surface. Positronium fraction curves are shown in figure 5.3 for the same incident energies. The first curve, (E = 25 eV), shows that positronium begins to be thermally desorbed at T ≈ 50 °C. The S parameter from annihilation of Ps is high because the low momentum of the e^+-e^- atom.

Thermal desorption of Ps has not been observed before in liquids, and, this work shows for the first time, that a positron surface state can exist on disordered surfaces. At the melting point , a small rise is observed; as before, this rise could reflect local melting, or impurities being released from the surface.

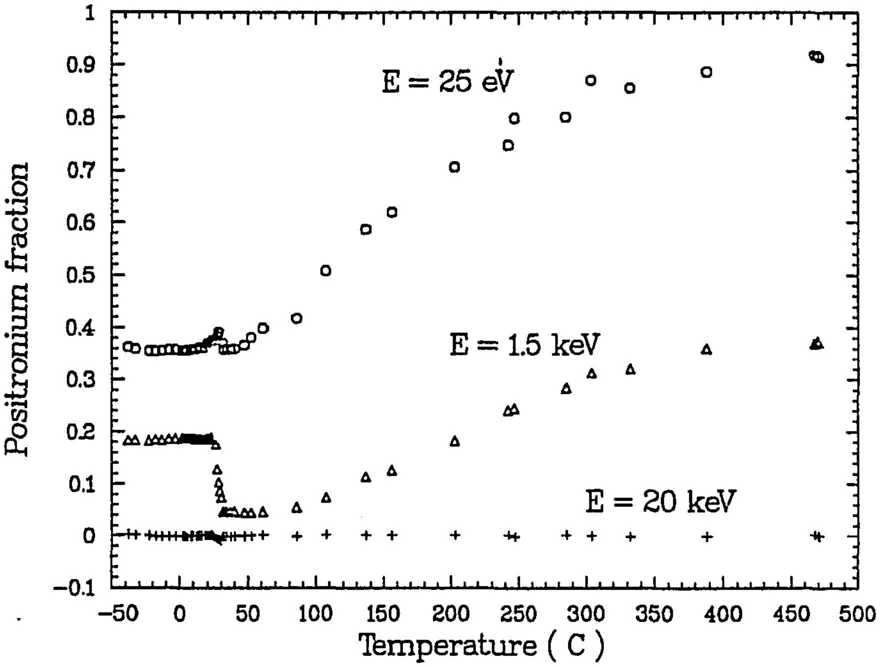

Figure 5.3: Positronium fraction in Ga as function of temperature. The first curve is for $\bar{z} < 50$ Å, the second curve is for $\bar{z} \approx 130$Å, and the lower curve is for $\bar{z} \approx 6200$ Å.

We turn now to a quantitative treatment of positronium desorption. The activation energy of positronium E_a is related to the binding energy of positrons to the surface trap E_b, the energy necessary to extract an electron from the surface ϕ_-, and the energy released when Ps is created in vacuum (6.8 eV). From the Born-Haber cycle[112]:

$$E_a = \phi_- + E_b - 6.8\ eV. \tag{5.1}$$

Typical values of E_b are 2-3 eV. The activation energy for desorption of positronium ϕ_{Ps}, can be calculated from the temperature dependence of the fraction of positrons arriving at the surface that form Ps[113,142]:

$$f_0(T) = F_0 + \frac{\Gamma \exp\left(-E_a/k_B T\right)}{\lambda + \Gamma \exp\left(-E_a/k_B T\right)} f_s, \tag{5.2}$$

where F_0 is the fraction of energetic positronium emitted from the surface. It is generally assumed that the desorption rate[113,143] is $\Gamma \exp(-E_a/k_BT)$, where λ is the annihilation rate of positrons trapped at the surface state. The second term in eq. (5.2) is the fraction of positroniums emitted from the surface state, with f_s the fraction trapped at the surface. The experimental values of the Ps fraction in fig. 5.3 were fitted with a nonlinear fitting routine, using F_o, f_s, E_a, and Γ/λ as free parameters. The results are shown in fig. 5.4. The solid line is a fit to equation (5.2). The results are $E_a = 0.35(0.03)$ eV, $F_o = 0.36(0.01)$, $f_s = 0.55(0.01)$ and $\Gamma/\lambda = 1.0(0.4) \times 10^4$.

The electron work function in metals depends on the phase of the surface; the differences between phases is about 5 %. However, the differences between the results obtained by different experimental methods are of the same order[116]. Therefore, the work function used to calculate the binding energy of positrons to the surface represents an average from different phases. From Ashcroft and Mermin[116]'s book, the electron work function in Ga is $\phi_- = 3.96$ eV. From eq. (5.1) we obtain for the positron binding energy $E_b = 3.19(0.03)$ eV. This value is higher than the theoretical value $E_b = 2.3$ eV, obtained by Nieminen and Hodges[114]. However, these authors used an average electron density to determine the correlation energy E_{corr}. It was shown later[115] that this method gives variations in the absolute values of the positron work function of up to 1 eV.

The second curve in fig. 5.2 shows the S parameter for positrons implanted at $\bar{z} \approx 130$ Å. This curve has contributions from positrons that annihilate in the surface and in the bulk. In liquid Ga, the fraction annihilating in each state is different from that in the solid state. Therefore the S parameter drops upon melting because fewer positrons can reach the surface. This finding indicates that the diffusion length decreases on melting.

The bulk value of S for Ga in fig 5.2 ($E_{inc.} = 20$ keV) increases at the melting point, which is generally assumed to be caused by positron trapping[16,104,105]. An increase in the bulk lifetime of Ga from 190 to 260 ps[16], also suggests that positrons become trapped in liquid Ga. We note that these traps do not affect the positrons annihilating at the surface, because no change is seen in S_s. The potential well of the traps at the surface is negligible compared to the surface state.

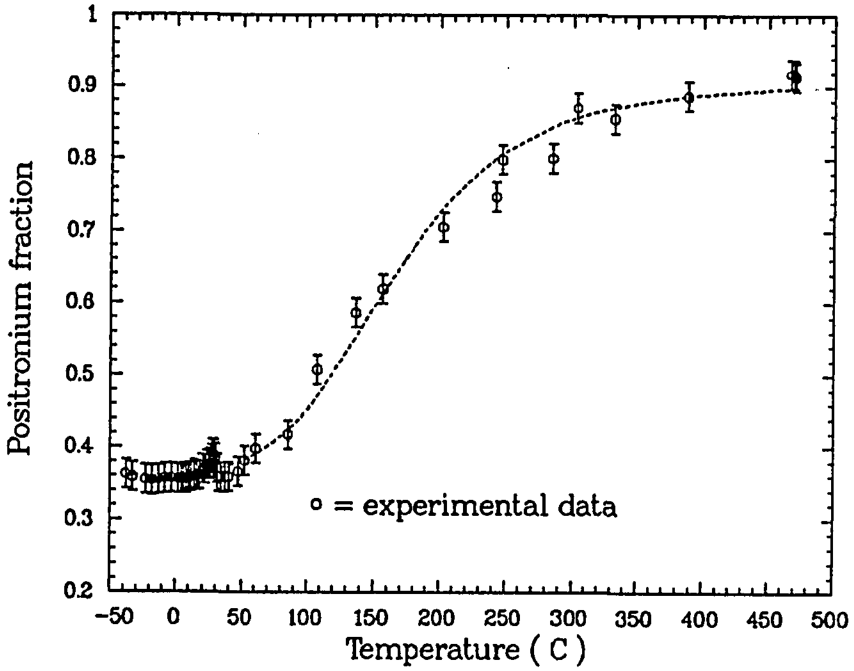

Figure 5.4: Thermally activated Ps formation in Ga; the dashed line is a nonlinear fit using eq. 5.2. The results are $E_a = 0.35(0.03)$ eV, $F_0 = 0.36(0.01)$, $f_s = 0.55(0.01)$ and $\Gamma/\lambda = 1.0(0.4) \times 10^4$

In the solid phase, there was no trapping of positrons in thermal vacancies[104,105] The reason may be that Ga has a very open packed structure, orthorhombic Ga has a coordination number[111] $N_c = 7$. Therefore because the large separation between atoms, potential wells capable of trapping positrons are not created[107] or they are too shallow. On melting, Ga contracts by 3.1 %, and the coordination number increases to N_c = 9-10.[111] In spite of the decrease in the average interatomic spacing, previous studies have shown that trapping does occur in the melt[16]. Kishimoto and Tanigawa's[109] two-parameter correlation of the lifetime of positrons and energy of the annihilation radiation suggests that more than one annihilation mode can coexist in the melt. One mode is short lived, with narrow momentum distribution, which is attributed to trapping and annihilation in solid-like clusters in the liquid. The other is long lived, with broad momentum distribution[109] (attributed to trapping in vacancy-like defects).

These two modes of annihilation were also evidenced by a small decrease in the lifetime of liquid Ga as the temperature was increased[16]. Our results only show a small decrease in S_{bulk} as the temperature is increased.

Bismuth

Bi is a semi-metal with low melting point, $T_m = 273.3$ °C, that also contracts on melting (3.3 %). Its vapor pressure just above the melting point is $\approx 1 \times 10^{-10}$ Torr; its density at room temperature is 9.8 g/cm^3. As in Ga, previous studies in Bi[105] showed no trapping of positrons in thermally generated vacancies in the solid phase. Therefore, in solid Bi the bulk S parameter increases slightly, following the thermal expansion of the lattice[105] (which is also true for Ga).

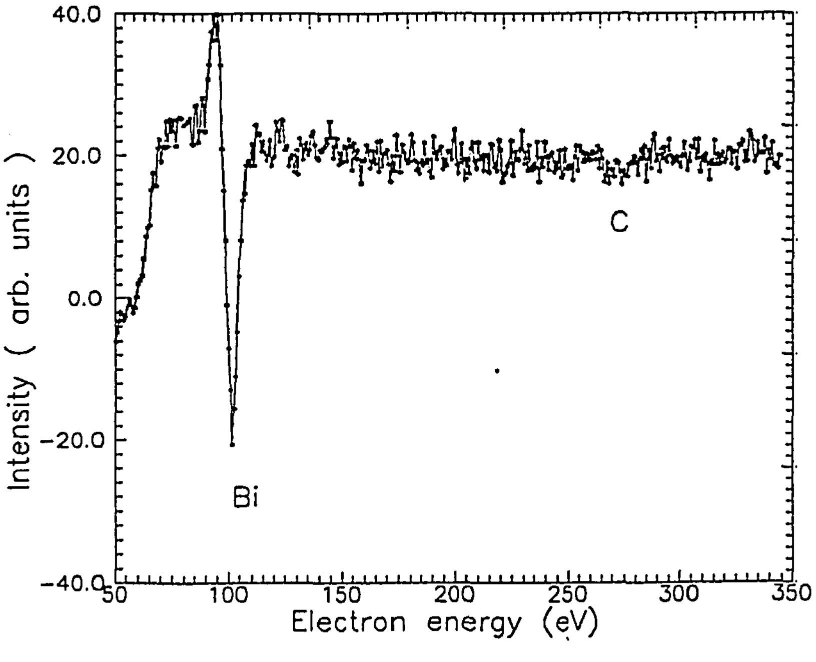

Figure 5.5: Auger spectrum of a clean Bi surface taken before the experiments.

The Bi sample was obtained from Aesar/Johnson Mathey, MA, 99.9999 %

purity. Before placing the sample the vacuum, it was etched in a solution of 160 ml H_2O, 30 ml nitric acid, and 40 ml glacial acetic acid[144]. It then was placed in the beam, sputtered, and annealed *in situ* until there was no trace of contaminants. The Auger spectrum of a clean surface taken before the experiments is shown in figure 5.5.

The experimental values of the S parameter as a function of temperature are shown in fig. 5.6. The S parameter at low incident energy, E = 200 eV, corresponds to positions implanted close to the surface ($\bar{z} < 50$ Å). This curve starts to increase at T ~ 80°C and levels off at the melting point. As in liquid Ga, this leveling is caused by thermal desorption of positronium.

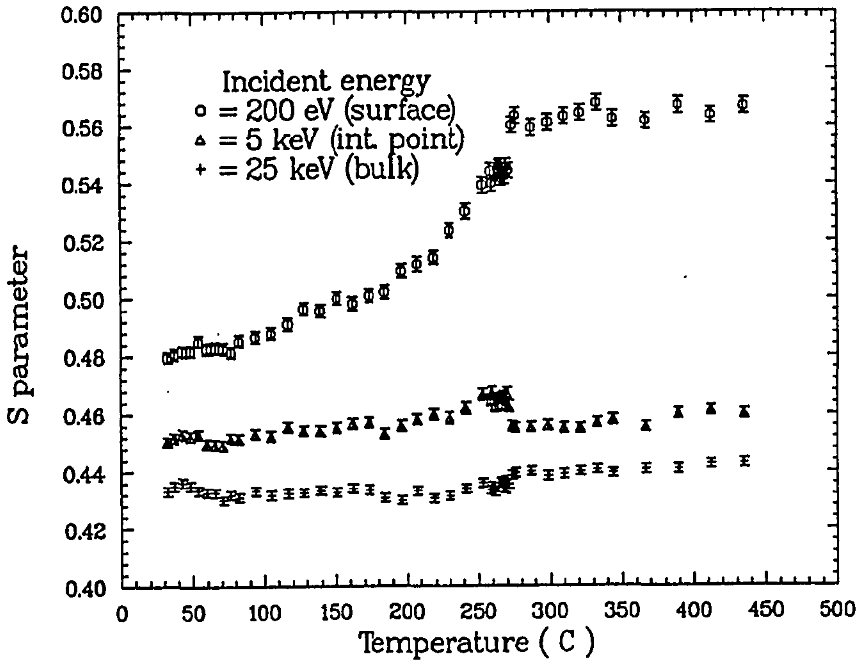

Figure 5.6: S parameter for Bi plotted as function of temperature for three incident energies. E = 200 eV corresponds to positrons implanted at $\bar{z} < 50$ Å, E = 5 keV to positrons implanted at $\bar{z} \approx 480$ Å, and E = 25 keV corresponds to $\bar{z} \approx 6200$ Å.

At the melting point, there is a jump associated with a change in the geometry of the sample, or release of impurities. It does not seem to be related to a change in the surface state, because the positronium fraction increases slightly. and the change in S is of the same order of magnitude as the error bars.

The second curve in fig. 5.6 shows the S parameter from positrons implanted at E = 5.0 keV, which corresponds to $\bar{z} \approx 540$ Å. As in Ga, there are two contributions to this curve; S_s and S_{bulk}. A fraction of the positrons diffuse to the surface and contribute with a high value of S; the remaining annihilate in the bulk. Because the diffusion length changes at the melting point, the fraction of positrons that annihilates in the bulk increases, and the the fraction in the surface decreases. As a result the S parameter decreases.

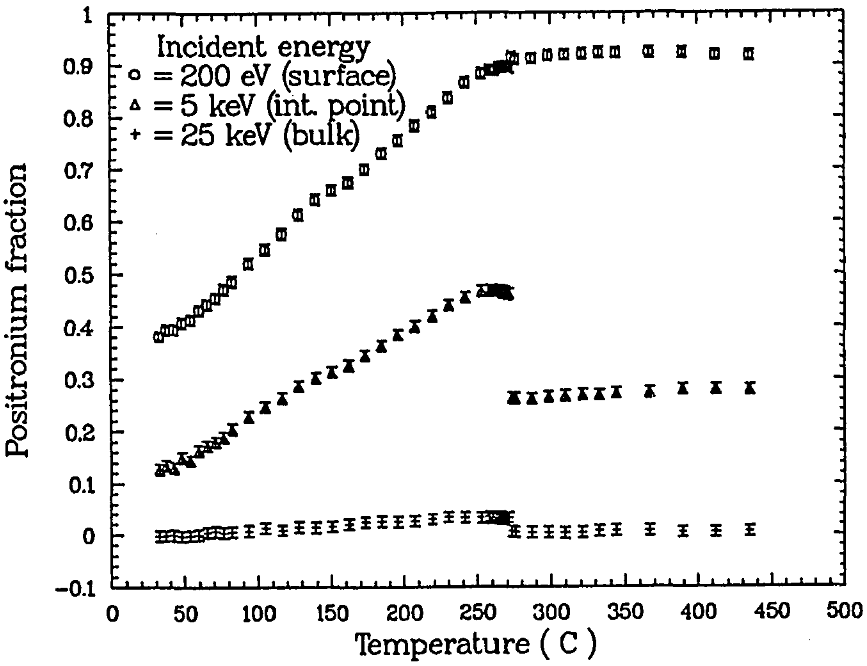

Figure 5.7: Positronium fraction in Bi at the same incident energies as in fig. 5.6, as function of temperature.

The fraction of incident positrons that form Ps after returning to the surface is shown in fig. 5.7 for the same incident energies as fig. 5.6. Thermally activated Ps formation is clearly seen in the first curve (E = 200 eV). These positrons are implanted close to the surface, and most of them return to it. The small increase in Ps formation upon melting suggests that the density of electron states increases in the liquid phase, *i.e.* there are more free electrons with energies close to the Fermi energy that can combine with positrons to form Ps.

Using eq. (5.2), the first curve in fig 5.7 can be fitted, to obtain the formation energy of positronium. The results obtained are $E_a = 0.32(0.01)$ eV, $F_o = 0.38(0.01)$, $f_s = 0.58(0.01)$, and $\Gamma/\lambda = 7(2) \times 10^3$. The results are also shown in fig. 5.8, along with the fitted results. The electron work function[116] of Bi is $\phi_- = 5.4$ eV. Using equation (5.1) the binding energy of positrons to the surface trap $E_b = 2.72(0.01)$ eV. At the melting point, the S parameter drops because fewer positrons can return to the surface, indicating that the diffusion length decreases on melting.

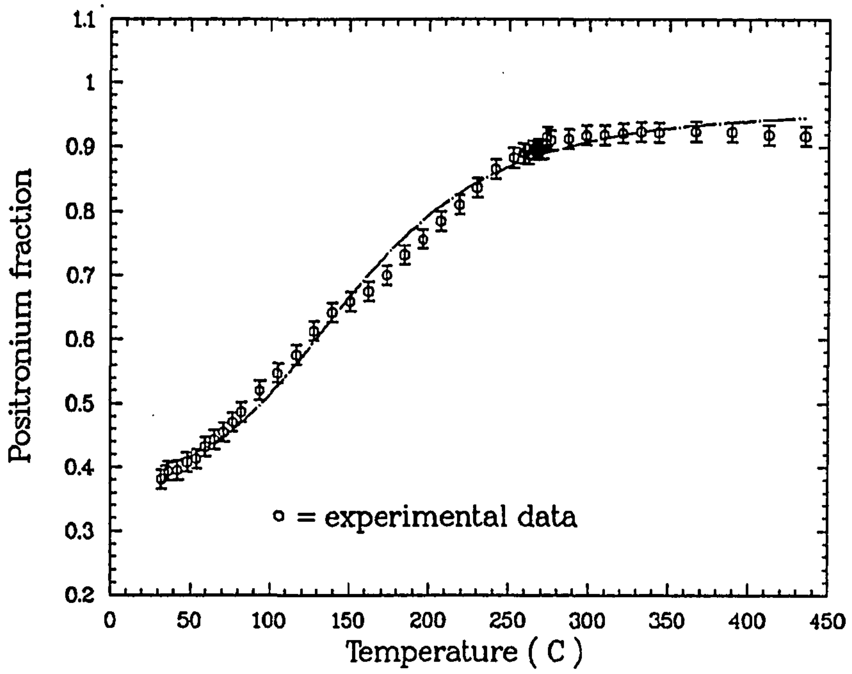

Figure 5.8: Fit to positronium fraction in Bi (dotted-dashed line) using eq. 5.2. The circles are the experimental values. The formation energy of positronium is $E_a = 0.32(0.01)$ eV, $F_o = 0.38(0.01)$, $f_s = 0.58(0.01)$, and $\Gamma/\lambda = 7(2) \times 10^3$.

The bulk value of S for Bi, E = 25 keV, which corresponds to an implantation length of $\bar{z} \approx 7040$ Å, shows a linear increase with temperature, and a small change upon melting. This jump could be due to vacancy trapping[117] or to a change in the electronic configuration[118] in the location of positron annihilation.

The change in positronium fraction at the melting point seen in the third curve of fig. 5.7 (E = 25 keV) reflects ~ 3 % of the positrons reaching, and annihilating at, the surface. Upon melting, all positrons annihilate in the bulk of the sample.

Sodium

Na is an alkali metal with low melting point, 95.7 °C, its vapor pressure at $T = 130$ °C is $\approx 4 \times 10^{-8}$ Torr. The vapor pressure increases very rapidly as temperature increases. Therefore, only measurements for $T < 250$ °C could be performed. Sodium reacts easily with oxygen and hydrogen, and is very hard to keep clean, even at a pressure of 2×10^{-9} Torr, which corresponds to normal running conditions. To obtain a clean sample, a sealed ampule from Aesar/Johnson Mathey, MA, 99.95 % purity, containing Na was inserted into the vacuum system. When the pressure reached $\approx 1 \times 10^{-9}$ Torr, the tip of the ampule was broken and heated until liquid Na poured into the sample holder. A large, clean Na meniscus was obtained. The surface was subsequently cleaned by skimming with a flat stainless steel blade to remove impurities. Auger spectra were taken before and after measurements to assure that the surface of the sample was free from impurities. Figure 5.9 shows a typical Auger spectrum after cleaning.

Previous theoretical studies[31,115] predicted a high value of the positron work function for Na ($\phi_+ \approx 5$ eV), and a positive value of the positronium work function ($\phi_{Ps} \approx 0.4$ eV). Therefore, no emission of positrons or positronium from the surface was expected. In addition, it was also predicted that there would be no bound states at the surface[31]. As a consequence, all thermal positrons reaching the surface from the inside will be reflected and eventually annihilate in the bulk.

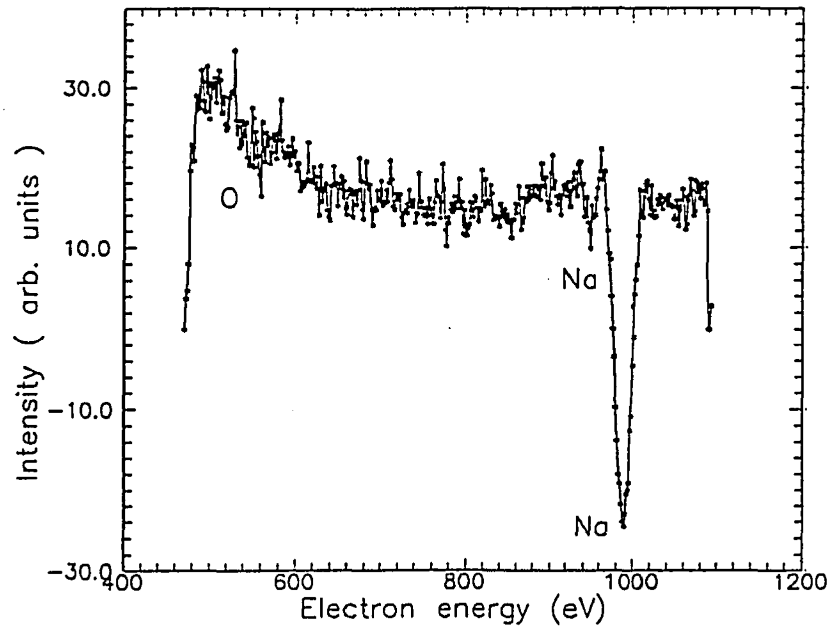

Figure 5.9: Typical Auger spectrum of clean Na sample taken before the experiments.

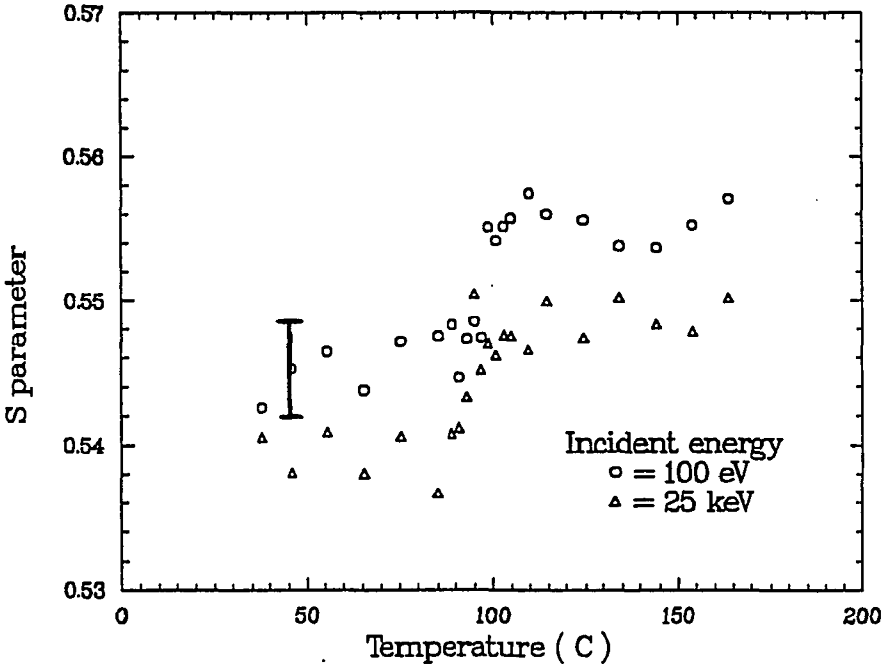

Figure 5.10: S parameter in Na for positrons implanted close to the surface (E = 100 eV) and deep in the bulk (E = 25 keV) as function of temperature. Both curves show similar features and are close to each other, indicating that, in both cases, positrons annihilate in the bulk.

This effect can be seen in figure 5.10, where the S parameter is shown for for two incident energies. The results at E = 100 eV ($\bar{z} < 50$ Å) and E = 25 keV ($\bar{z} = 7.1\ \mu$

m) are similar because even positrons implanted close to the surface annihilate in the bulk. The difference between the two curves is associated with the emission of nonthermal positronium.

The curve for positrons implanted at 25 keV increases at the melting point, reflecting a change of state from free to trapped in the liquid phase. The same effects were observed for Ga, and Bi. Trapping in liquid Na was also observed with lifetime experiments[16], in which the lifetime increased from ≈ 263 to ≈ 278 ps upon melting.

In figure 5.11, the positronium fraction is plotted as a function of temperature. At low incident energies, a small fraction is desorbed from the surface, which we believe is due to nonthermal positrons. The decrease upon melting may be due to a decrease in the density of electron states at the Fermi energy, which reduces the probability of picking an electron to form Ps.

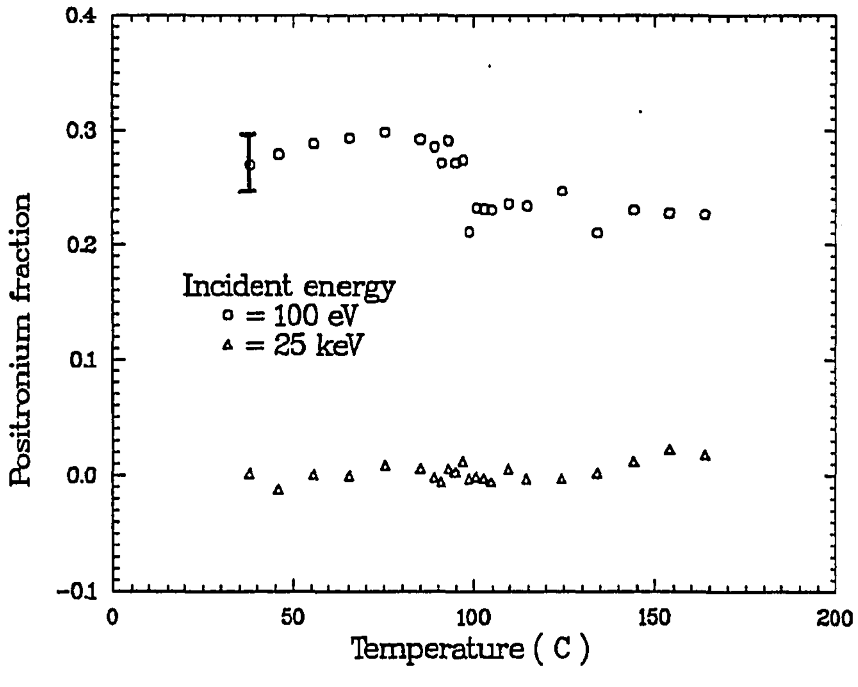

Figure 5.11: Positronium fraction as function of temperature for the same incident energies as in Fig. 5.10.

Tin

Tin (Sn) is also a metal with low melting point: 232.0 °C. Its density is $\rho = 7.3$ g/cm^3 and its vapor pressure at T = 900 °C is $\approx 1 \times 10^{-6}$ Torr. Therefore it is suitable for study with the Liquid Metals Beam. The response of tin to positrons is very similar to Ga. Previous studies[18,119] have shown no vacancy trapping in the solid phase, even at temperatures close to the melting point.

Before insertion into the vacuum, a polycrystalline sample (99.9999 % purity) from Aesar/Johnson Matthey was etched[144] in a hot solution (T = 80 °C) of 60 % ethanol and 40 % HCl, until the surface was shiny. In vacuum, the sample was sputtered and annealed to 400 °C for several hours. An Auger spectrum is shown in figure 5.12. A small amount of oxygen is present at the surface.

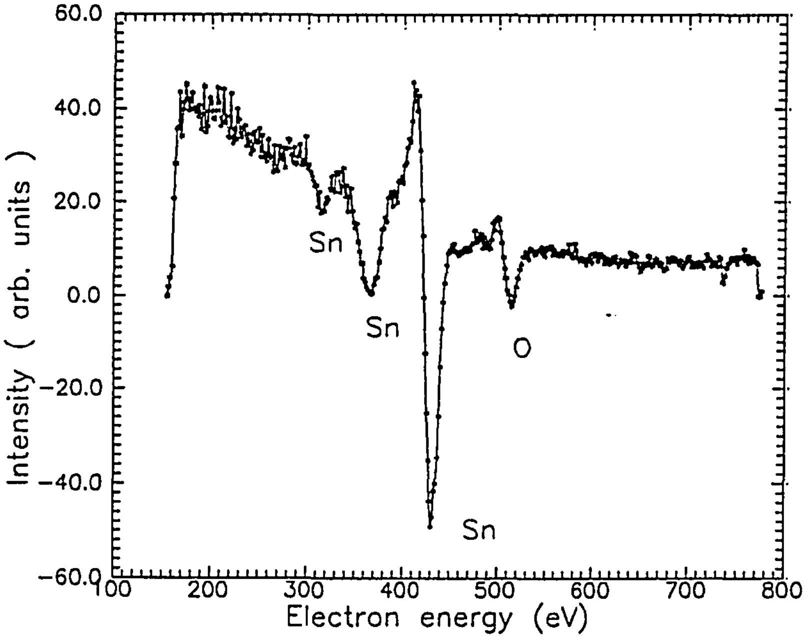

Figure 5.12: Auger spectrum of Tin taken before the experiments.

The S parameter measured as a function of temperature for three incident energies is shown in figure 5.13. As with Ga and Bi, we can calculate an approximate implantation depth using eq. (2.2). The curve at E = 100 eV corresponds to positrons implanted less than 50 Å from the surface. E = 3 keV corresponds to positrons implanted at $\bar{z} \approx 320$ Å, and E = 25 keV are positrons implanted at

$\bar{z} \approx 9450$ Å.

At high incident energies, most positrons annihilate in the bulk. S_{bulk} does not change appreciably when the temperature increases in the solid phase, which indicates that there is no trapping[18] in thermally generated vacancies. Seeger[107] argues that Sn is a metal with narrow ion cores, which preclude vacancy trapping because the potential well formed at a vacancy is too shallow to trap positrons. The radius of Sn^{4+} is 0.71 Å, which is small compared with the interatomic distances (2.8 Å and 3.02 Å). At the melting point, there is an increase in S_{bulk}, which is an indication of trapping. The lifetime[18,102] in solid Sn was $\tau \approx 202$ ps, and no trapping was observed at thermally generated vacancies. Dedoussis *et al*[120] found later a small increase in the lifetime before melting, which they attribute to trapping by thermally generated vacancies. Our results do not show an increase in the S parameter below the melting temperature.

Upon melting there is ≈ 2% increase in S_{bulk}, which suggests that the electron density at the site of annihilation changes upon melting. As in Ga, the increase is attributed to positron trapping at vacancies. Early angular correlation[18,119] studies indicated that there was vacancy trapping in liquid Sn. We found no experimental values for the lifetime in liquid Sn in the published literature.

The curve at $E = 3$ keV, in figure 5.13, shows contributions to the S parameter from the surface and the bulk. At the melting point, fewer positrons reach the surface because the diffusion length is shorter than in the solid phase, and the S parameter decreases.

The value of S at the surface in fig. 5.13 ($E = 100$ eV) does not show a significant change at the melting point (the small jump results from changes in the surface geometry). Therefore, the branching ratio of positrons annihilating in the surface or as positronium does not change. A similar situation was seen in Ga and Bi.

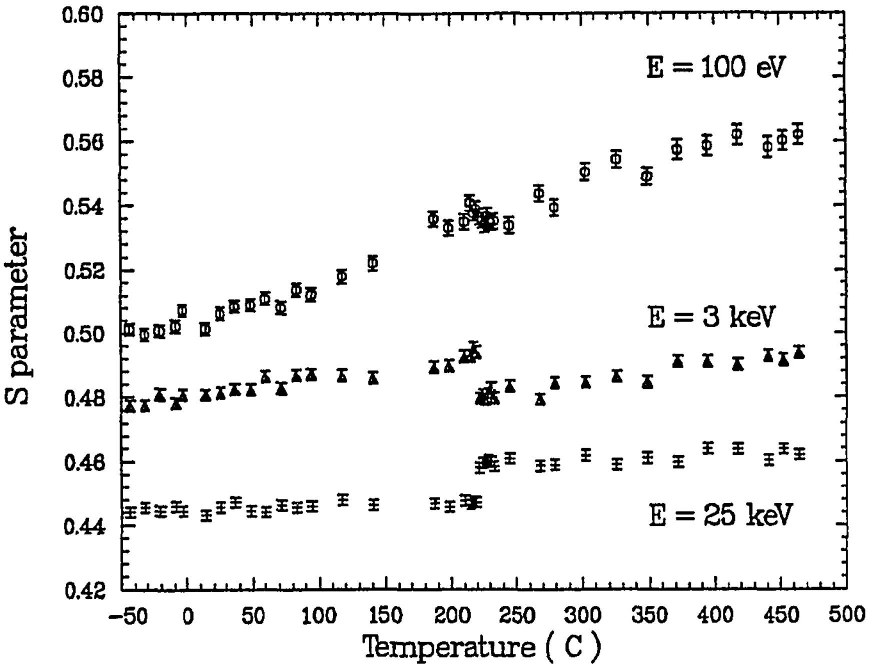

Figure 5.13: S parameter for solid and liquid Sn as function of temperature at three incident energies. E = 100 eV corresponds to positrons implanted at $\bar{z} < 50$ Å, E = 3 keV corresponds to $\bar{z} \approx 320$ Å, and E = 25 keV corresponds to $\bar{z} \approx 9450$ Å.

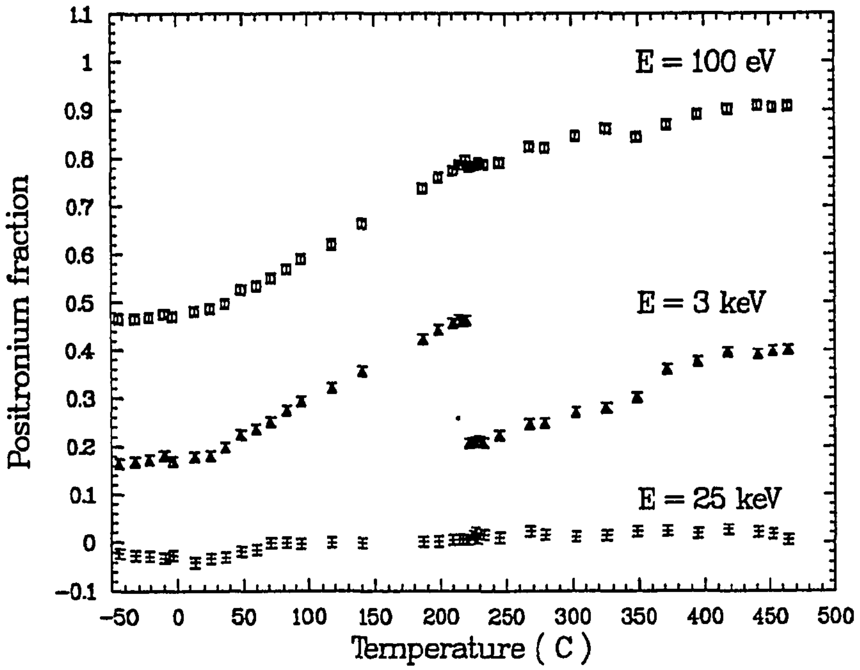

Figure 5.14: Positronium fraction for Sn, for the same incident energies as in figure 5.13.

There is a continuous increase in S_s with temperature that is associated with thermal positronium desorption. In figure 5.14, the positronium fraction as function of temperature is shown for the same incident energies as fig. 5.13.

Near the melting point, positrons implanted close to the surface (E = 100 eV) fall into the surface trap and most are thermally desorbed as positronium. Hence, there is only a small change in positronium formation upon melting. It is interesting to note that desorption continues in the liquid as well.

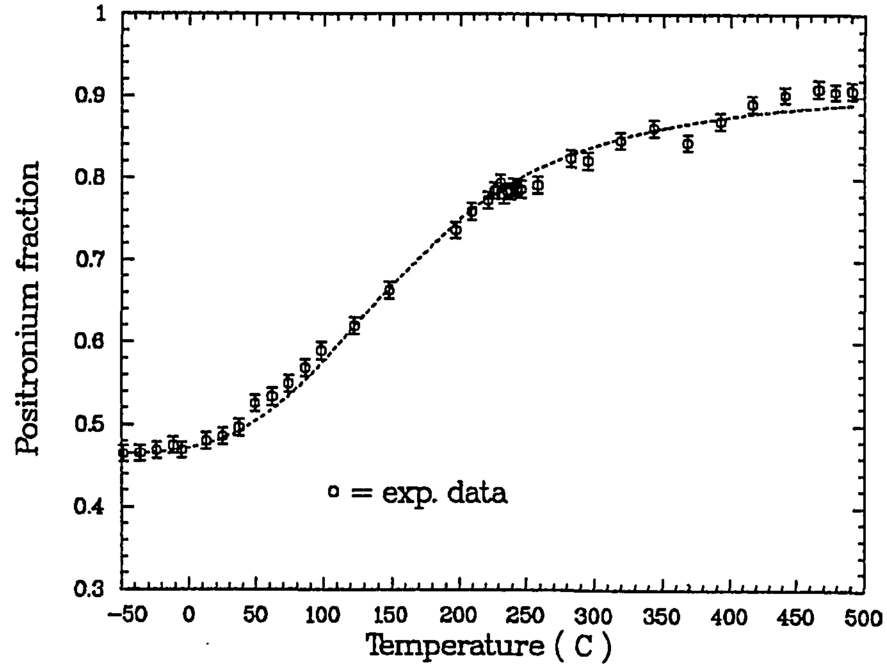

Figure 5.15: Fitted values of positronium fraction to equation 5.2, versus temperature. The circles are the experimental data. The results are $E_a = 0.25(0.01)$ eV, $F_0 = 0.46(0.03)$, $f_s = 0.45(0.03)$ and $\Gamma/\lambda = 0.8(0.1) \times 10^3$

The positronium fraction curve at E = 100 eV can be fitted with equation (5.2). The resulting values are $E_a = 0.25(0.01)$ eV, $F_o = 0.46(0.03)$, $f_s = 0.45(0.03)$, and $\Gamma/\lambda = 8(1) \times 10^3$. Fig 5.15 shows the fit , along with the experimental results. Using equation (5.1), and the value of the electron work function[116] for Sn $\phi_- = 4.4$ eV, the positron binding energy is $E_b = 2.65(0.01)$ eV, which is very close to the theoretical value of $E_b = 2.5$ eV[114]. As mentioned before, the variation in the electron work function for different crystallographic faces is about 5 %, as is the difference between different experimental methods.[116] Thus, it is not necessary to differentiate between different faces.

Lynn *et al*[121] found the activation energy of Ps in Sn to be $E_a = 0.38(0.02)$ eV, which is 50 % higher than our values. However, all their measurements were done below the melting point, and our results show that Ps desorption continues in the liquid phase. This difference could introduce an error in their calibration of Ps fraction at low incident energies (R_1), giving an incorrect value in their fits of the activation energy of Ps. The difference in E_a also can results from its dependence on the crystallographic face. Lynn *et al*[121] used crystalline Sn(110), while our measurements were made with polycrystalline Sn. Differences of 25 % have been observed for E_a in different faces of Ag.[8]

5.1.2 Measurements of S and F parameter for Pb and In as function of temperature

Lead

Lead has a low melting point $T_m = 327.5$ °C, and its vapor pressure at the melting point is $\approx 6.5 \times 10^{-9}$ Torr. Its density is 11.4 g/cm^3 at room temperature and it expands 3.5% upon melting.

Pb has been studied with angular correlation techniques[19,122], lifetime[108], and positronium time-of-flight[123]. Lifetime[108] studies showed trapping of positrons in thermally generated vacancies, starting from T $\approx$ 150°C and reaching saturation close to the melting point. Angular correlation studies[19] in bulk Pb showed similar behavior. Upon melting, an increase in the coincidence count rate at the peak of the angular correlation curve (this is equivalent to the S parameter), shows that the traps change. It is not clear if this change is related to an expansion of the size of the trap, or the appearance of a new kind of trap.

A polycrystalline sample of 99.9995 % purity from Aesar/Johnson Matthey was etched in a solution of 25% hydrogen peroxide, 75% acetic acid until a shiny surface was obtained[144]. In vacuum, the sample was sputtered with Ar, and annealed at 400 °C for several hours. The surface was monitored with Auger spectroscopy after cleaning. The spectrum of a clean sample is shown in figure 5.16.

Figure 5.17. shows the S parameter as function of temperature in Pb. As in the other metals discussed, the three curves correspond to positrons implanted at $\bar{z} < 50$ Å (E = 200 eV), at $\bar{z} \approx 460$ Å (E = 5 keV), and at $\bar{z} \approx 6050$ Å (E = 25 keV). A small increase is seen in the top curve (surface), which is probably due to thermal desorption of the small fraction of positrons that are trapped at the surface. Time-of-flight experiments[123] have shown that the positronium work function is negative. This conclusion is confirmed by our Ps fraction measurements (figure 5.18). The curve at E = 200 eV shows a high fraction of Ps at all temperatures, with a small increase from 50 °C to 300 °C.

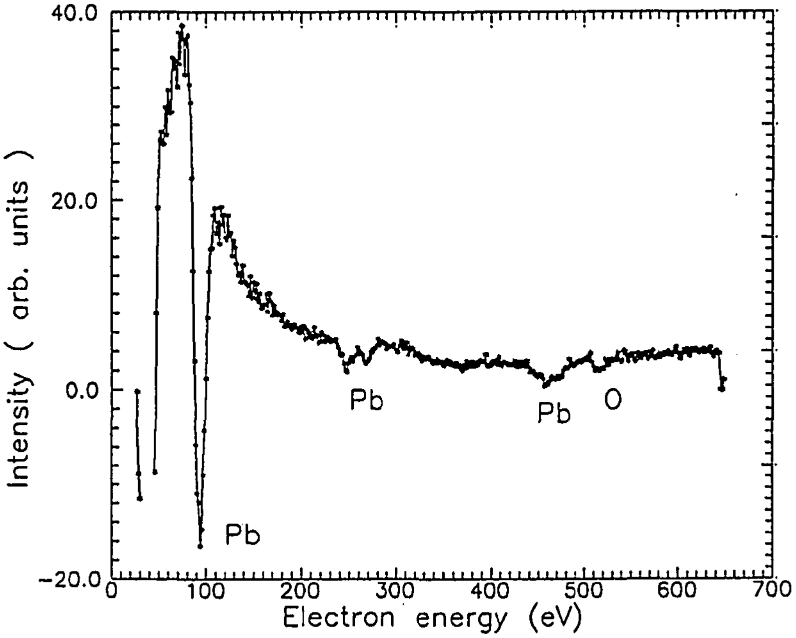

Figure 5.16: Auger analysis spectrum of a clean Pb sample.

The third curve in figure 5.17 (E = 25 keV) corresponds to positrons annihilating in the bulk. There is a small increase starting at T ≈ 150°C, reflecting the onset of trapping in thermally generated vacancies. At low temperatures, the diffusion length seems to be long, and positrons implanted at 25 keV can still reach the surface. Therefore, this curve has a small contribution from positrons annihilating at the surface that increases the value of S at low temperatures. This effect can be more clearly seen in figure 5.18. At E = 25 keV, below the melting point, there is a small fraction of positronium. Upon melting, all positrons annihilate in the bulk. Trifthäuser's results[19] show an appreciable increase in the angular correlation curve at the melting point (see figure 1.3) which we can not observe with the S parameter.

There is no appreciable change in the bulk S parameter (E = 25 keV) at the melting point, this is probably due to poor statistics, and the previously mentioned contribution from annihilation at the surface.

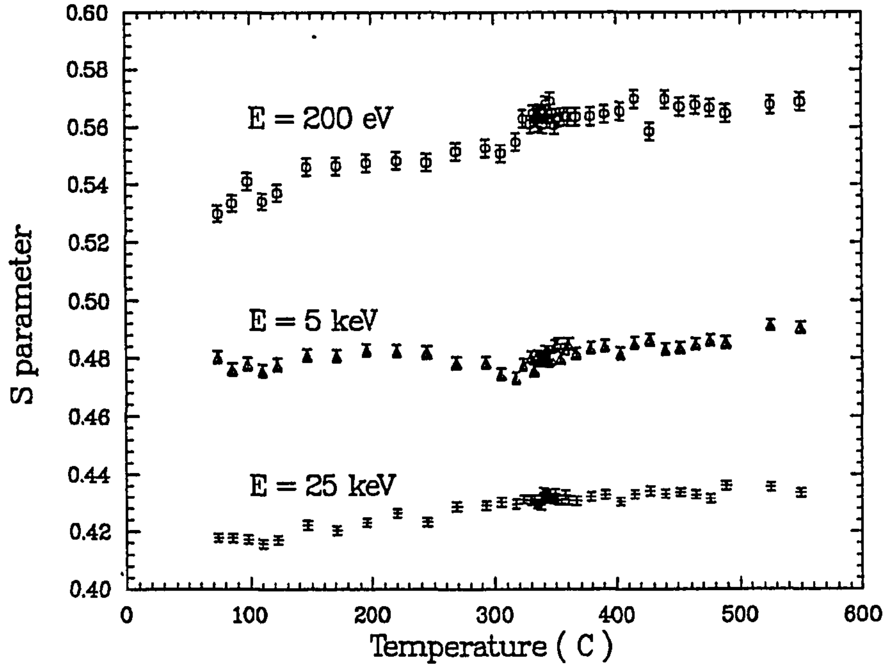

Figure 5.17: Experimental S parameter data for Pb plotted against temperature. The first curve, (E = 200 eV) corresponds to $\bar{z} < 50$Å, the second curve, (E = 5 keV) corresponds to $\bar{z} \approx 460$ Å, and the third curve, (E = 25 keV) is for $\bar{z} \approx 6050$Å.

The S parameter curve at the surface (E = 200 eV) in figure 5.17, shows a small jump at the melting point which is probably caused by a change in the geometry of the sample. This increase is only is slightly larger than the experimnetal error.

The results with E = 5 keV show that the fraction annihilating in the bulk, and the fraction annihilating at the surface are unchanged upon melting. This finding is an indication that the diffusion length is similar below and above the melting point. If our conclusion that all positrons are trapped at temperatures below the melting point is correct, then it is reasonable to believe that the diffusion length does not change on melting.

The formation energy of positronium E_a and the binding energy of positrons to the surface potential E_b cannot be calculated because only a very small percentage of positronium is thermally desorbed, which does not allow us to perform the fitting.

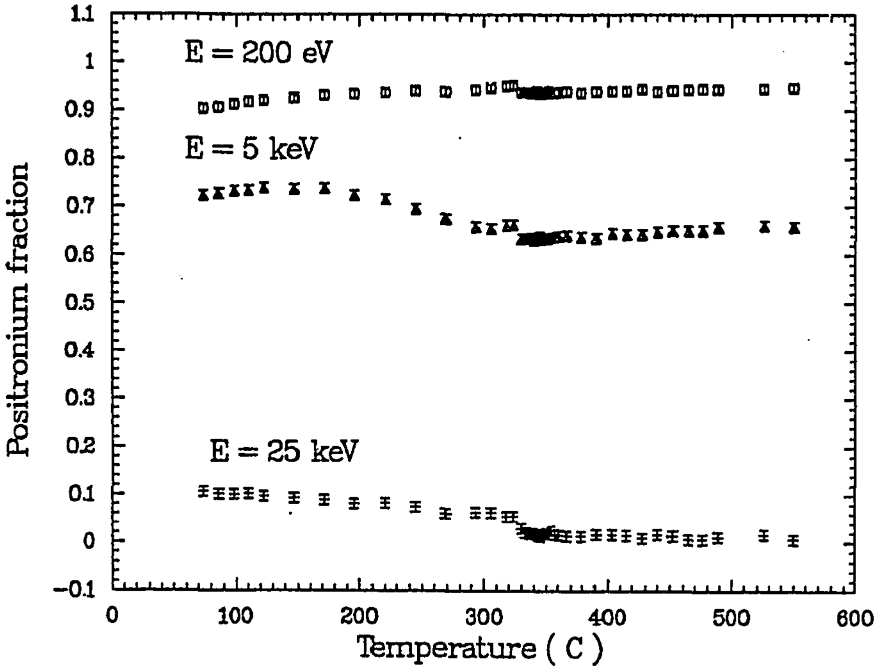

Figure 5.18: Experimental values of the positronium fraction for Pb, for the same incident energies as figure 5.17.

Indium

Indium has a low melting point, $T_m = 156.6$ °, and a vapor pressure at temperatures close to the melting point of 1×10^{-12} Torr. Thus In can be studied over a wide range of temperatures under ultra high vacuum. Its density is 7.31 g/cm^3. Upon melting, there is a volume increase of 2.7 %. Indium has been studied before with angular correlation[19,122] and lifetime techniques[109,17,9]. As with Pb, an increase in the lifetime indicates trapping in thermally generated vacancies. Upon melting, there is an increase in the coincidence count rate of the angular correlation curve[19] suggesting that there is a change in the size of the trapping centers, or the nature of the trapping centers, or there is an increase in the fraction of positrons trapped[19].

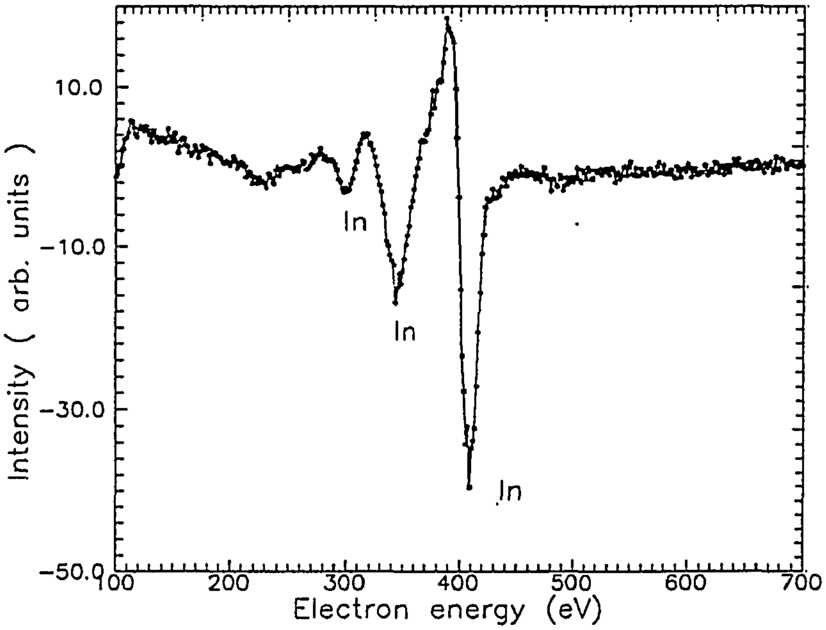

Figure 5.19: Auger spectra of In taken before the measurements.

Following the standard procedure, the In sample (purity 99.999 % from Aesar/Johnson Matthey) was etched in 75% HCl, 25% HNO_3 at 80 °C until a shiny surface was obtained[144]. It was subsequently placed in the sample holder, sputtered with Ar and annealed at 450 °C for a few hours. Figure 5.17 shows a clean

Auger spectrum. All measurements were taken at a pressure of 2×10^{-9} Torr. In figure 5.20, we show the experimentally measured S parameter. The top curve is for $\bar{z} < 50$ Å (E = 150 eV), the middle curve corresponds to positrons implanted with $\bar{z} \approx 240$Å (E = 2.5 keV), and the lower curve $\bar{z} \approx 9400$ Å (E = 25 keV). At E = 150 eV, the S parameter increases with temperature and is associated with thermal desorption of positronium, as seen in Ga, Bi, and Sn. Figure 5.21 shows the positronium fraction at the same incident energies as fig. 5.20. The top curve (E = 150 eV) shows that Ps starts to be thermally desorbed at T ≈ 20°C. As seen in the other metals, upon melting, the S parameter does not change appreciably (except for a jump due to change in the geometry of the sample, or release of impurities from the surface). The fact that the surface S parameter does not change upon melting shows that the branching ratio for positronium formation or annihilation at the surface is independent of the overall bulk structure.

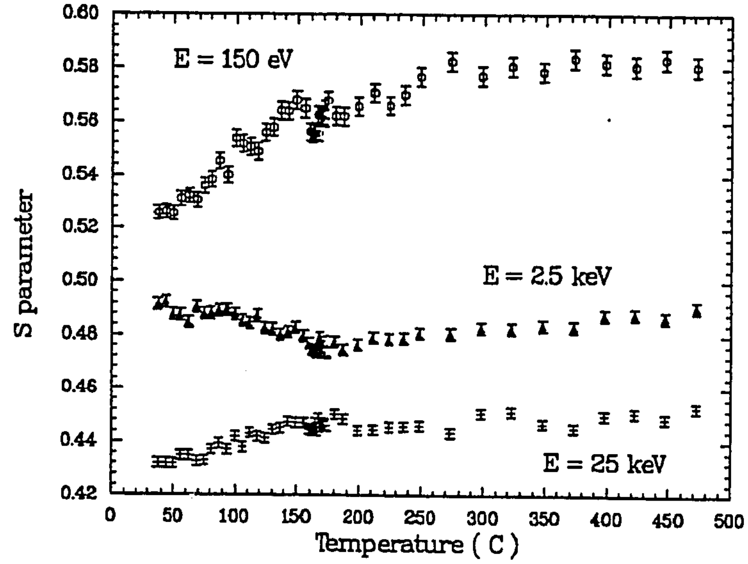

Figure 5.20: S parameter curves in solid and liquid In for three implantation depths. $\bar{z} < 50$ Å, $\bar{z} \approx 240$ Å, and $\bar{z} \approx 9400$ Å.

From the curve at E = 150 eV in figure 5.21, we can see that upon melting, the Ps fraction decreases slightly, which might imply that the density of vacancies at the surface increases, thus increasing the trapping rate. Upon melting, the density of electron states decreases slightly at the Fermi energy[111], and there are fewer electrons with energy close to the Fermi energy available to form Ps. This effect may also explain the decrease in Ps fraction, and might also show that the density of electron states decreases on melting.

The S parameter curve for E = 2.5 keV in figure 5.18 initially decreases with temperature, which indicates that the fraction of positrons that reach the surface decreases as the temperature is increased; this implies that the diffusion length decreases. This effect is very clearly seen in the measurements of Ps fraction in fig. 5.21, where the middle curve shows a rapid decrease in Ps.

At the melting point, there is a small or negligible change in S or F. This finding is in contrast to the metals that do not show trapping in the solid phase (Ga, Bi, Na, and Sn) and consequently, show a large jump in both S and F. If all positrons are trapped in defects, the change from solid to liquid does not change the state of the positron, and S or F do not change.

The S parameter curve at E = 25 keV in fig. 5.20 corresponds to positrons annihilating primarily in the bulk. As in Pb, Bi and Sn, a small fraction of these positrons reach the surface. There is also a small increase in S when the temperature increases. This effect, seen before with angular correlation techniques,[19,18] shows that positrons are trapped in thermally generated vacancies. An early study[9] of lifetime in solid In revealed an increase from ≈ 200 ps at T = 25 °C, to 250 ps at T = 150 °C (just below the melting point). Crisp *et al*[17] found the bulk lifetime in In was τ_b = 182 ps. Close to the melting point (T ≈ 150 °C), their results show a vacancy lifetime of τ_v = 240 ps. Work by Kishimoto and Tanigawa[109] also shows an increase in the lifetime as the temperature increases from 220 ps at T = 25 °C to 260 ps at T ≈ 130 °C . Very close to the melting point they observed an additional fast rise in the lifetime, which they attributed to formation of divacancies or to impurities in In. This newer value for the lifetime in In will be used to calculate the diffusion coefficient.

Although the lifetime results from different experiments do not agree well, they all show an increase that can be attributed to positron trapping in thermally generated vacancies. The change in angular correlation below T_m, and the small change upon melting also seem to indicate that positrons annihilate from trapping sites in the melt. The change upon melting is probably due to a variation in the kind of traps; single vacancies as well as vacancy clusters of various sizes can be expected in liquid In.[19]

The S parameter for E = 25 keV (figure 5.20) does not change at T_m. We cannot observe a difference between solid and liquid In because of the mixing of surface and bulk S parameters for measurements at high incident energy. Another problem is the large experimental error in the measurements of S parameter.

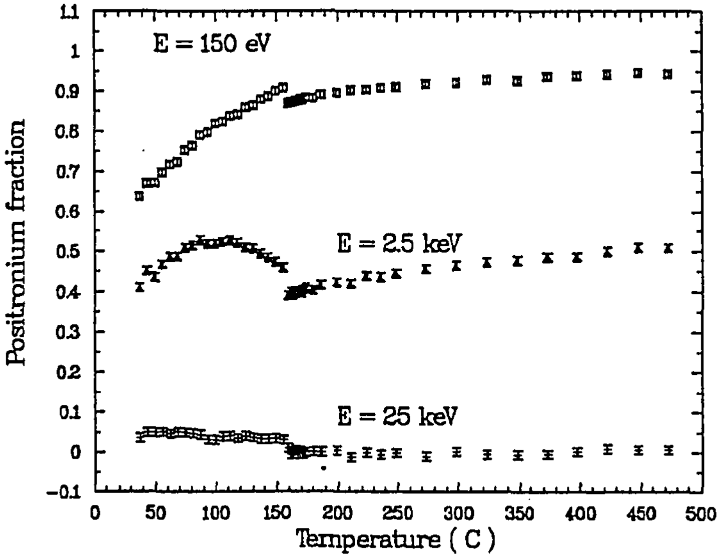

Figure 5.21: Positronium fraction curves at the same three different implantation depths in In, as in figure 5.20.

As with Ga, Bi, and Sn, we can fit the experimental results of thermal desorption of positronium to eq. 5.2 to obtain the activation energy of Ps. The results obtained are E_a = 0.25(0.01) eV, F_o = 0.47(0.03), f_s = 0.46(0.02), and

$\Gamma/\lambda = 8(2) \times 10^3$. The experimental results and the fitted curve are plotted in figure 5.22. The electron work function[116] in In is $\phi_+ = 3.8$ eV; therefore, from equation 5.2, the binding energy of positrons to the surface state is $E_b = 3.25(0.01)$ eV. Nieminen and Hodges[114] calculated the positron binding energy to be $E_b = 2.4$ eV, and the positron work function $\phi_+ = 2.6$ eV. They predicted that a surface state cannot exist in In. But the results in figure 5.22 show that a surface state does exist in liquid and solid In.

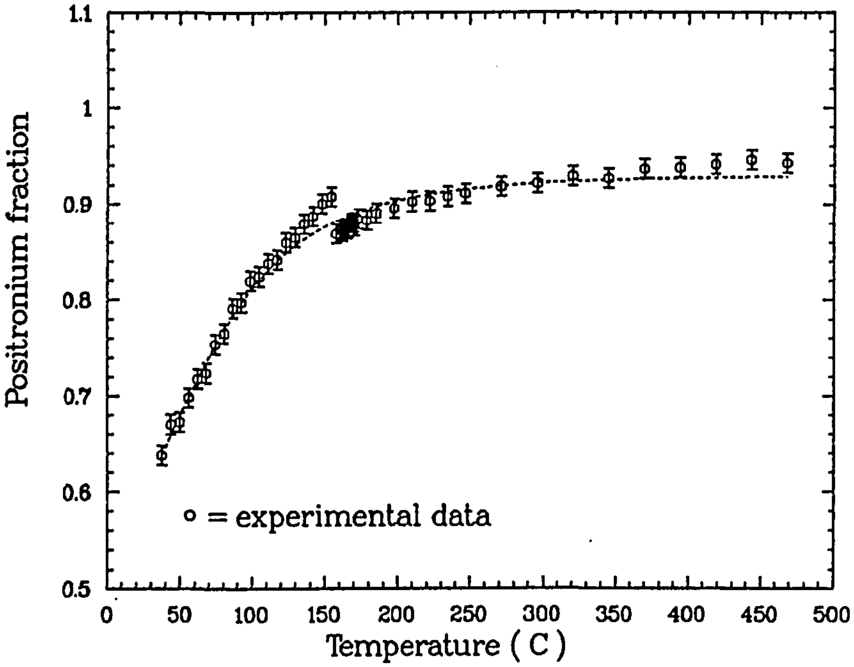

Figure 5.22: Fit to the experimental Ps fraction data. The solid line is obtained from eq. 5.2. The results are $E_a = 0.25(0.01)$ eV, $F_0 = 0.47(0.03)$, $f_s = 0.46(0.02)$ and $\Gamma/\lambda = 8(1) \times 10^3$

5.2 Diffusion length

5.2.1. Analysis of diffusion data

In this section we are going to present the diffusion length results. For all metals investigated, the diffusion length decreases with increasing temperature in the solid phase, decreases or remains constant at melting, and then increases with further increasing temperature in the melt. As it was done in section 5.1, the analysis of the results will be separated according to the state of the positron in the solid phase at temperatures below the melting point. The first group are metals where positrons do not show trapping effects in thermally generated vacancies, namely Ga, Bi, Sn, Na. The second group is Pb, and In, in which positrons get trapped at vacancies.

In section 5.2.1, we will describe in detail the method used to obtain the diffusion length, using the data from Ps fraction and S parameter for each temperature. We will describe the effect of nonthermal positrons in the fitting and a method to estimate the error. Finally, the effect of positrons backscattered from the sample is discussed.

Diffusion length was calculated using the fitting routine VEPFIT[65] described in Chapter II. We used model #5 because a liquid can be considered as a layer with uniform density, and we are interested in fitting the S parameter and the diffusion length independently. The number of intervals defined was 24, which is the value recommended in by Van Veen *et al*[65]. In all cases, the fitted parameters were the diffusion length L_+, the S parameter in the surface state S_{ss}, and the S parameter in the bulk S_{bulk}. The parameters defining the Makhov profile, m and n, were fixed for each metal. In all cases m = 2 and n = 1.6 were chosen, following reference 8. The newer results from Ritley *et al*[53] or McKeown *et al*[52] mentioned in chapter 2 have not been implemented in the fitting routine yet.

We obtained the diffusion length with the following procedure. For each temperature, the F and S parameters were measured. Data on positronium fraction, calibrated according to section 2.5, were fitted with VEPFIT to obtain the fraction f_0 and the diffusion length. The S parameter from Ps was extrapolated from the curves of S as function of energy. At high temperatures and low incident energy, in a clean surface, most incident positrons will form Ps. Therefore, the S parameter obtained will be close to S_{Ps}. The value used was $S_{Ps} = 0.62$.

Subsequently, the S parameter data was fitted using the estimated S_{Ps} and the deduced f_0 as an input to the program. Both values are included in the calibration factor Ω (eq. 2.30). The diffusion length, as obtained from fits to the F parameter is not reliable because the calibration factors R_0, R_1 and P_1/P_0 cannot accurately be obtained. These parameters are also very dependent on the surface condition, which can change during the experiment. Therefore, only the diffusion length obtained from fits to the S parameter are shown.

To estimate the experimental error due to nonthermal positrons, at a given temperature, a grid was placed in front of the sample and biased to +50 and −50 V. For each bias, the S parameter was measured as function of energy, using the same energies as those used to measure the diffusion length. With a bias of 50 V, any nonthermal positron that is re-emitted from the sample, will be returned to it. These positrons have less energy than the incident positrons, and they will tend to increase the value of the S parameter at low incident energies. A fit to these data will give a low diffusion length.

Huomo *et. al*[44] proposed another method to analyze the S and F parameter when nonthermal positrons are present. They chose a minimum implantation energy for the data analysis and assumed that S is a nearly linear function of F. The deviation from linearity is mainly associated with nonthermal positrons reaching the surface. Also, they considered only energies above the energy where that deviation occurs. However, the assumption of linear F and S is only valid for small values of f_o. For $f_o > 0.3$, the nonlinearities are determined mainly by the normalization factor in the S parameter. To illustrate this point, simulated data with different branching ratios for Ps formation, f_o, are shown in figure 5.23. The parameters of the Makhovian profile were chosen to be $m = 2$ and $n = 1.6$. The diffusion length was $L_+ = 600$ Å.

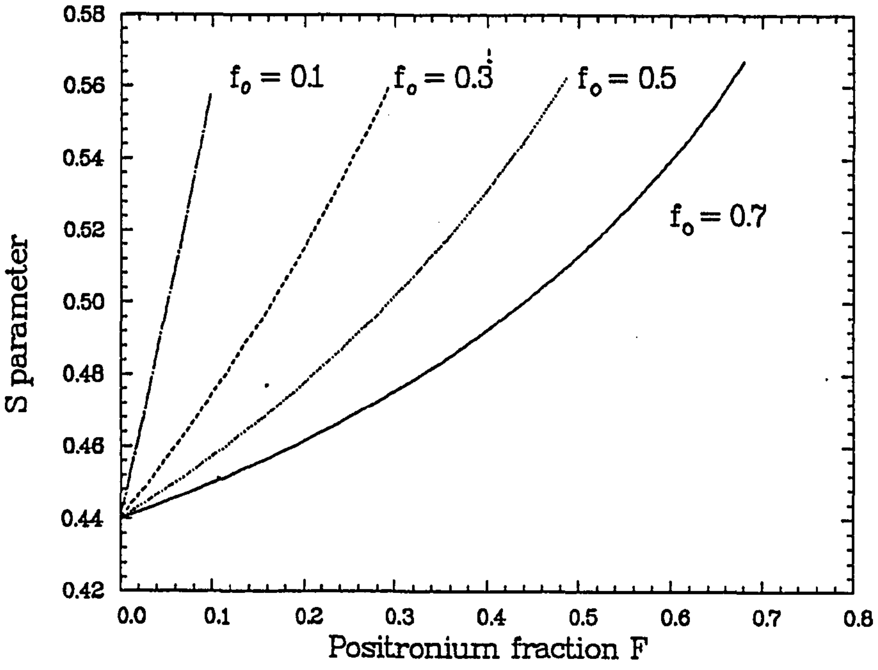

Figure 5.23: Illustration of the dependence of the the S parameter on Ps fraction due to the factor Ω in the normalization factor for S (eq. 2.30). The data was obtained from the diffusion model with $m = 2$, $n = 1.6$, and $L_+ = 600$ Å.

One problem with this method is that the fitted diffusion length increases monotonically as the the energy chosen to start the fit is increased. Consequently, if the wrong minimum energy is chosen, the diffusion lengths obtained from the fittings do not have an upper bound. To illustrate this point, the diffusion length in Bi from fits to the S parameter data (T = 408 °C) are shown in figure 5.24.

The effect of backscattered positrons in the analysis of the diffusion length is

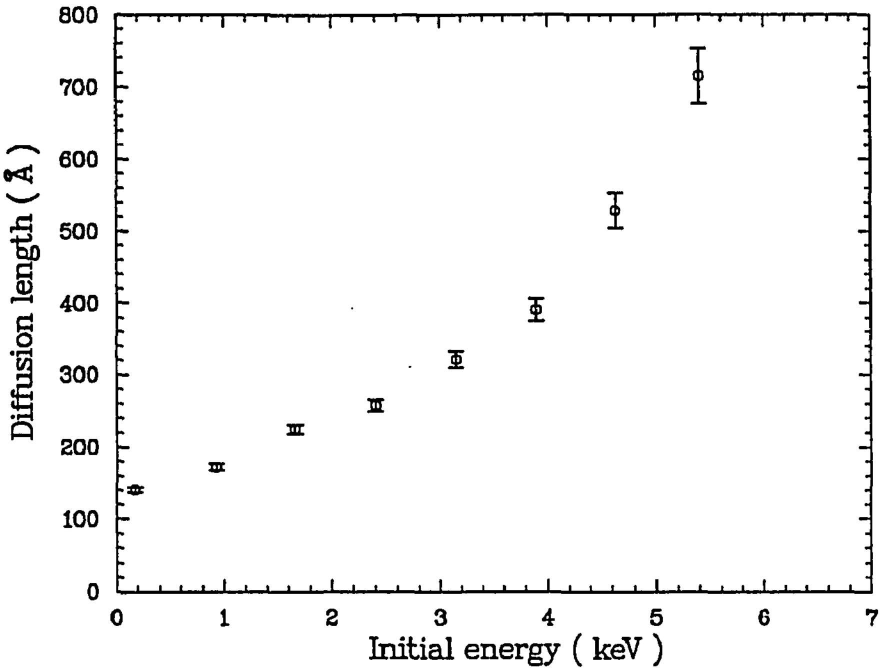

Figure 5.24: Fits to the S parameter data in Bi at T = 408 °C. The diffusion length was calculated with VEPFIT, choosing different energies to start the fits.

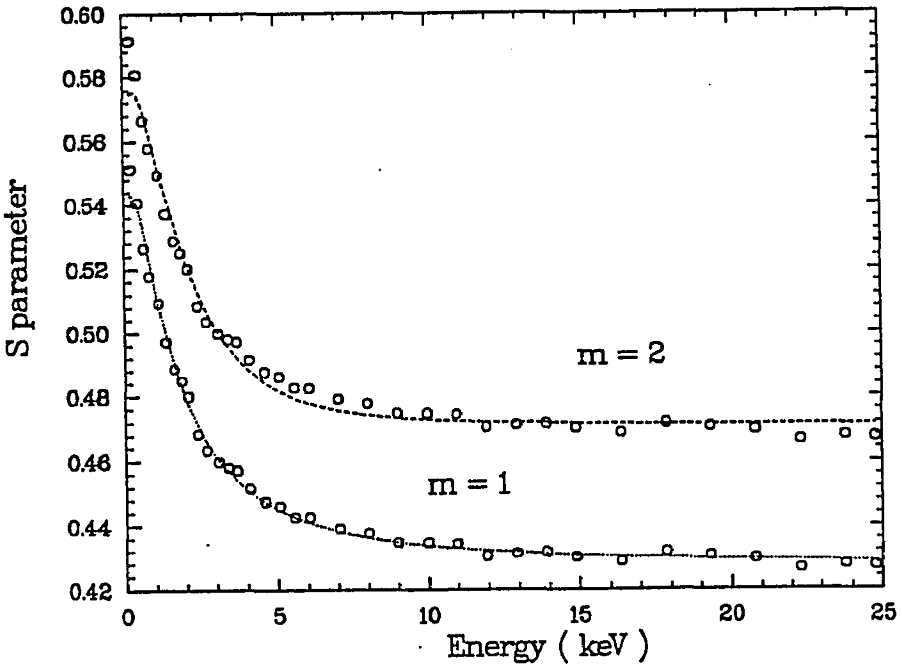

Figure 5.25: The effect of backscattered positrons in the analysis of the data. The dashed line shows a fit to the S data in Pb, with m = 1 and m = 2. A better fit is obtained with m = 1, which shows that after implantation there are more positrons close to the surface in metals with high Z.

stronger in materials with high Z (Bi, Pb, Sn), where the probability of backscattering by the ion cores is large. These positrons, which have lower energy than the incident beam, are trapped in the magnetic field and can later return to the sample. As a consequence, there are more positrons close to the surface than is predicted with the Makhovian profile having m = 2. Therefore the implantation profile is best described by a shaping parameter m less than 2 for these materials. For lead, a better fit to the the S parameter curves is found with m = 1, rather than m = 2 (figure 5.25).

5.2.2 Measurements of Diffusion length in Ga, Bi, Sn, and Na

Gallium

The data used to calculate the diffusion length were taken at a constant temperature, with the energy being varied from 100 to 20 keV. More points were measured from 100 eV to 2 keV because the changes in S or F parameter were larger in this energy range than at high incident energies. Measurements of S as function of energy are shown in figure 5.26 for different temperatures.

The fits were performed with the fitting routine VEPFIT. The values used for m and n were 2 and 1.4, respectively. The second result was used because preliminary Monte Carlo simulations[49] of the stopping profile show n $\approx$ 1.4 for Ga

The fitted results are shown in figure 5.27. Below the melting point, the diffusion length is $L_+ \approx 1200(100)$ Å. The diffusion coefficient D_+ can be calculated using the definition in eq. (2.36). The experimental lifetime in solid Ga is τ =193(5) ps, as given by ref. 104. Thus we obtain $D_+ = 0.75(0.07)$ cm^2/s. This result is larger than the theoretical value obtained by by Bergersen *et al*[27] of $D_+ = 0.4 \times 10^{-4}$ m^2/s.

Upon melting, the diffusion length drops to $L_+ \approx 60(5)$ Å, which represents a change of almost 2 orders of magnitude. This large drop confirms the results obtained previously,[16,78,79] that below the melting point positrons are in a Bloch-like state and the diffusion length is long. Upon melting, all become trapped and there is little diffusion.

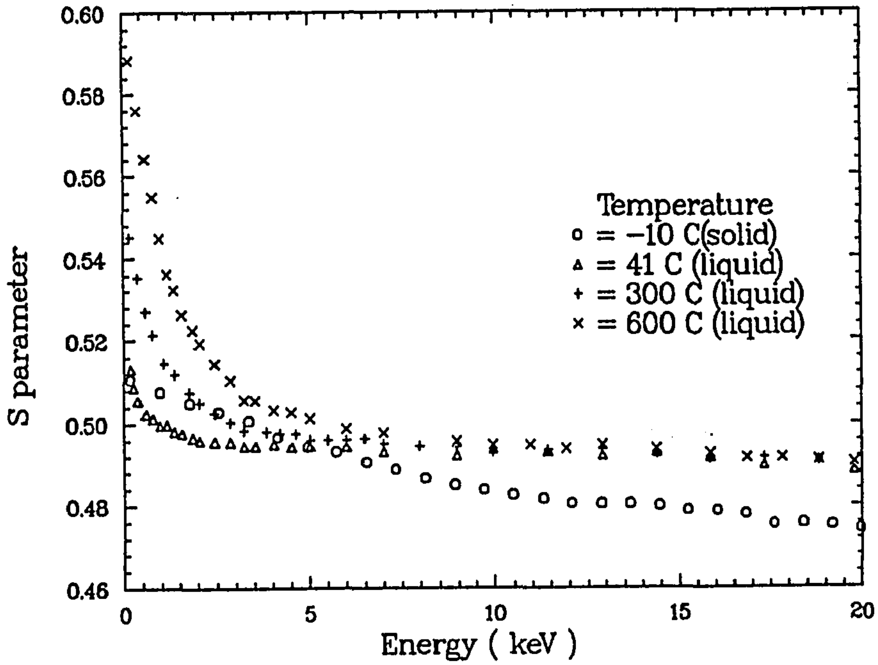

Figure 5.26: S parameter in Ga as function of the incident energy for different temperatures.

As the temperature is increased further, there is an exponential increase in the diffusion length that starts at T $\approx$ 150°C

The errors in the fits introduced by nonthermal positrons escaping through the surface are estimated measuring the S parameter with a grid in front of the sample. Three data sets are shown in figure 5.28. The grid was biased at +50 V, −50 V and 0 V.

A possible explanation for the increase in the diffusion length in the liquid phase is the following. The time it takes to trap a positron[6] in a vacancy or defect is of the order of 10^{-15} s, which is much faster than the ionic motion in liquids[1,2] ($\sim 10^{-12}$ s). Thus, the positron can be seen as interacting with an almost static array of ions and can react to any ionic displacement. Therefore, density fluctuations on a time scale of 10^{-12} s could produce potential wells strong enough to trap positrons. These traps could later disappear, forcing the positron to jump to the next fluctuation. Thus, the diffusion in liquid Ga can be seen as a hopping motion between traps. Trapping and detrapping could happen many times in the lifetime of the positron ($\sim 10^{-10}$ s). As the temperature increases, the frequency of these fluctuations would increase, increasing the diffusion length. These fluctuations also can affect the size of stable traps (with lifetime $> 10^{-12}$ s) which, in turn, would alter the diffusion length. Thermally activated detrapping alone is unlikely to explain change in the diffusion length because the thermal energy of the positron is much less than the binding energy of the trap.[12] The fluctuation in the binding energy of the traps also can affect any stable traps in the liquid. As the temperature increases, these fluctuation would force positrons out, increasing the diffusion length.

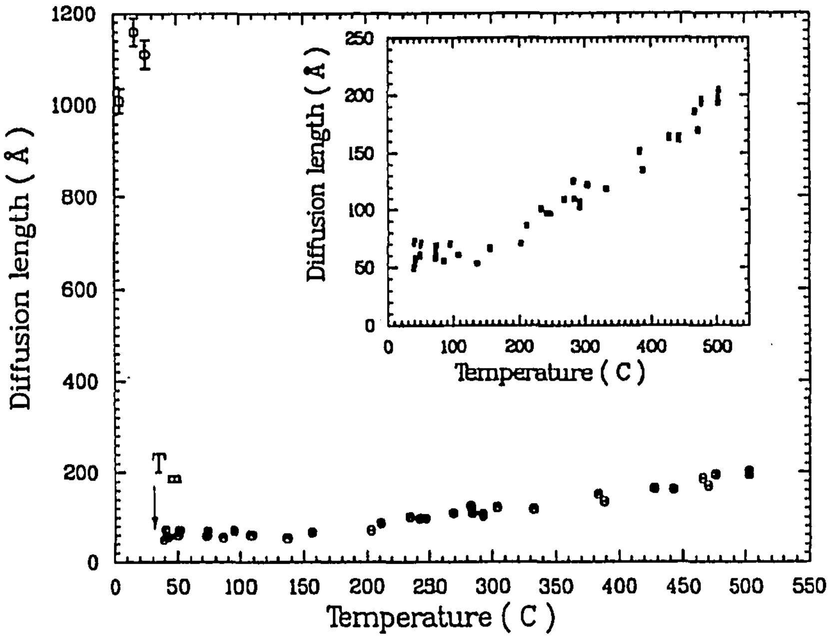

Figure 5.27: Diffusion length results for Ga as function of temperature. A large drop is observed on melting. The inset shows the exponential increase in the diffusion length in the liquid phase. The error bars shown are statistical calculations from the fitting routine.

Such fluctuations can explain the decrease in the lifetime with higher temperatures[16], because the lifetime will be given by the weighted average of the lifetime in the traps (260 ps) and the lifetime in the bulk (193 ps).

An alternative explanation is that the positron pushes away the surrounding atoms to create a potential well where they get trapped[107,124,125] (self-trapping). Leung *et al.*[125] modeled the metal by an elastic continuum with bulk modulus B. The positron interacts with this continuum via a deformation potential. They concluded that if $E_d^2/B < 70$ [Hartree a_0^3], positrons do not selftrap in the metal. E_d is the positron deformation potential, ($E_d \approx -\frac{2}{3}E_F$, E_F is the Fermi energy in the liquid), and B is the bulk modulus.

For Ga, we obtain $E_d^2/B = 44$ Hartree a_0^3 a value less than the limit required to have a localized positron.[125]

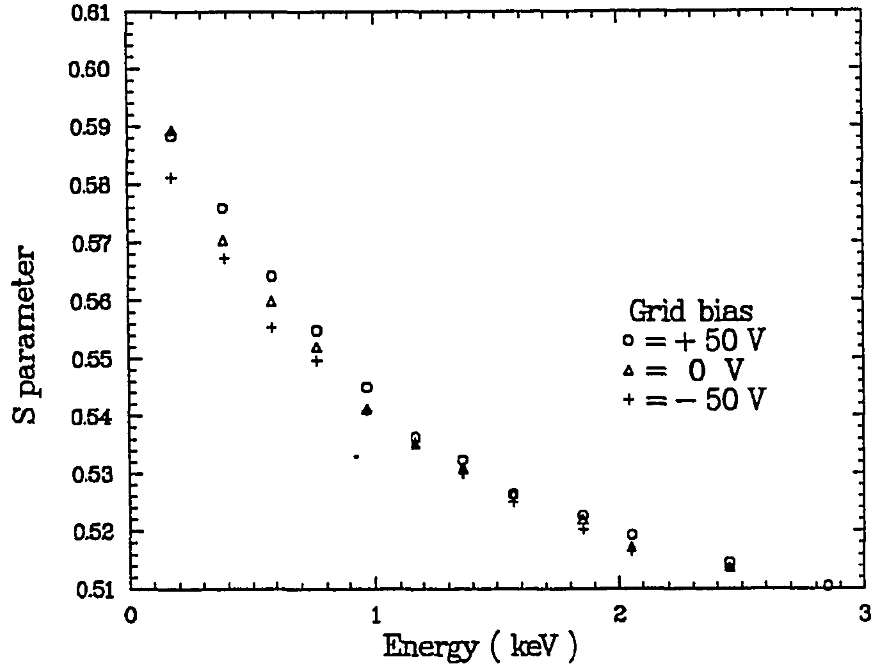

Figure 5.28: S parameter for T = 600 °C, with a grid in front of the sample at three different biases. These data were used to estimate the experimental error in the fitting routine from nonthermal positrons.

Bismuth

The S parameter data used to calculate the diffusion lengths is shown in figure 5.29 at different temperatures, the energy ranging from 100 eV to 25 keV. Figure 5.30 gives the diffusion length results for Bi. At room temperature $L_+ \approx 650$ Å. However, this value may be lower than the real value because of systematic errors in the fitting routine. In VEPFIT, it is assumed that at high incident energies all positrons annihilate in the bulk. However, the maximum energy reached by the Liquid Metals Beam is 25 keV. At these energies some positrons can still reach the surface. Figure 5.7 shows that below the melting point, the Ps fraction at E = 25 keV is not exactly zero.

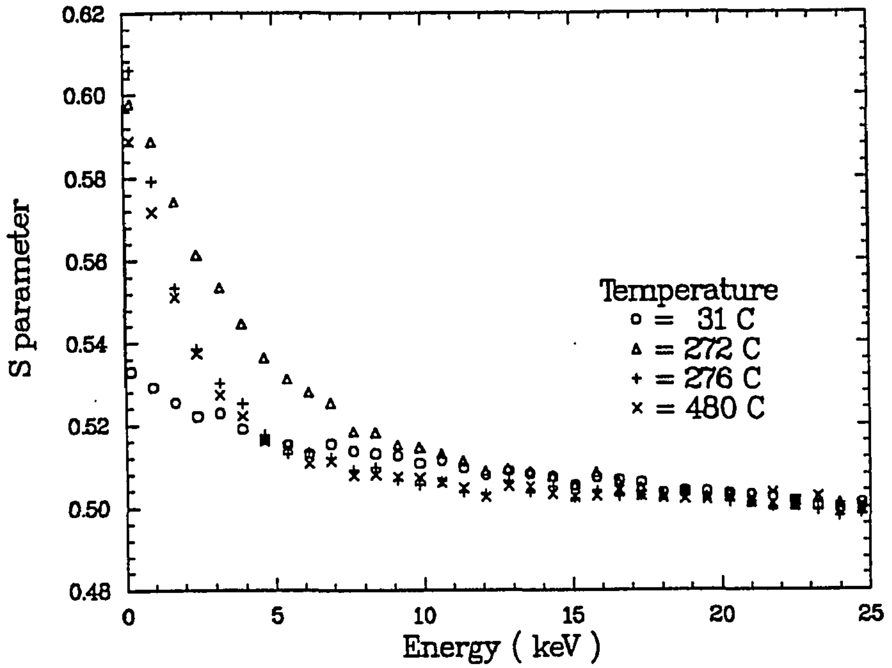

Figure 5.29: S parameter in Bi plotted against the incident energy for four temperatures. The circles and triangles are in solid Bi. "+" and "×" are in liquid Bi.

Thus, S(E=25 keV) $\neq S_{bulk}$ and the diffusion length can not be calculated accurately. The error bars in the solid phase are larger than in the liquid because the dynamic range used to fit the diffusion length is smaller at lower temperatures. At T = 31 °C, the S parameter varies from ~ 0.528 at E = 100 keV to ~ 0.50 at

E = 25 keV. While at T = 276 °C, the change is from S ~ 0.603 to S ~ 0.50.

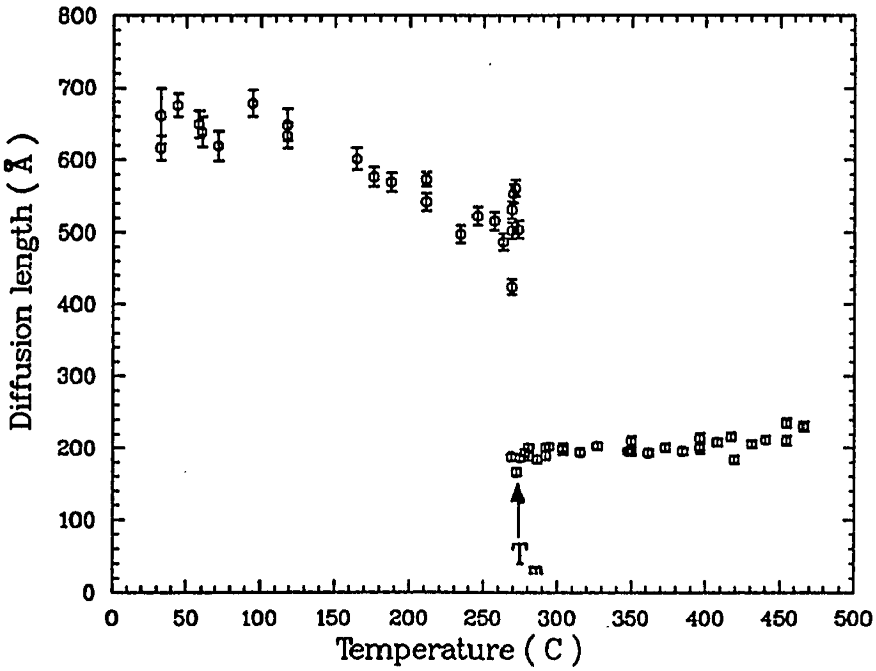

Figure 5.30: Diffusion length results in solid and liquid Bi plotted against temperature. There is a large drop in the diffusion length at the melting point.

The theoretical value of the diffusion length can be obtained from the formulas in reference 27. At T = 25 °C, we have $D_+ = 0.33$ cm^2/s (using $E_d = -\frac{2}{3}E_F = -6.6$ eV, and $m^* = 1.8m_e$). The diffusion length is given by $L_+ = \sqrt{D_+\tau}$. The bulk lifetime is^{105} $\tau = 258(3)$ ps. Thus, $L_+ = 920$ Å, is higher than our experimental value. Apparently, inaccurate determination of the asymptotic value of S can lead to smaller values for L_+.

Close to the melting point, $L_+ \approx 500$ Å for solid Bi. At this temperature the problem of inaccuracy remains, and the deduced diffusion length may be lower than the actual length. The theoretical value for the diffusion length calculated according to ref. 27 is $L_+ = 790$ Å at T = 270 °C.

Upon melting, L_+ drops to ≈ 190 Å. An estimate of the experimental error from nonthermal positrons is ± 40 Å in the solid, and ± 20 Å in the liquid. These errors are estimated from measurements of the S parameter with a grid in front of the sample. Three data sets are shown in figure 5.31. The bias applied was +50 V, -50 V and 0 V. At T = 280 °C, and with a bias of +50 V in the grid, the result obtained was $L_+ = 424$ Å. With a bias of -50 V, the results is $L_+ = 531$ Å. With the grid at ground the results is $L_+ = 502$ Å.

In liquid Bi, at high incident energies, all positrons annihilate in the bulk (as seen in figure 5.7, for $z \approx 6200$ Å) and the calculated diffusion length is not underestimated.

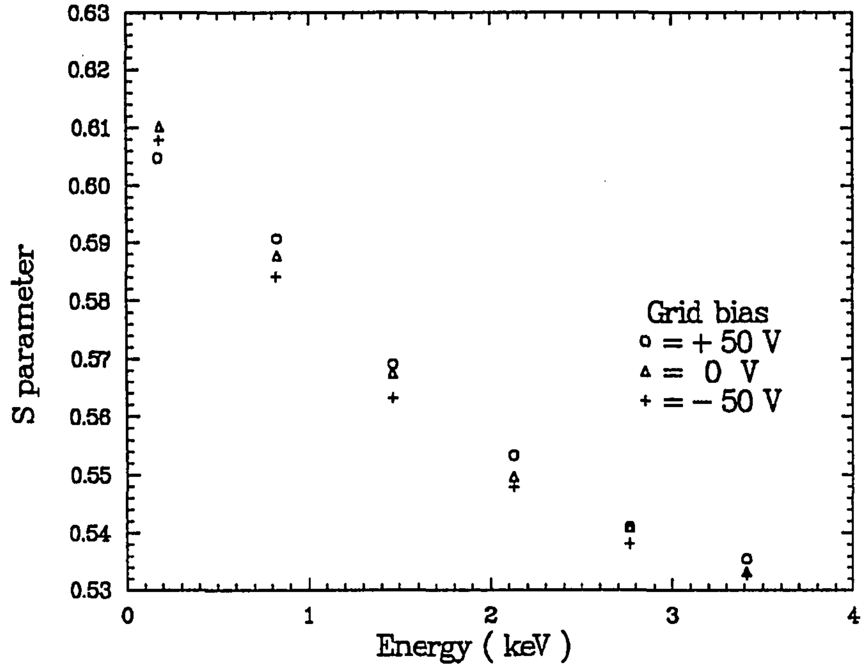

Figure 5.31: S parameter in Bi for T = 280 °C, with a grid in front of the sample at three different bias voltages. These data were used to estimate the experimental error in the fitting routine from nonthermal positrons.

In Bi, the drop in the diffusion length observed at the melting point can be explained as increased scattering by the more mobile ions in liquid Bi, or by trapping. Several different traps can exist in the melt. Above the melting point, there is a slight linear increase in the diffusion length with increasing temperature. A simple least squares fit gives $L_+ = 0.15(0.02)T$ [Å/°C] + 149(6) Å. In contrast to Ga, the increase in Bi is linear with a much smaller slope which may indicate that traps in Ga are more shallow than traps in Bi, or that the ion mobility is higher in Ga than in Bi.

As in Ga, the small increase could be due to fluctuations in the size of the traps. Because positron trapping occurs in a time scale of $\sim 10^{-15}$s, it can react to any ionic motion ($\sim 10^{-12}$s). When the trap decreases in size, the positron is forced out of it, and the diffusion length increases.

Self-trapping seems not to play a role in liquid Bi. From reference 125, we obtain $E_d^2/B = 64$ [Hartree a_0^3], with $E_d \approx -\frac{2}{3}E_F = -6.7$ eV, which is lower than $E_d^2/B = 70$ [Hartree a_0^3], the limiting value for selftrapping. This result shows that positrons are essentially a nonperturbing probe in liquid Bi.

Sodium

Because there are no bound states in the surface of sodium, and the positron work function[31] is positive, $\phi_+ = 5.6$ eV, thermal positrons which reach the surface return to the bulk, where they subsequently annihilate. Therefore, when the S parameter is measured as function of the energy, there is no signal from the surface. This assumption was basic to extracting the diffusion length with the VEPFIT program. The S parameter plotted against energy is shown in figure 5.32. The small difference observed between low and high incident energy is attributed to nonthermal positronium.

Positronium fraction is plotted versus incident energy in figure 5.33; there is a rapid decrease from E = 100 eV to E = 1 keV. Theoretical calculations[31] show that the Ps work function is positive, $\phi_{Ps} = 0.4$ eV, thus, no Ps should be formed at the surface. The F parameter seen in figure 5.32 at low incident energies is attributed to nonthermal positrons, which have enough energy to overcome the potential step at the surface and leave the sample. Because the mean free path for nonthermal positrons is short[31], they can reach the surface only if the mean implantation depth is small[44]. Thus the number of nonthermal positrons reaching the surface decreases rapidly as the incident energy is increased.

For comparison, the experimental results are plotted along with the fraction of positronium that would be formed if a fraction f_0 of the thermal positrons that reach the surface form Ps. The theoretical value[115] of the diffusion length at room temperature ($D_+ \approx 1.29$ cm^2/s) can be inserted in the diffusion equation. Then, the number of positrons that return to the surface can be calculated for any given energy. If $f_0 \approx 0.09$, which is the value obtained experimentally from figure 5.33. Then, the amount of positronium formed from thermal positrons diffusing to the surface can be calculated for any given energy, as shown by the solid line in fig. 5.33. Because the measured positronium fraction decreases faster than the theoretical, we can conclude that the observed results at low incident energy come from nonthermal positrons.

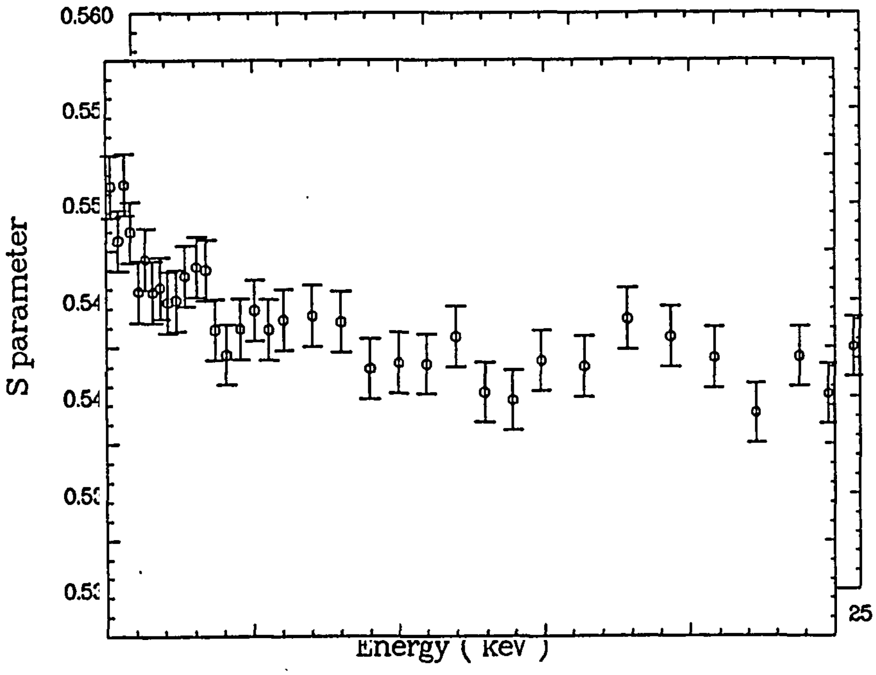

Figure 5.32: S parameter in Na, plotted as function of the incident energy. There is little change between low and high incident energies.

Self-trapping does not seem to play a role in liquid Na. Using the deformation potential from reference 115, $E_d = -2.59$ eV, $B = 5.37\times10^{10}$ dy/cm^2 in liquid Na[1]. $E_d^2/B = 31$ [Hartree a_0^3]. This value is lower than 70 [Hartree a_0^3], the limiting value for self-trapping. This result shows that positrons are essentially a nonperturbing probe in liquid Na.

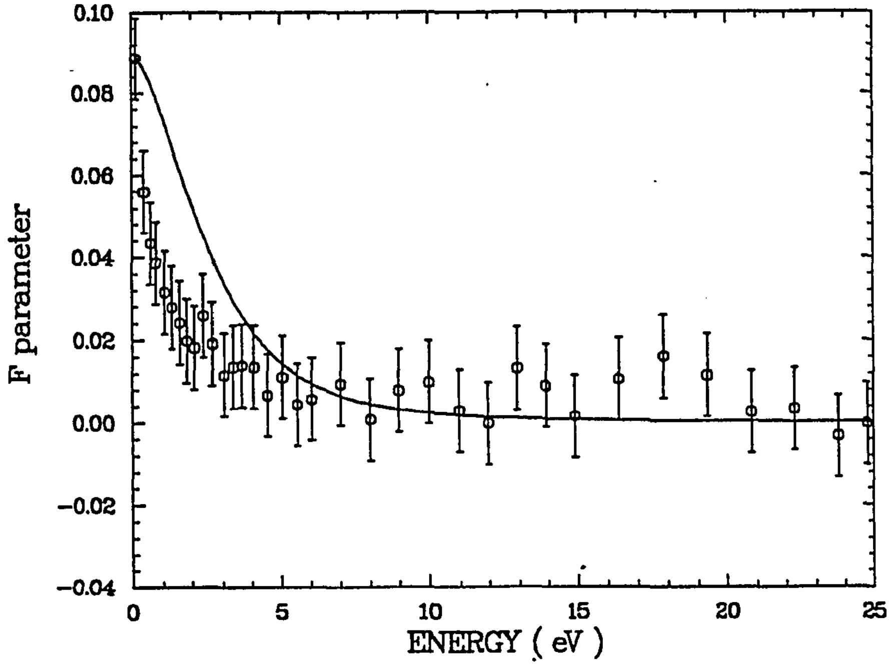

Figure 5.33: Positronium fraction in Na, as function of the incident energy. The solid line is the amount of Ps that would be formed if a fraction f_o of the thermal positrons that return to the surface form Ps.

Tin

The S parameter data used to calculate the diffusion lengths is shown in figure 5.34 for four temperatures, with the energy ranging from 100 eV to 25 keV. As in the other metals, more points were taken in the energy range from 100 eV to 5 keV, where the change is most pronounced.

The diffusion lengths for Sn are shown in fig 5.35; they are very similar to the diffusion lengths in Bi. In both metals, positrons are in a Bloch-like state in the solid phase. Accordingly, the diffusion length decreases as $\approx T^{-1/4}$ with temperature because phonon scattering is the dominant interaction between positrons and the metal. At room temperature $L_+ \approx 950(50)$ Å. At temperatures below ≈ 100°C, the diffusion length is not accurate because the energy range of the beam is not high enough to reach the bulk value of S. Thus, the fitting routine is not accurate.

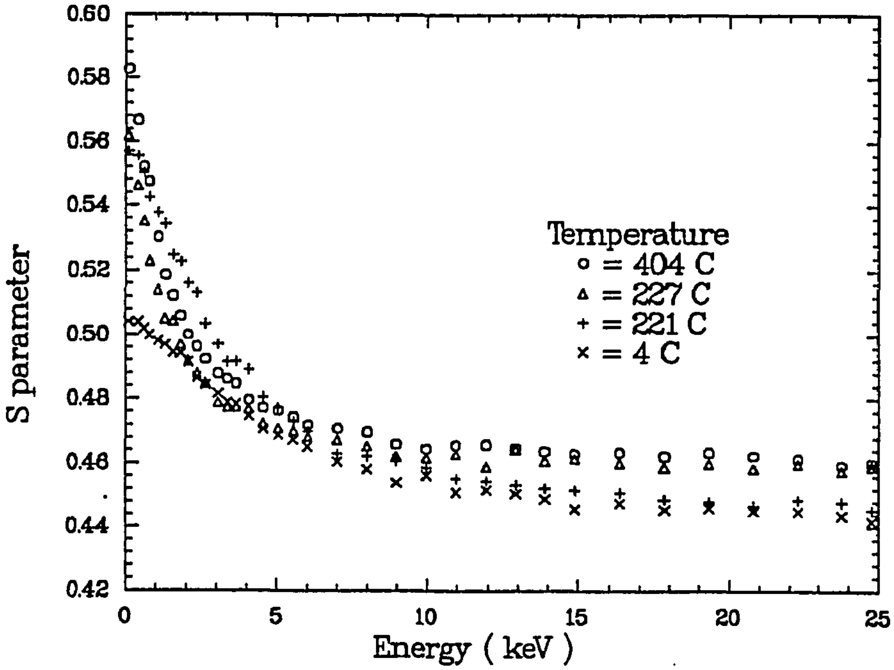

Figure 5.34: S parameter measurements for Sn for four temperatures plotted against the energy. The circles and triangles are in liquid Sn. "+" and "×" are in solid Sn.

The theoretical value for the diffusion length can be obtained from the formulas in reference 27. At T = 300 °C we have $D_+ = 1.12$ cm^2/s, using $E_d = -2/3E_F = 6.7$ eV, and $m^* = 1.8m_e$. The diffusion length is given by $L_+ = \sqrt{D_+\tau}$ and the bulk lifetime is[102] $\tau = 202(5)$ ps. Thus, the theoretical value of the diffusion length is $L_+ \approx 1500$ Å. This value is much larger than the diffusion length in figure 5.32 ($L_+ \approx 950$ Å. at T = 30 °C). An inaccurate asymptotic value of S can lead to smaller values for L_+.

Just below the melting point $L_+ \approx 750(50)$ Å. The theoretical value at this temperature is $L_+ \approx 1100$ Å. Upon melting, the diffusion length drops to $\approx 260(20)$

Å. The error in L_+ was calculated from the maximun error in the fitting routine. In Sn, the drop observed at the melting point can be explained by vacancy trapping or increased scattering with the more mobile ions in liquid Sn. The increase in S_{bulk} at the melting point seems to indicate positron trapping. A more accurate determination of positron trapping in liquid Sn should be performed using lifetime techniques.

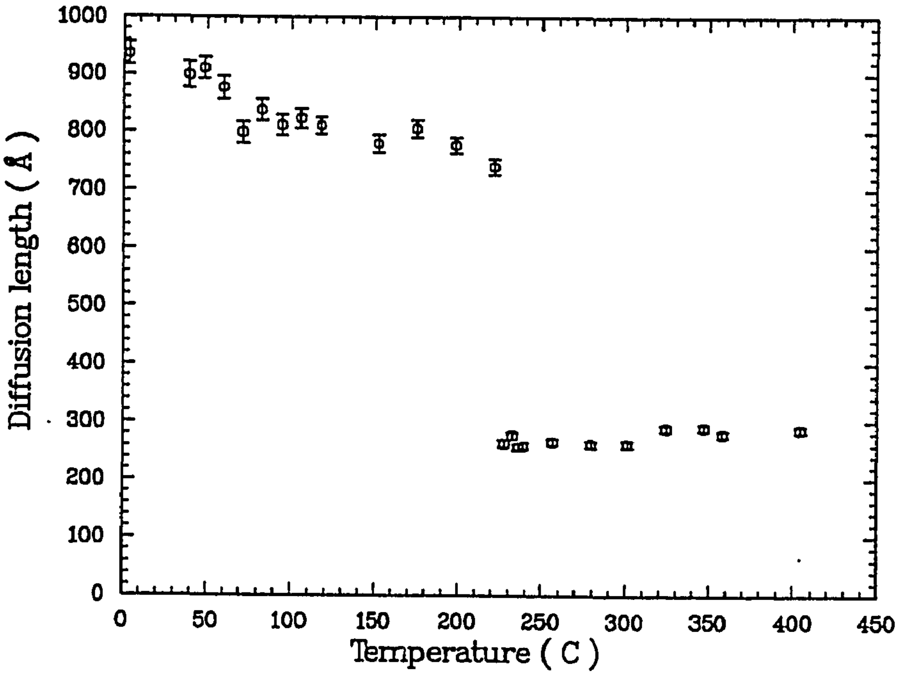

Figure 5.35: Diffusion length results for Sn above and below the melting point as a function of the temperature. Part of the data used for the fits is shown in figure 5.35.

Early Ps fraction measurements with a positron beam[121] showed that E_0, which is related to the diffusion length by[8] $E_0 = L_+/A$ decreased as the temperature was increased. Lynn *et. al*[121] attributed this decrease to trapping in thermally generated vacancies. However their data has incident energies only up to 5 keV, which may be too low to extract the correct E_0. The diffusion length that they extracted is $L_+ \approx 300$ Å, which is smaller than our results.

There is a slight linear increase in the diffusion length with increasing temperature. A least-squares fit gives $L_+ = 0.163(0.029)T$ [Å/°C] + 224(9) [Å]. As in Ga, this increase in the diffusion length can be explained by positrons hopping between traps. The increase is less pronounced than in Ga, which suggests that the binding energy of the trap is higher in Sn than in Ga.

In liquid Sn, self-trapping does not to seem be the reason for positron trapping. From reference 125, we obtain for liquid Sn $E_d = -6.6$ eV, $B = 3.6 \times 10^{11}$ dy/cm^2. Then $E_d^2/B = 47$ [Hartree a_0^3] which is lower than 70 [Hartree a_0^3], the limiting value required for self-trapping. This result shows that positrons are essentially a nonperturbing probe in liquid Sn.

5.2.3 Measurements of diffusion length in Pb and In

Pb and In show a pronounced trapping effect below the melting point, as was evidenced by S_{bulk} and also by the diffusion length. A rapid decrease in the diffusion length occurs when positrons start to get trapped at thermally generated vacancies. Upon melting, the trapping sites may change, but the diffusion characteristics are not significantly affected. Only a small decrease in the diffusion length is seen.

Lead

As previously, the S parameter was measured as function of the incident energy, for a given temperature. The energy ranged from 100 eV to 25 keV for each temperature (figure 5 36). The increase in S_{bulk} at temperatures below the melting point is caused by thermal vacancy trapping of positrons. Saturation trapping occurs close to the melting point;[19] thus, there is no further increase in S_{bulk}. The results of fits to the S data are shown in figure 5.37, where the diffusion length is plotted against temperature.

At room temperature, $L_+ \approx 350$ Å. However, this value may not be accurate, because at low temperatures the S parameter at 25 keV has a small contribution from the surface. In the fitting routine, it is assumed that S_{bulk} can be reached at high incident energies; this is not possible in the Liquid Metals Beam for Pb.

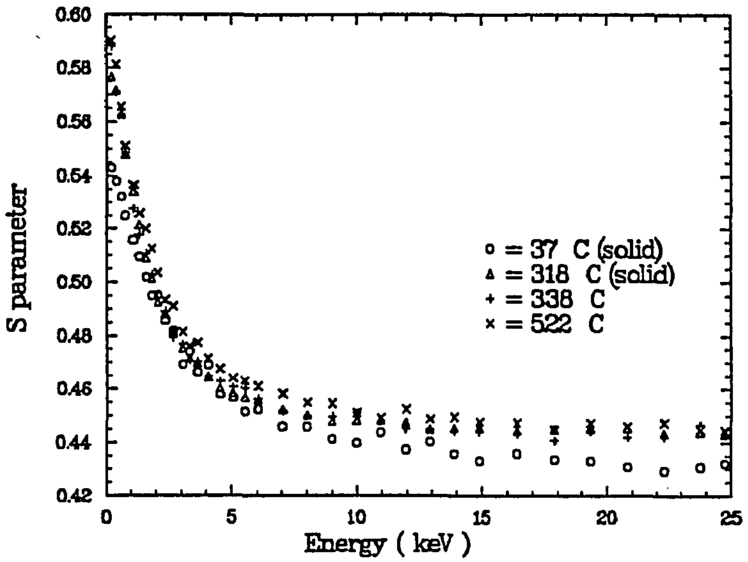

Figure 5.30: Plot of the S parameter versus incident energy for different temperatures. The circles and triangles are in solid Pb, the "+" and "×" are in liquid Pb.

The diffusion coefficient can be obtained from $D_+ = L_+^2/\tau$. The bulk lifetime is[108] $\tau = 168$ ps in solid Pb, and $D_+ = 0.07$ cm2/s. The theoretical value for the diffusion length was obtained from reference 115. At T = 300 °C we have $D_+ = 0.86$ cm^2/s, which is an order of magnitude smaller than the calculated result. An inaccurate determination of the asymptotic value of S can lead to unrealistically small values for L_+.

As the temperature increases, the diffusion length decreases rapidly because of the combined effect of phonon scattering and thermal vacancy trapping. The diffusion length just below the melting point is ≈ 180(20) Å. At these temperatures, diffusion is determined by trapping, and the relation $D_+ \sim T^{-1/2}$ is no longer valid. Upon melting, no change was observed in the diffusion length. This result is consistent with the assumption that all positrons are trapped in the solid phase below the melting point. Upon melting, an increase in the concentration of traps, or change in the electronic structure does not affect the diffusion of trapped positrons.

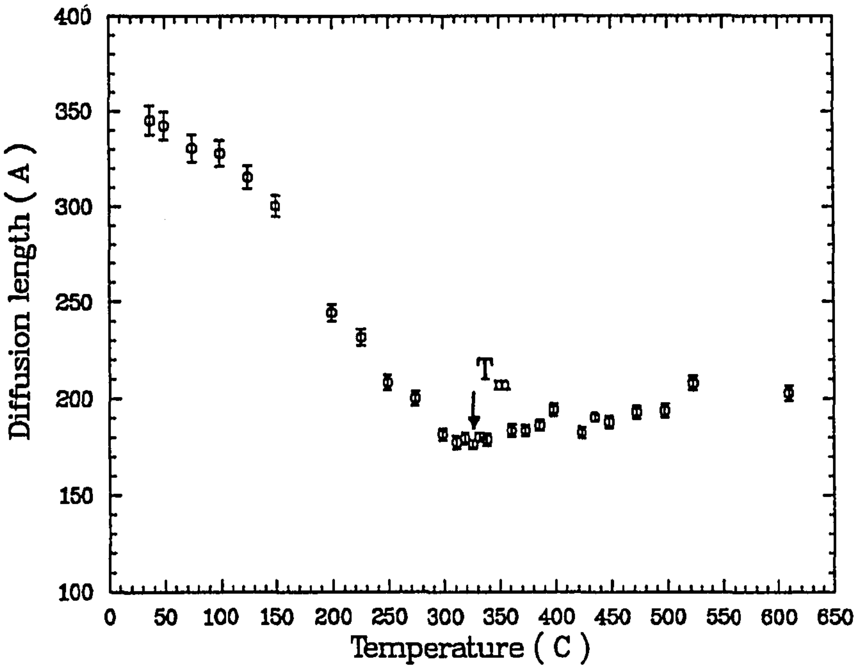

Figure 5.37: Fits to the S parameter data in Pb. The melting point is indicated with an arrow. No change in the diffusion length is observed within the experimental error.

The error bars in the diffusion length are obtained from the fitting routine. In contrast to any of the previous metals, we did not observe nonthermal positrons or Ps being emitted from the sample. In figure 5.38, we show plots of S and F parameter taken at one temperature with a grid in front of the sample biased to 0, 50, and −50 V.

As discussed, the positronium work function is negative and there is a high fraction of Ps at all temperatures. Thus, nonthermal Ps cannot be distinguished from thermal Ps.

As the temperature increases, the diffusion length increases slightly. This effect has been observed for all metals. As in Ga or Sn, a possible explanation is that thermal fluctuations in the size of the traps can release the positron, creating a hopping motion between different kind of traps or between the free state and the traps. This hopping motion increases the diffusion length.

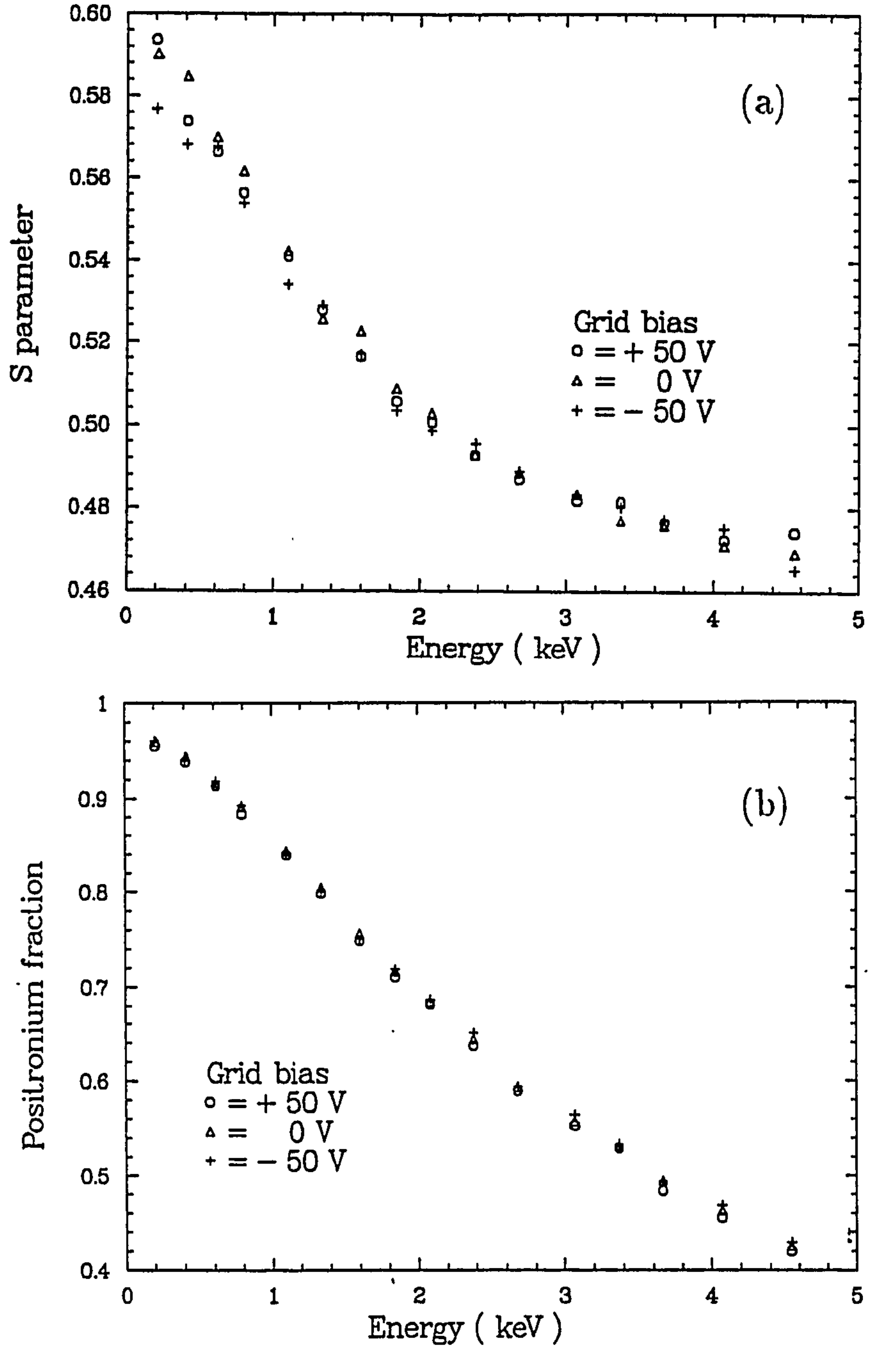

Figure 5.38: (a) S parameter in Pb for three different grid bias, at T = 310 °C. (b) Positronium fraction at the same temperature as in a). The S and F data were measured simultaneously.

A linear-squares fit to the diffusion length in liquid Pb gives $L_+ = 0.095$ (0.012)T [Å/°C] + 149(5) Å. The slope of the diffusion length is less pronounced than in Ga, or Sn, which suggests that the binding to the traps is stronger in Pb than in the other metals.

In liquid Pb, self-trapping does not seems to be the reason for positron trapping. From reference 115, we obtain $E_d = -6.39$ eV, $B = 2.86 \times 10^{11}$ dy/cm^2 in liquid Pb[1]. Then, $E_d^2/B = 57$ [Hartree a_0^3] which is lower than 70 [Hartree a_0^3], the limiting value required for self-trapping. This result shows that positrons are essentially a nonperturbing probe in liquid Pb.

Nonthermal positrons do not play a role in the calculations of diffusion length. There is no difference in the measurements of the S parameter with a grid in front of the sample for different bias voltages. This is shown in figure 5.36 for Pb at T = 40 °C.

Indium

Previous studies with In show a pronounced trapping effect in the solid phase as the temperature is increased. Therefore, as in Pb, there is a strong variation of the diffusion length with temperature. Some of the data used to calculate the diffusion length at different temperatures is shown in figure 5.39. The energy was varied from 100 eV to 25 keV.

Figure 5.40 shows the results of the fit to the S parameter. At room temperature, $L_+ \approx 530$Å. As in Pb, Bi and Sn, this value may not be accurate, because at the highest incident energy (E = 25 keV), and low temperatures some positrons still reach the surface. Thus, the S parameter is higher than the bulk value and the fitting diffusion length cannot be calculated accurately. The diffusion coefficient can be calculated from eq. (2.4). At room temperature, the bulk lifetime is $\tau = 220(4)$ ps,[109] and $D_+ = 0.13$ cm^2/s. The theoretical results for the diffusion coefficient can be obtained from reference 27. At T = 300 °C, $D_+ = 0.4$ cm^2/s, which is larger than the experimental results.

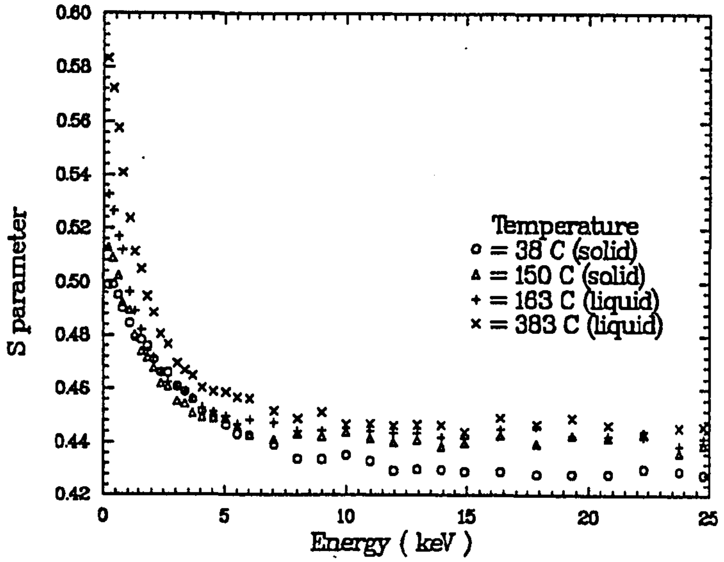

Figure 5.39: Representative S parameter data in In used to calculate the diffusion length at different temperatures.

As in Pb, Bi, and Sn, inaccurate determination of the asymptotic value of S can lead to smaller values for L_+. A rapid decrease in the diffusion length is seen from 50 °C to the melting point, which is attributed to trapping in thermally generated vacancies[17]. This decrease is much faster than the decrease in metals with no vacancy trapping (Ga, Bi, or Sn) in the solid phase. Close to the melting point, the diffusion length is $\approx$ 245(20) Å. The lifetime at this temperature[109] in solid In is τ = 280(5) ps. Thus, the diffusion constant is $D_+ = 2.1 \times 10^{-2}$ cm^2/s. The small drop in L_+ observed at the melting point can be explained by an increase in the trapping fraction from $\approx$ 83% to complete trapping[19].

As the temperature in increased in the liquid phase, the diffusion length increases linearly. A least-squares fit gives $L_+ = 0.123(0.014)$ T [Å/ °C] + 205(4) Å. This increase also seems to be related to hopping between traps in the liquid phase.

Self-trapping does not seem to play a role in liquid In. Using the criteria from reference 125, we obtain $E_d = -5.6$ eV, $B = 3.38 \times 10^{11}$ dy/cm^2 in liquid In[1]. Therefore, E_d^2/B = 31 [Hartree a_0^3], which is lower than 70 [Hartree a_0^3], the limiting value required for self-trapping. This result shows that positrons are essentially a nonperturbing probe in liquid In.

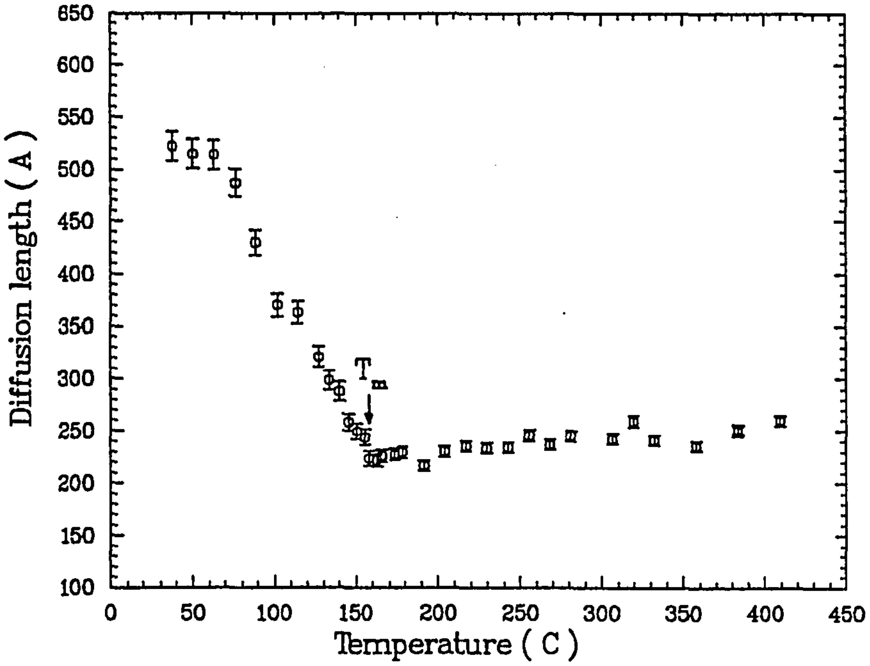

Figure 5.40: Diffusion length in In as function of the temperature, obtained from fits to the S parameter. Positronium fraction has been included in the fit.

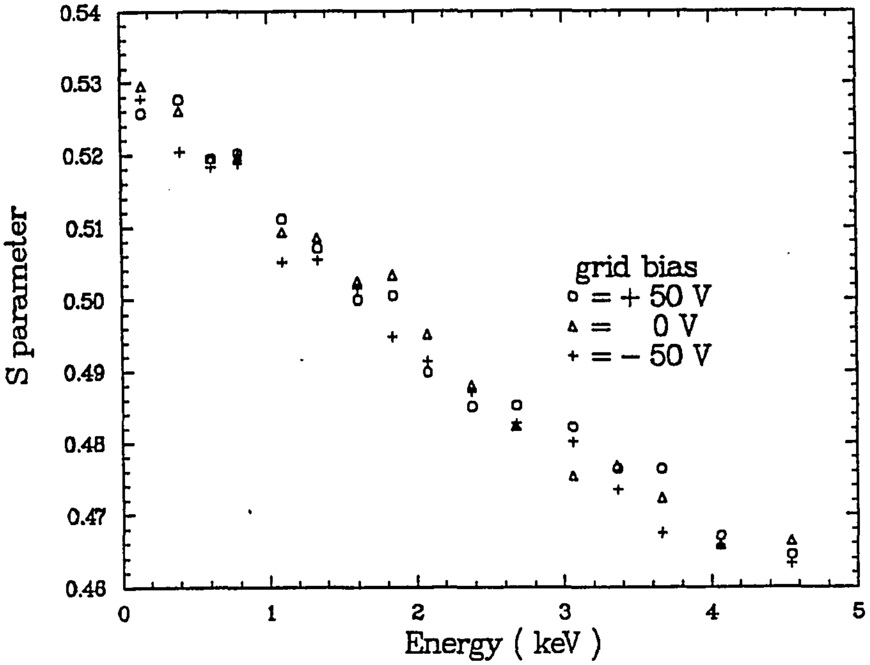

Figure 5.41: S parameter in In for three different grid bias, at T = 45 °C.

Nonthermal positrons do not seem to play a role in the calculations of diffusion length. Measurements of the S parameter with a grid in front of the sample do not show any difference for different bias voltages as shown in figure 5.41 for T = 40 °C. This was also the case for Pb.

5.3 Nonthermal-positron effects

The process of energy loss of charged particles in a solid or liquid recently has received much attention[126–129]. The analysis of the S and F parameter data strongly dependes on a knowledge of the positron implantation profile[129], which is determined by the mechanisms of energy loss available to the positrons. As discussed in Chapter II, at energies below 1 keV, the positron can lose energy by inelastic scattering from conduction electrons and phonons as well as from defects. When positrons are implanted close to the surface, they can be re-emitted before complete thermalization if their energy is higher than the positron work function. We will discuss information on the energy loss mechanisms provided by nonthermal positrons.

The energy analysis is performed with a two parallel grids in front of the sample. The sample is maintained at 30 V, and the grid bias is varied from 10 to 50 V. Nonthermal positrons that leave the sample, having the normal component of the kinetic energy less than the grid potential, will return to the sample where they annihilate. Positrons with higher energy will pass through the grids and be removed by an **E**×**B** energy filter. By changing the grid bias, an integral energy spectrum of nonthermal positrons can be obtained. To avoid systematic errors caused by changes in the surface conditions, many sweeps are performed during each run.

The differential energy spectrum is obtained by differentiation of a Gaussian smoothed spectra (1.1 eV at FWHM).

In all the metals under investigation, the positron work function is positive. Thus, the spectra of the re-emitted positrons reflects the energy distribution of positrons that have energy greater than ϕ_+.

Because of the efficient mechanism of energy loss in metals, the re-emitted fraction is strongly dependent on the incident energy, as shown in figure 5.42 for several metals. The fraction of re-emitted positrons decreases when the incident energy is increased. The fraction of incident positrons that are re-emitted depends on the positron work function. In all metals, the re-emitted fraction is small. Thus, the analysis of the diffusion length is not greatly affected by nonthermal positrons. We noted in section 5.2 that the fitted diffusion length changes little when a grid is placed in front of the sample.

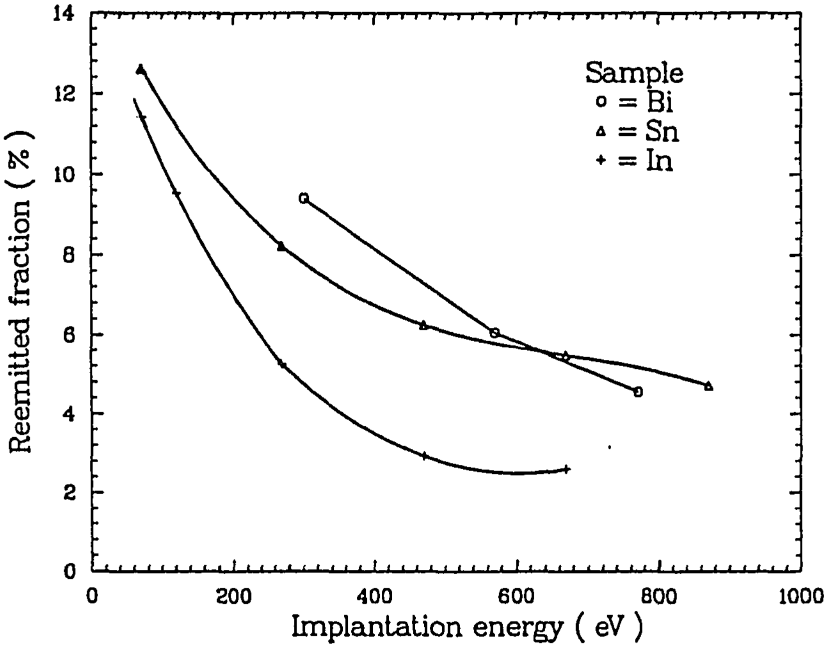

Figure 5.42: The fraction of incident positrons re-emitted from several metals, plotted against the implantation energy. The rapid decrease reflects the efficient mechanism of energy loss in metals.

Bismuth

The energy spectrum of re-emitted positrons from solid and liquid Bi shows that the positron work function is positive. To our knowledge, there are no theoretical calculations of the positron work function in Bi. For positrons implanted at E = 270 eV, and T = 30 °C , the peak of the re-emitted positron spectra is centered around E = 0 (figure 5.45). There should be a small deviation from zero due to the contact potentials between the sample and grid, but the resolution of our system does not allow us to see it. Metals with a negative positron work function show a re-emitted spectrum centered around E = $\phi_+ + \delta$E, with a high energy tail due to nonthermal positrons[130]; δE is the difference in the contact potentials between the sample and the grid in front of the sample. The contact potential is an order of magnitude smaller than the work function,[138] and smaller than the accuracy of our measurements ($\approx$ 1eV).

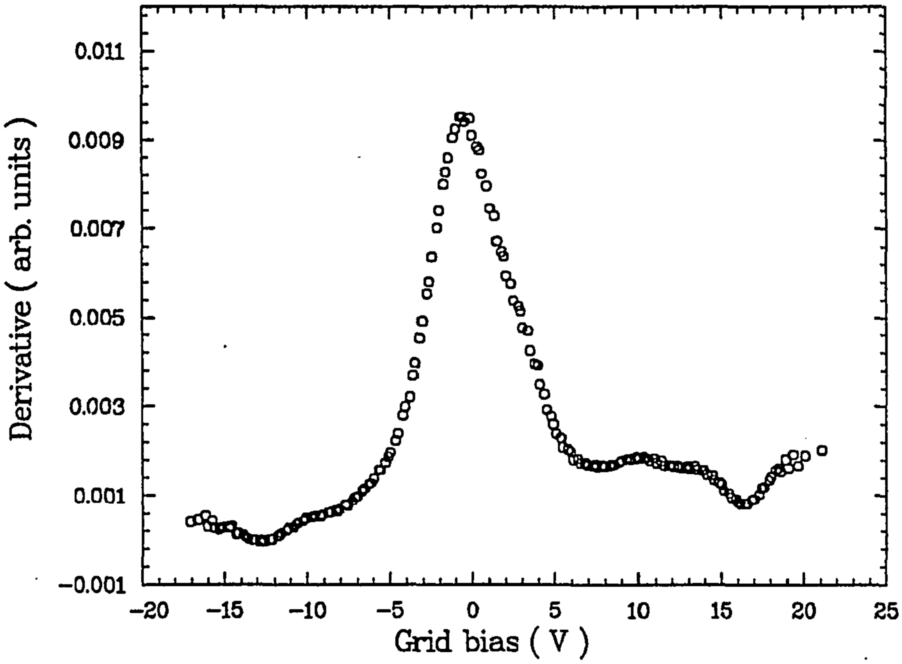

Figure 5.43: The differential energy spectra of positrons being re-emitted from Bi at T = 30 °C , after being implanted at E = 270 eV. The spectrum is centered around E = 0, which shows that the positron work function for Bi is positive.

Figure 5.44 shows the spectra of re-emitted positrons from Bi, implanted at E = 270 eV for different temperatures. The oscillations in the curves are produced by the smoothing routine. At T = 310 °C and 440 °C , Bi is liquid. For positrons implanted at E = 270, the fraction re-emitted is $\approx$ 9.4 %, independent of temperature. Thus, the mechanism of energy loss for positrons with E> ϕ_+ is not affected by temperature, and is the same for solid or liquid Bi. This suggests that the implantation profile does not change appreciably upon melting. Nonthermal positron trapping cannot be observed in liquid Bi.

Previous studies[40] of nonthermal positron reemission in Al found a large decrease in the re-emitted fraction when the sample was heated. Above 570 °C the fraction of re-emitted positrons with energies less than 2 eV is reduced. At this temperature, a large number of thermal vacancies is created, these can trap nonthermal positrons in Al. In Bi, only positrons with energies grater than E = ϕ_+ can be re-emitted; therefore, nonthermal trapping is not observed.

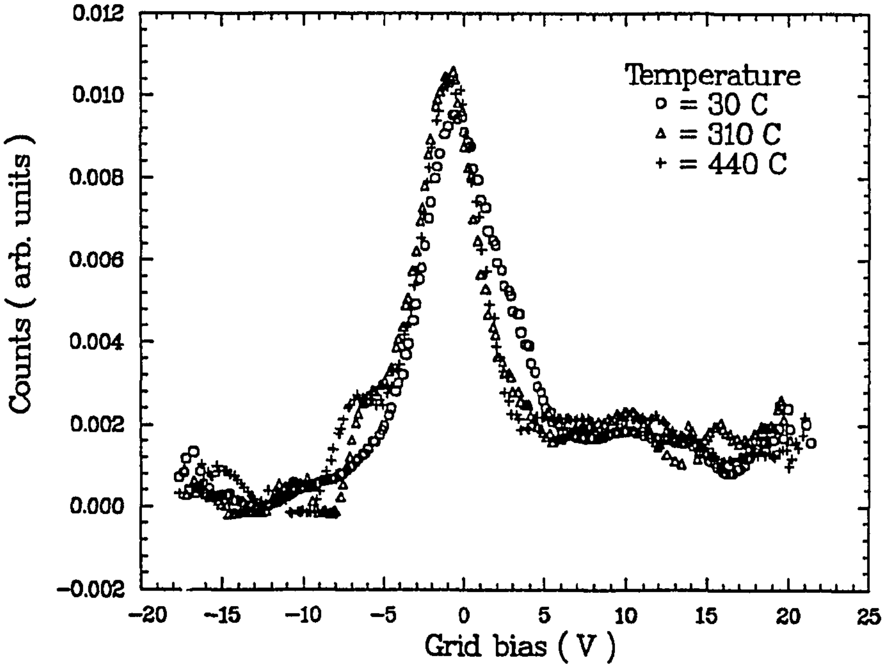

Figure 5.44: The differential energy distribution of positrons re-emitted from Bi, after being implanted at E = 270 eV, at three different temperatures. T = 310 °C and 440 °C corresponds to liquid Bi. The fraction is independent of temperature.

Sodium

Because Na is a very reactive metal, with a high vapor pressure, only data at low temperatures could be obtained. Since its work function is highly positive

($\phi_+ = 4.8$ eV), the re-emitted fraction is smaller than in Bi. At E = 70 eV, the fraction that is re-emitted from the surface of Na was ≈ 7.0 %.

The spectra of re-emitted positrons from Na, implanted at E = 70 eV, are shown in figure 5.45 for different temperatures. At T = 45 °C and 85 °C , Na is solid; at T = 110 °C Na is liquid. The re-emitted fraction for a given incident energy is independent of temperature, as was also true for Bi.

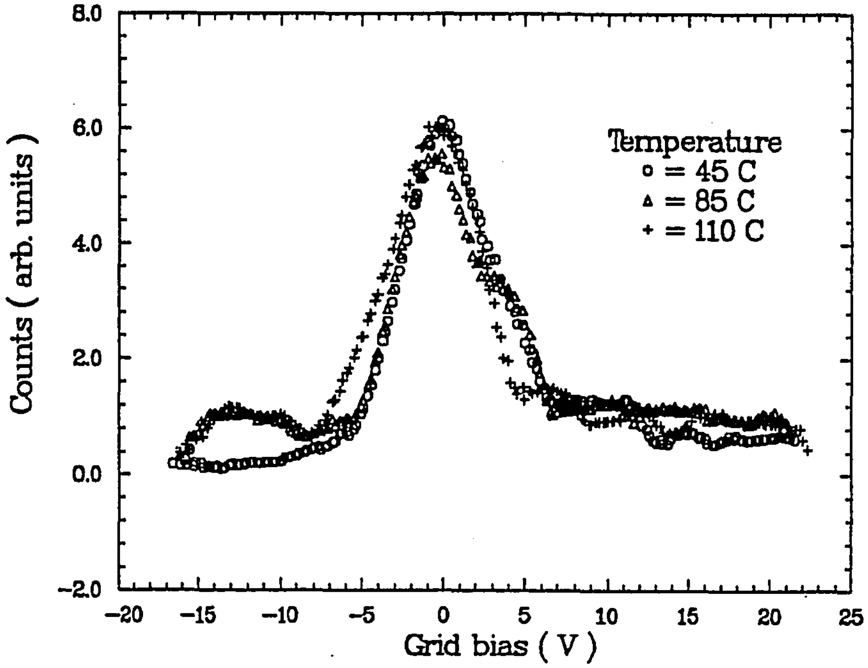

Figure 5.45: The differential energy distribution of positrons re-emitted from Na, after being implanted at E = 70 eV, at three different temperatures. T = 110 °C corresponds to liquid Na. The nonthermal re-emitted fraction is independent of temperature.

Tin

The fraction of incident positrons re-emitted at E = 70 eV from the surface of Sn was ≈ 13.6 %. The positron work function[114] in Sn is 2.7 eV, and only positrons with E> ϕ_+ are re-emitted. Previous studies[40] in Al found the re-emitted fraction to be ≈ 22%, with the positron work function ≈ 0.1 eV. We note that because of the large positron work function and small re-emitted fraction (compared to Al), the analysis of the diffusion length is not strongly affected by nonthermal positrons. This finding is consistent with the observation that the fitted diffusion length did not change when a grid was placed in front of the sample (section 5.2).

As the incident energy increases, the re-emitted fraction decreases rapidly due to the efficient mechanism of energy loss in metals (figure 5.42).

The spectra of re-emitted positrons from Sn, implanted at $E = 70$ eV, are shown in figure 5.46 for three temperatures. The oscillations in the curves are produced by the smoothing routine. Sn is solid at $T = 31$ °C and 180 °C and is liquid at $T = 240$ °C . The fraction of re-emitted positrons is ≈ 13.6 % of the incident positrons, independent of temperature.

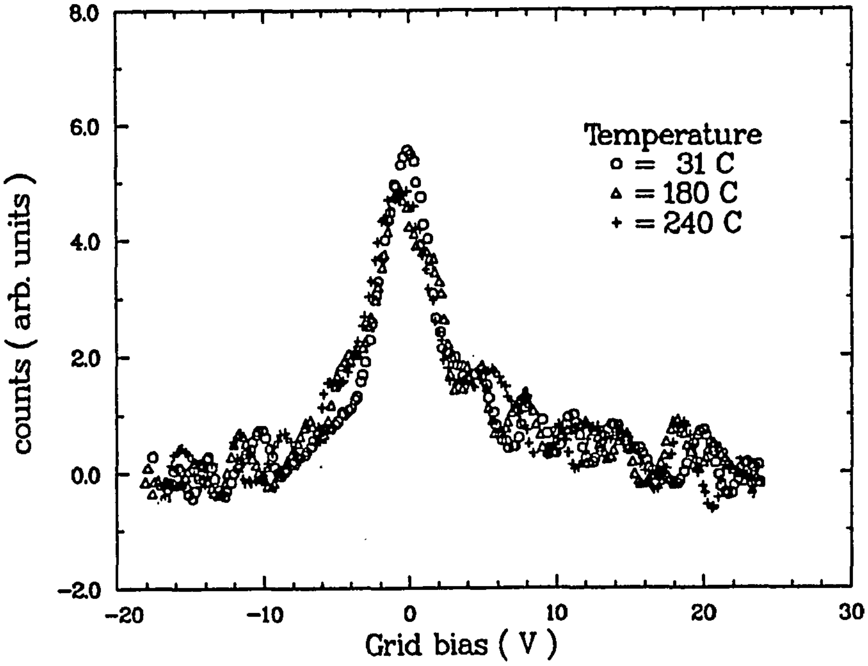

Figure 5.46: The differential energy distribution of re-emitted positrons from Sn. The implantation energy is $E = 70$ eV. At $T = 31$ °C and 180 °C Sn is solid. The fraction of re-emitted positrons is independent of temperature.

Above $E = \phi_+$ the mechanism of energy loss is not affected by temperature, and is the same for solid or liquid Sn. Nonthermal positron trapping is not observed at $T = 240$ °C , where a large number of traps is expected. In solid

Sn, (T = 31 and 180 °C) thermal vacancies are not able to trap positrons[18]. These results indicate that nonthermal trapping occurs for positrons with energy $-\phi_+ < E < 0$.

Indium

In contrast to previous metals, In shows pronounced thermal-vacancy trapping below the melting point. The fraction of incident positrons that are re-emitted at E = 70 eV from the surface of In was ≈ 11.4 %. The positron work function[114] in In is $\phi_+ = 2.6$ eV. Thus, only positrons with E > ϕ_+ are re-emitted. As with Bi, Sn, and Na, this fraction is small (compared with Al) because of the large positron work function. The diffusion length is not gratly affected by nonthermal positrons, a finding that is consistent with the observation that the fitted diffusion length did not change when a grid was placed in front of the sample.

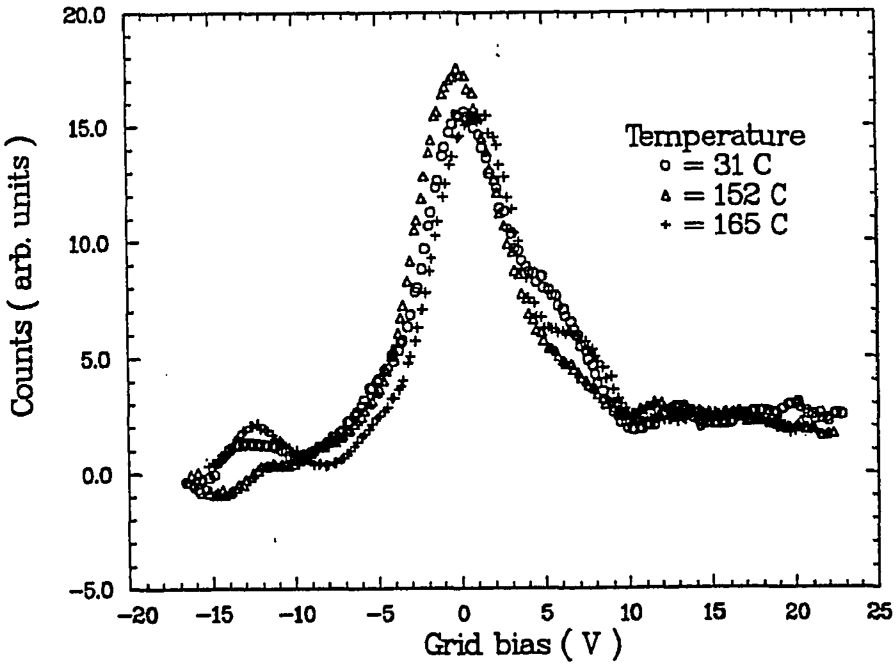

Figure 5.47: The spectra of re-emitted positrons from In, after being implanted at E = 120 eV. At T = 31 °C and 152 °C In is solid. At T = 165 °C In is liquid. As for Bi, Sn, and Na, the fraction of re-emitted positrons is independent of temperature.

As the incident energy is increased, the re-emitted fraction decreases rapidly, again, because of the efficient energy loss mechanism in metals (figure 5.42).

The spectra of re-emitted positrons from In, implanted at E = 70 eV, are shown in figure 5.47 for different temperatures. The oscillations in the curves are produced by the smoothing routine. At T = 31 °C , and 152 °C , In is solid, and at T = 165 °C In is liquid. The fraction of re-emitted positrons is ≈ 11.4 % of the incident positrons, independent of temperature.

Above E = ϕ_+ the energy loss mechanism is not affected by temperature, and is the same for solid or liquid In. Nonthermal positron trapping is not observed at T = 152 °C , where a large number of traps is expected. In solid Sn, (T = 31 and 180 °C) thermal vacancies are not able to trap positrons[119]. These results indicate that nonthermal trapping occurs for positrons with energy $-\phi_+ < E < 0$.

6. Conclusions

Using a newly constructed vertical positron beam, we have measured the Doppler broadening of the annihilation gamma rays from positrons in several liquid and solid metals. From these measurements, we calculated the diffusion coefficient of positrons in liquid metals and the binding energy of positrons and positronium to solid and liquid metallic surfaces. The aim of this work was to extract information of the density fluctuations of the ions in a liquid by measuring the diffusion coefficient of positrons. We found that the diffusion length is strongly dependent on density fluctuations. Our results show that the diffusion mechanism of positrons in liquids is a hopping process between traps. This is a very interesting mechanism that differs from the mechanism responsible for diffusion in solids, *i.e.* scattering with phonons.

We were also interested in the changes of the surface potential caused by melting. Positronium formation, as well as measurements of the fraction of nonthermal positrons released from the surface, allow us to determine the change in the surface potential and the branching ratio of positrons or positronium.

The samples studied were Ga, Bi, Na, Sn, Pb, and In. The primary reason to using these samples was their low melting point and low vapor pressure in the liquid phase. These characteristics measurements of Doppler broadening at ultra high vacuum ($\sim 1 \times 10^{-9}$ Torr), which is important for measuring positronium formation in a clean surface.

The S parameter was measured as function of the temperature for all samples. Table 1 summarizes the bulk S parameter across the melting point. These results are consistent with previous measurements of Doppler broadening[11–15,19,26,109] and lifetime experiments.[16,17,104,105] Our results show that the bulk S parameter

(S_{bulk}) is sensitive to the state of the positrons in the host. An appreciable change is observed in the bulk S parameter at the melting point. The metals that do not show positron trapping in the solid phase (Ga, Bi, Na, Sn), show a large increase in S_{bulk} upon melting. We interpret this effect as due to the creation of centers that can trap positrons in the liquid phase. The nature of these centers is not clear; most likely, they are regions where the ion density is lower than the average.

Table 6.1: Change in the bulk value of the S parameter below and above the melting point. The largest change is observed in metals where positrons do not get trapped in thermally generated vacancies in the solid phase. Changes in Ps fraction, f_o across the melting point also are shown. The error quoted in parentheses corresponds to the last significant digit.

Metal	S_{bulk} below T_m	S_{bulk} above T_m	f_o below T_m	f_o above T_m
Ga	0.474(1)	0.488(1)	0.36(2)	0.36(2)
Bi	0.436(1)	0.439(1)	0.90(2)	0.91(2)
Na	0.539(1)	0.545(1)	0.28(4)	0.23(4)
Sn	0.447(1)	0.458(1)	0.79(1)	0.79(1)
Pb	0.430(1)	0.430(1)	0.96(1)	0.94(1)
In	0.446(1)	0.446(1)	0.91(1)	0.87(1)

From measurements of the S parameter at the surface, S_s, we deduced that there is no change or only a small one across the melting point (within experimental error). This finding suggests that the branching ratio for Ps formation or annihilation at the surface is not altered by a change from a crystalline to a disordered structure on melting. Furthermore, that the characteristics of the surface state appear to be unchanged upon melting.

By fitting the temperature dependence of Ps formation, it is possible to obtain the formation energy of Ps, and the binding energy of positrons to the surface. Both results are given in table 6.2, along with the theoretical calculations of the binding energy by Nieminen and Hodges.[114] They calculated the electron-positron interaction by means of virtual excitations of surface and bulk plasmons, and minimized the energy expectation value at the ground state of a trial wave function. The experimental results are within 40 % of the theoretical results. In contrast to their calculations, a stable surface state ($E_b > \phi_+$) was found for In, Sn, and Pb. A stable surface state was found also for Ga, and Bi.

Table 6.2: Results of the Ps fraction fits to eq. (5.2). E_a, is the formation potential for Ps, E_b is the binding energy of positrons to the surface potential, F_0 is the fraction of energetic Ps emitted from the surface. f_s is the fraction trapped at the surface, Γ is the desorption rate of positrons from the surface at high temperatures, λ is the annihilation rate at the surface state. The error quoted in parentheses corresponds to the last digit.

Metal	E_a eV	F_0	f_s	Γ/λ 10^4	$^{\dagger}E_b$ eV	$^{*}E_b$ eV	surface states
Ga	0.35(3)	0.36(1)	0.55(1)	1.0(4)	3.19(3)	2.3	yes
Bi	0.32(1)	0.38(1)	0.58(1)	0.7(2)	2.72(1)		yes
Na						2.7	no
Sn	0.25(1)	0.46(3)	0.45(3)	0.8(1)	2.65(1)	2.5	yes
Pb						2.8	yes
In	0.25(1)	0.47(3)	0.46(2)	0.8(2)	3.25(1)	2.4	yes

† This work

* Theoretical work from Nieminen and Hodges[114]

The fraction of nonthermal positrons re-emitted from the metals we investigated was not affected by the transition from the solid to liquid phase. The re-emitted fraction in Bi (for a beam energy of $E_i = 270$ eV), Na ($E_i = 70$ eV), Sn ($E_i = 70$ eV) and In ($E_i = 120$ eV) remained constant over a wide range of temperature. The positron work function in all metals investigated is very large (2-5 eV), which prevents low-energy epithermal positrons from leaving the sample. These positrons are more likely to be affected by a change in the number of traps[40] due to melting or to an increase in temperature. Thus, the fraction that can escape is not very sensitive to melting or to changes in temperature. This indicates that the surface potential does not change appreciably upon melting.

Table 6.3 is a summary of the diffusion length results for the different metals investigated is presented. The largest change in the diffusion length is observed in metals where the state of the positron changes from a Bloch-like state to a trapped state upon melting. In metals that trap positrons in thermally generated vacancies, the drop in the diffusion length upon melting is small or nonexistent. In all liquid metals, the positron seems to be in a trapped state. Diffusion appears to be related to trapping in temporary fluctuations in the ionic structure. The positron hops from fluctuation to fluctuation. The size of the traps is strongly dependent on temperature, so that when temperature is increased, the hopping motion increases.

Table 6.3: Diffusion length L_+ results below and above the melting point for metals under investigation. The largest change is observed in metals where positrons do not get trapped in thermally generated vacancies. m_+ is the slope of the linear increase of the diffusion length in liquid metals, E_v is the binding energy of positrons in vacancies in the solid phase, from reference 117

Metal	L_+ (Å) below T_m	L_+ (Å) above T_m	m_+ (Å/°C)	E_v (eV)
Ga	1200(100)	60(5)		2.65
Bi	500(40)	190(20)	0.15(0.02)	
Na				0.02
Sn	750(50)	260(20)	0.163(0.029)	2.64
Pb	180(20)	180(20)	0.095(0.012)	3.44
In	245(20)	225(20)	0.123(0.014)	2.55

In the liquid phase of all metals, the diffusion length increased with temperature. In Ga, the increase is very fast, resembling a thermally activated process. All other metals showed a slow increase in the diffusion length with temperature. A simple least-squares fit was performed in each case (the results are summarized in table 6.3).

It is known that when there are vacancies that trap positrons in the solid phase, the diffusion length is directly related to the strength of the trapping potential.[107] If the diffusion length in liquid metals is only related to the binding energy at defects, then in metals where trapping is weak, the diffusion length should be longer than in metals where the trapping is strong. Following the same argument, as the temperature is increased, thermal detrapping should occur more frequently in metals where trapping is weak.

There are no calculations of the binding energy of positrons to traps in the liquid phase. Although there is no *a priori* indication that the binding energy to vacancies in the liquid phase should be similar to the solid phase, in order to compare with the diffusion length, we will assume that it is the same. Calculations of the binding energy in the solid phase[117] should give a reasonable estimate of positron binding to traps in liquids. Table 6.3 gives the slope m_+, of the increase in the diffusion length in the liquid, and the binding energy of positrons to vacancies. Liquid Ga, which shows a rapid increase in the diffusion length with temperature, has a very large binding energy in the solid phase. Pb, which has also a large binding energy in the solid, shows a very weak increase in the diffusion length. These facts indicate that the strength of the binding to the traps is not the only effect leading to the increase in the diffusion length in the liquid.

The positron diffusion coefficient in liquid metals, D_+, is plotted in figure 6.1 (using $D_+ = L_+^2/\tau$). The solid lines were calculated using the linear fits to the diffusion length to distinguish the different results. The lifetime was assumed to be constant over the temperature interval. For Ga, the solid line is a guide to the eye because no simple fit could be done. The diffusion coefficient shows a different behavior than the other metals. A low temperatures the increase is linear, followed by a rapid increase at T ≈ 200 °C . For Ga, the lifetime used was τ = 260 ps[16]. Because no experimental data on lifetime in liquid Sn exists, we used the calculated lifetime at metal vacancies taken from reference 106; τ = 282 ps. For Pb, τ = 275 ps was used, taken from the lifetime at metal vacancies in solid Pb.[106]

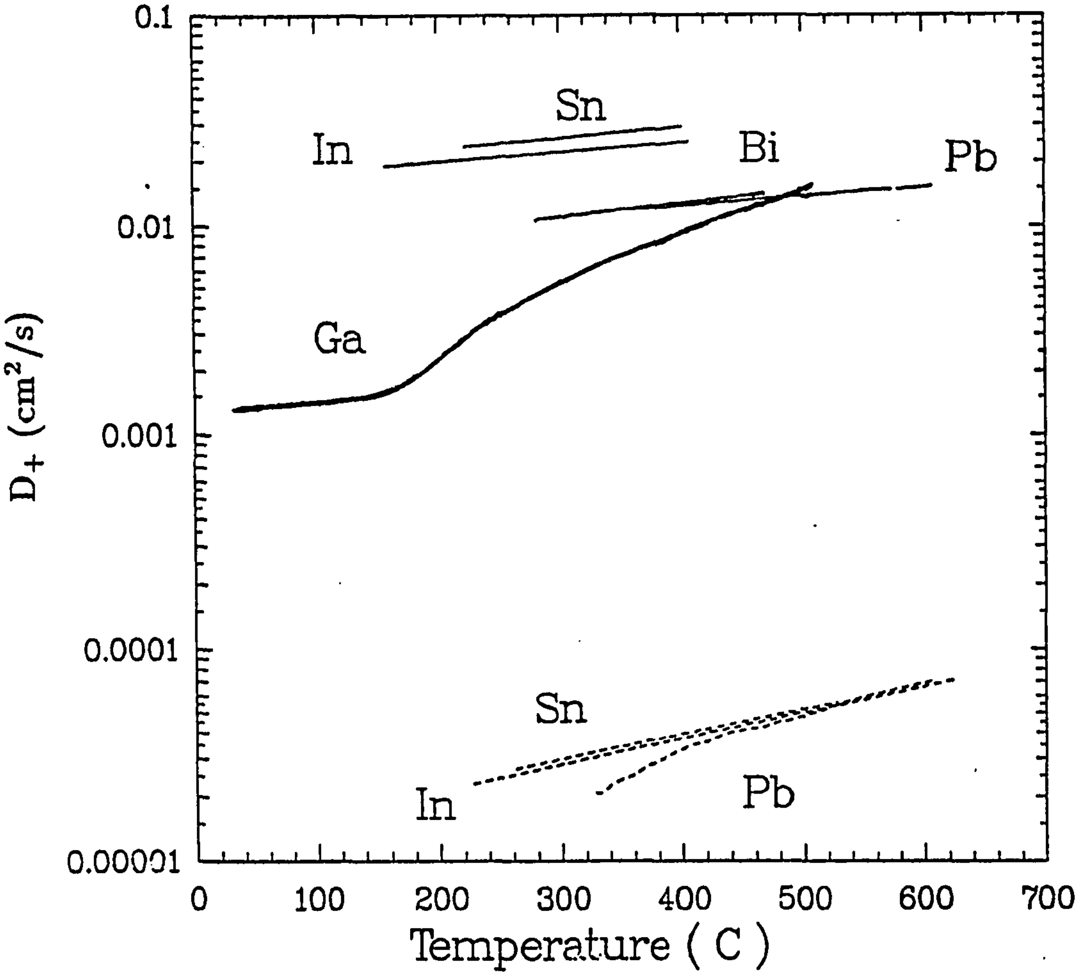

Figure 6.1: Diffusion coefficient of positrons in liquid metals. The solid lines are calculated from the linear fits to the diffusion length, as explained in the text, for Ga, the solid line is a guide to the eye. The dashed lines are the self-diffusion coefficient in liquid metals.

The lifetime for liquid In was taken from reference 109, $\tau = 260$ ps. In Bi, there is no data for positron lifetimes in vacancies nor in the liquid phase. Thus, the lifetime was estimated assuming that upon melting, it would increase $\approx 30\%$ from the bulk value ($\tau_b = 258$ ps); this is a typical increase seen in metals[107]

The ionic self-diffusion coefficient in liquid metals also has been plotted in the same scale. This coefficient is three orders of magnitude smaller than the diffusion coefficient of positrons. The difference is expected because the difference in the positron and atomic mass is at least two orders of magnitude.

It is now widely believed that the self-diffusion process in liquid metals is not a thermally activated process[1-5,131,132], *i.e.* This process requires that a void of molecular dimensions is created in the neighborhood of the ion before it jumps[133-136]. An activated process predicts a diffusion coefficient that has an exponential temperature dependence, $D = D_o \exp(-E/kT)$, where E is the activation energy.

However, the experimental data on self-diffusion show that no simple function can be used to fit the data[131], and that an exponential dependence on temperature is not the norm. It is believed that there may be many modes of motion[81,82] (activated diffusion and free diffusion), that contribute, and the relative importance of each mode depends on temperature.

The diffusion mechanism of positrons in liquids may also be a combination of many diffusion modes. 1) A thermally activated process that depends on the strength of the binding to the trap. This process would also depend on the availability of a void where the positron can jump. 2) Another mechanism may result from fluctuations in the size (and binding energy) of the traps. In each metal, the relative importance of these three mechanisms differs at different temperatures.

Table 6.4 summarizes the diffusion coefficients in several solid and liquid metals at the melting point; these values are compared with the self-diffusion coefficient in liquid metals.

The behavior of the diffusion length of positrons in liquid metals suggests that there are density fluctuations in liquid metals of the order of a few atomic volumes which to a small degree are dependent on temperature. The time scale of these fluctuations are of the order[1] of 10^{-12} s. However, the size and the frequency of these fluctuations needs to be related to the diffusion coefficient of positrons. Calculations of this type are needed to compare with our experimental data to shed light into the dynamics of the ions in liquid metals

Table 6.4: Diffusion coefficient below and above the melting point for several metals. D_s is the self-diffusion coefficient of the ions at the melting point, from reference 131. The largest change is observed in metals where positrons do not get trapped in thermally generated vacancies.

Metal	D_+ 10^{-2}cm^2/s below T_m	D_+ 10^{-2}cm^2/s above T_m	D_s 10^{-5}cm^2/s above T_m
Ga	75(7)	1.4(0.1)	1.6
Bi	9.7(0.8)	1.1(0.1)	
Na			5.2
Sn	28(2)	2.4(0.2)	2.3
Pb	1.2(0.1)	1.2(0.1)	2.2
In	2.1(0.2)	1.9(0.2)	1.6

Future studies.

There are indications that melting of small clusters embedded in a larger host occurs at temperatures below the melting point.[145] The diffusion length and the S parameter in the bulk of a metal offer a unique opportunity to study melting of clusters or multilayers. The S parameter length in Bi, Ga, Sn, and Na is remarkably different in the solid from the liquid phase, offering the opportunity to study the temperature dependence of the melting point of clusters of different sizes. Thus, if a cluster of any of these metals is embedded in another material with different bulk melting point, the change in S parameter can reveal any deviation of the melting temperature of the cluster from the bulk melting temperature.

The diffusion length offers the possibility to study melting of overlayers of different metals. For example, a multilayer of Al/Sn/Al should show an increase in the S parameter if the Sn layer melts. A large decrease in the diffusion length of the Sn layer should be observed at the same time. If melting in thin layers occurs at temperatures below the melting point, or if a large number of defects are created, the S parameter or the diffusion length would show a change different from that in the bulk.

An interesting set of experiments is the study of surface melting. Recent studies[139–141] show that the open-packed surface of Pb, Al, and other metals lose their crystalline order few hundred degrees below the bulk melting point. A roughening transition is seen, even at lower temperatures. The thickness of the molten layer is only a few nm, and increases logarithmically as the temperature approaches the melting point[140]. A useful probe of this liquid layer is Ps formation. For several of the metals studied (Bi, Na, Pb, and In), a decrease in the Ps fraction was observed upon melting. Because Ps is very sensitive to surface conditions, it may be an ideal probe to surface melting. A gradual decrease in the Ps fraction could be observed in open packed surfaces like Pb(110) approaching the melting point because of the appearance of a liquid layer. In close packed surfaces that do not show surface melting effects, like Pb(111), only a sudden decrease in Ps fraction should be observed on melting.

References

1. Mitsuo Shimoji, *Liquid Metals.* (Academic Press Inc., New York, 1977).
2. Y. Waseda, *The structure of non crystalline materials.* (McGraw Hill, N.Y. 1980).
3. N. H. March, *Liquid Metals, concept and theory* Cambridge Monographs on mathematical physics, Cambridge University press, 1990.
4. T. E. Faber, *Theory of liquid metals* , Cambridge University Press, 1972.
5. J. P. Hansen and I. A. McDonald, *Theory of simple liquids*, New Yok, Academic Press, 1986.
6. C. H. Hodges, Phys. Rev. Letters **25**, 284 (1970).
7. C. D. Anderson, Science **76**, 238 (1932), and Phys. Rev. **41**, 405 (1932).
8. P. J. Schultz and K. G. Lynn, Rev. of Mod. Phys. **60**, 701 (1988), and references therein.
9. I. K. MacKenzie, T. L. Khoo, A. B. McDonald, and B. T. A. McKee, Phys. Rev. Letters **19**, 946 (1967).
10. O. E. Mogensen, and G. Trumpy, Phys. Rev. **188**, 639 (1969).
11. F. Itoh, M. Kuroha, K. Kai, and S. Takeuchi, J. Phys. Soc. Japan **33**, 567 (1972).
12. R. N. West, R. E. Borland, J. R. A. Cooper, and N. E. Cusak, Proc. Royal Soc. **92**, 195 (1967).
13. D. R. Gustafson and A. R. MacKintosh, Phys. Letters **5**, 234 (1964).
14. A. T. Stewart, J. H. Kusmiss and R. H. March, Phys. Rev. **132**, 495 (1963).
15. D. R. Gustafson, A. R. MacKintosh, and D. J. Zaffarano, Phys. Rev. **130**, 1455 (1963).
16. W. Brandt and H. F. Waung, Physics Letters **27A**, 700 (1968).
17. V. H. C. Crisp, D. G. Lock, and R. N. West, J. of Phys. **F** 4, 830 (1974).

18. J. H. Kusmiss and A. T. Stewart, Adv. Phys. **16**, 471 (1967).

19. W. Triftshäuser, Phys. Rev. **B** 12, 4634 (1975).

20. R. N. West, Adv. in Physics **22**, 263 (1973).

21. A. P. Mills, Jr. Phys. Rev. Lett. **41**, 1828 (1978).

22. R. Khatri, M. Charlton, P. Sferlazzo, K. G. Lynn, A. P. Mills, Jr., L. O. Roellig, Appl. Phys. Lett. **57**, 2374 (1990).

23. M. Weber, S. Tang, S. Berko, B.L. Brown, K.F. Kanter, K.G. Lynn, A.P. Mills, L.O. Roellig and A. Viescas, Phys. Rev. Letters **61**, 2542 (1988).

24. A. Weiss, Phys. Rev. Letters **61**, 2245 (1988).

25. K. G. Lynn, Phys. Rev. Letters **43**, 391 (1979).

26. H.E. Shaeffer, W.Eckert, J. Briggman, and W. Bauer, J. Phys. C. SA97, (1989).

27. B. Bergersen, E. Pajanne, P. Kubica, M. J. Stott, and C. H. Hodges, Sol. State Comm. **15**, 1377 (1974).

28. J. Oliva, Phys. Rev. **B** 21, 4909 (1980).

29. E. J. Woll and J. P. Carbotte, Phys Rev **164**, 985 (1987).

30. A. Perkins and J. P. Carbotte, Phys Rev **1**, 101 (1970).

31. R. M. Nieminen and J. Oliva, Phys. Rev. B **22**, 2226 (1980).

32. P. J. Schultz, R. Logan, T. E. Jackman and J. A. Davies, Phys. Rev. B **38**, 6369 (1988).

33. W. N. Lennard, P. J. Schultz, and G. R Massoumi, Nuc. Inst. and Methods **B 33**, 128 (1988).

34. S. Valkealahty and R. M. Nieminen, Appl. Phys. **A 35**, 51 (1984).

35. J. M. Dale, L. D. Hulett, and S. Pendyala, Appl. Surf. Science **8**, 472 (1981).

36. A. P. Mills, W. S. Crane, Phys. Rev. **A 31**, 593 (1985).

37. E. M. Gullikson and A. P. Mills, Phys. Rev. Lett. **57**, 376 (1986).

38. S. C. Sharma, S. Berko and W. K. Warburton, Phys. Lett. **58 A**, 405 (1976).

39. J. A. Jackman, G. M. Hood and R. J. Schultz, J. Phys. F **17**, 1817, (1987).

40. B. Nielsen, K. G. Lynn and Y.C. Chen, Phys. Rev. Lett. **57**, 1789 (1986).

41. H. Huomo, A. Vehanen, M. D. Bentzon and P. Hautojarvi, Phys. Rev. B **35**, 825 (1987).

42. T. McMullen and M. J. Stott, Phys. Rev. B **35**, 825 (1986).

43. E. Gramsch and K. G. Lynn, Phys. Rev. B **40**, 2537 (1989).

44. H. Houmo, E. Soininen, and A. Vehanen, Appl. Phys. **A 49**, 647 (1989).

45. A. F. Makhov, Sov. Phys. Solid State **2**, 1934 (1960).

46. L. Katz and A. S. Penfold, Rev. of Mod. Phys. **24**, 28 (1952).

47. A. Vehanen, K. Saarinen, P. Hautojärvi, and H. Huomo, Phys. Rev. **B 35**, 4606 (1987).

48. K. G. Lynn, and H. Lutz, Phys. Rev. **B 22**, 4143 (1980).

49. K. Ritley and K. G. Lynn, Positron beams for solids and surfaces. AIP conference proceedings 218, pp. 3, London, Canada, July 1990, edited by P. J. Schultz, G. R. Massoumi and P. Simpson.

50. K. G. Lynn, T. Mckay, and M. Mckeown (1987). (unpublished)

51. J. A. Baker, N. B. Chilton, K. O. Jensen, A.B. Walker, and P. J. Coleman, Appl. Phys. Lett. **59**, 2962 (1991)

52. M. McKeown, K. G. Lynn, V. J. Ghosh, D. O. Welch, (to be published) (1991)

53. K. Ritley and K. G. Lynn, (to be published) (1991)

54. A. P. Mills and R. Wilson, Phys. Rev. **A 26**, 490 (1982).

55. K. G. Lynn and D. O. Welch, Phys Rev. B, **22**, 99 (1980).

56. T. R. Waite, Phys. Rev. **107**, 463 (1957).

57. K. G. Lynn, Proceedings of the International School of Physics Enrico Fermi, Course LXXXIII, Edited by W. Brandt and A. Dupasquier, North-Holland Publishing Co. 1983, page 609.

58. V. Heine and C. H. Hodges, J. Phys. **C 5**, 225 1972

59. C. H. Hodges and M. J. Stott, Phys. Rev. **B** 7, 73 (1973).

60. I. K. MacKenzie, J. A. Eady, and R. R. Gingerich, Physics Letters **33**A, 279 (1970).

61. J. L. Campbell Appl Phys. **13**, 365 (1977).

62. S. Mantl and W. Triftshäuser, Phys. Rev. Lett. **34**, 1554 (1975).

63. S. Mantl and W. Triftshäuser, Phys. Rev. **B** 17, 1645 (1978).

64. Bent Nielsen, K. G. Lynn, A. Vehanen, and Peter. J. Schultz, Phys. Rev. B **32**, 2296 (1985).

65. A. van Veen, H. Schut, J. de Vries, R. A. Hakvoort, and M. R. Ijpma, Positron beams for solids and surfaces. AIP conference proceedings 218, London, Canada, July 1990, edited by P. J. Schultz, G. R. Massoumi and P. Simpson.

66. D. T. Britton, P. C. Rice-Evans and J. H. Evans Phil. Mag. Lett. **57**, 165 (1088).

67. F. Reif *Fundamentals of statistical and thermal physics,* (McGraw-Hill Book Co.) New York (1965)

68. T. L. Hill, *Statistical Mechanics* , McGraw-Hill, New York (1956).

69. M. Hasegawa and M. Watabe, J. Phys. Soc. Jpn. **32**, 14 (1972).

70. G. K. Corless and N. H. March, Phyl. Mag. **6**, 1285 (1961).

71. J. G. Kirkwood, J. Chem. Phys. **3**, 300 (1935).

72. I. R. McDonald and S. P. O'Gorman, Phys. Chem. Liquids **8**, 57 (1978).

73. J. Yvon, *Actualités Cientifiques et Industrielles* , No. 203, Herman et Cie, Paris (1935).

74. M. Born and H. S Green, Proc. Royal Soc. **A**, 188, 10 (1946).

75. N. N. Bogoliubov, J. Phys. USSR, **10**, 257, 265 (1946).

76. L. S. Ornstein and S. Zernike, Proc. Acad. Sci. Amst. **17**, 193 (1914).

77. J. K. Perkus and G. J. Yevick, Phys. Rev. **110**, 1 (1958).

78. E. Thiele, J. Chem. Phys. **39**, 474 (1963).

79. M. S. Wertheim, Phys. Rev. Lett. **10**, 321 (1963).

80. B. J. Alder and T. E. Wainwright, J. Chem. Phys. **33**, 1439 (1960).

81. N. F. Carnahan and K. E. Starling, J. Chem. Phys. **53**, 600 (1970).

82. G. H. Vineyard, *Liquid Metals and Solidification*, Amer. Soc. Metals, Cleveland, 1 (1958).

83. J. E. Enderby, *Physics of Simple Metals* , North Holland, Amsterdam, 612 (1968).

84. P. A. Egelstaff, N. H. March and N. C. McGill, Can. J. Phys., **52**, 1651 (1974).

85. A. H. Narten, J. Chem. Phys. **56**, 1185 (1972).

86. A. J. Greenfield, J. Wellendorf, and N. Wiser, Phys. Rev A 4, 1607 (1971).

87. K. Furukawa, Rep. Progr. Phys. **25**, 395 (1962).

88. J. D. Bernal, *Structures and properties of liquids,* (ed. T. H. Hughel), Elsevier, London (1965).

89. R. Collins *Phase transitions and critical phenomena,* (eds. C. Domb and M. S. Green) Academic Press, London and New York (1972).

90. H. Ocken and C. C. J. Wagner, Phys. Rev **149**, 122 (1966).

91. D. M Chen, K. G. Lynn, R. Pareja, and B Nielsen, Phys Rev. B, **31**, 4123 (1985).

92. S. M. Hutchins, P. G. Coleman, A. Alam, and R. N. West, **ICPA 85**, pp 983 (1985).

93. E. Gramsch, J. Throwe, and K. G. Lynn, Appl. Phys. Lett. **51**, 1862 (1987).

94. A. Vehanen, J. Lahtinen, H. Huomo, J. Mäkinen, K. Rytsölä, and P. Hautojärvi, **ICPA 85**, pp 989.

95. R. Ley, K. D. Niebling, A. Osipowicz, A. Picard, and G. Wert, **ICPA 85**, pp 996.

96. R. H. Howell, R. A. Alvarez, and M. Stanek, Appl. Phys. Lett. 40, 751 (1982).

97. A. P. Mills, Jr. and E. M. Gullikson, Appl. Phys. Lett. **49**, 1121 (1986).

98. K. G. Lynn, B. Nielsen, and H. Quateman, Appl. Phys. Lett. **47**, 239 (1985).

99 R. Mayer, E. Gramsch, and A. Weiss, Phys. Rev. **B 40**, 11287 (1989).

100. Xiao-ye Wu, Peter Dull, and K. G. Lynn, Appl. Phys. Lett. **57**, 998 (1990).

101. K. G. Lynn, E. Gramsch, S. G. Usmar, and P. Sferlazzo, Appl. Phys. Lett. **55**, 87 (1989).

102. H. Weisberg and S. Berko, Phys. Rev. 154, 249 (1967).

103. S. Mantl and W. Triftshäuser, Phys. Rev. **B** 17, 1645 (1978).

104. D. Segers, C. Dauwe, M. Dorikens, and L. Dorikens-Vanpraet, Appl. Phys. **10**, 121 (1976)

105. D. Segers, M. Dorikens, and L. Dorikens-Vanpraet, Phys. Stat. Sol. (a) **48**, 133 (1978).

106. M. Manninen, R. Nieminen, P. Haujärvi, and J. Arponen, Phys. Rev. **B** 12, 4012 (1975).

107. A. Seeger J. Phys. F: Metals Physics, **3**, 248 (1973).

108. S. C. Sharma, S. Berko and W. K. Warburton, Phys. Letts. **58A**, 405 (1976).

109. Yuichiro Kishimoto and Shoichiro Tanigawa, **ICPA 82**, pp 404.

110. D. T. Britton and P. C. Rice-Evans, Phys. Letters **A** 126, 444 (1988).

111. J. Hafner and W. Jank, Phys. Rev. **B 42**, 11530 (1990).

112. A. P. Mills, Jr. Solid State Comm. **31**, 623 (1979).

113. I. J. Rosenberg, A. H. Weiss and K. F. Canter, J. Vacc. Sci. Technol. **17**, 253 (1980).

114. R. M. Nieminen and C. H. Hodges, Phys. Rev. B **18**, 2568 (1978).

115. O. V. Boev, M. J. Puska, and R. M. Nieminen, Phys Rev. B **36**, 7786 (1987).

116. N. W. Ashcroft and N. D. Mermin, "Solid state Physics" (Holt, Rinehart, and Winston, New York 1976).

117. Positrons in solids, Edited by P. Hautojarvi, Springer-Verlag (1979), page 178.

118. R. N. West, R. E. Borland, J. R. A. Cooper and N. E. Cusack, Proc. Phys. Soc. **92**, 195 (1967).

119. I. K MacKenzie,G. F. O. Langstroh, B. T. A. McKee, and C. G. White, Can. J. of Phys. **42** 1837 (1967).

120. S. Dedoussis, S. Charalambous and M. Chardalas, Phys. Lett. **62A**, 359 (1977).

121. Y. C. Jean, K. G. Lynn, and M. Carroll, Phys. Rev. **B** 21, 4935 (1980).

122. B. T. A. McKee, W. Trifthäuser and A. T. Stewart, Phys. Rev. Lett. **28**, 358 (1972).

123. R. H. Howell, I. J.. Rosenberg, P. Meyer and M. J. Fluss, Phys. Rev. **B** 35, 4555 (1987).

124. C. H. Hodges and H. Trinkaus, Sol. State. Comm. **18**, 857 (1976).

125. C. H. Leung, T. McMullen, and M. J. Stott, J. of Phys. F **6**, 1063 (1976).

126. A. P. Mills, Jr., Phys. Rev. Lett. **41**, 1828 (1978).

127. R. H. Ritchie and J. H. Ashley, J. Phys. Chem. Sol. **26**, 1689 (1965).

128. C. J. Powell, J. Vac. Sci. Technol. A **3**, 1338 (1985).

129. Bent Nielsen, K. G. Lynn and Yen-C. Chen, Phys. Rev. Lett. **57**, 1789 (1986).

130. A. P. Mills, *Positron solid state physics*, edited by W. Brandt, and A. Dupasquier (North Holland, Amsterdam, 1983), pp 432

131. N. H. Nachtrieb, Advan. Phys. **16**, 309 (1967)

132. C. Brown and N. H. March, Phys. and Chem. of Liquids, **1**, 141 (1968).

133. R. Zwanzig, J. Chem. Phys. **79**, 4507 (1983).

134. C. C. Mattai, and N. H. March, Phys. and Chem. of Liquids, **11**, 207 (1982).

135. R. Swalin, Acta Metall. **7**, 747 (1959)

136. M. H. Cohen and D. S. Turnbull, J. Chem. Phys. **31**, 1164 (1959)

137. M. C. Bellisent-Funel, P. Chieux, D. Levesque, and J. J. Weis, Phys. Rev. A, **39**, 6310 (1989).

138. C. Herring and M. H. Nichols, Rev. of Mod. Phys. **21**, 185 (1949).

139. R. H. Willens, A. Kornblit, L. R. Testardi, and S. Nakahara, Phys. Rev. B, **25**, 290 (1982).

140. J. W. M. Frenken, P. M. J. Maree, and F. van der Veen, Phys. Rev. B, **34**, 7506 (1986).

141. A. Pavlovska, and E. Bauer, Appl. Phys. A, **51**, 172 (1990).

142. D. W. Gidley, A. R. Köymen, and T. W. Capehart, Phys. Rev. B, **37**, 2465 (1988).

143. S. A. Chu, A. P. Mills, Jr., and C. A. Murray, Phys. Rev. B, **23**, 2060 (1981).

144. G. Petzow, *Metalographic Etching* American Soc. for Metals, Metals Park, Ohio, 1978.

145. S. Berry, Scientific American, 68, August 1990.